PHOTOPRODUCTION OF

CHARGED PIONS IN THE

PHOTON ENERGY RANGE 70-170 GEV

John Waterhouse

A thesis submitted to the Victoria University of Manchester for the degree of Doctor of Philosophy in the Department of Physics in the Faculty of Science.

November 1984

CONTENTS

Contents	1
Abstract	4
Preface	5
Chapter I - Photoproduction	6
1.1 - Introduction	7
1.2 - Photons and the Vector Meson Dominance Model	9
1.3 - Diffractive Photoproduction of Vector Mesons	11
1.4 - Inclusive Single Particle Photoproduction and KNO Scaling	13
1.5 - Inclusive Vector Meson Photoproduction	19
1.6 - Conclusion	23
1.7 - References	24
1.8 - Figure Captions	25
Chapter II - The Beam line and Tagging System	26
2.1 - Introduction	27
2.2 - The Beam Line	30
2.3 - The Beam Spectrometer	35
2.4 - The Tagging System	39
2.5 - The Tagging System Electronics	42
2.6 - Beam Line and Tagging System Performance	46
2.8 - References	51
2.9 - Figure Captions	52
Chapter III - The Channel Plate Detector	53
3.1 - Introduction	54

3.2 - Detector Design and Construction 58

3.3 - Results 67

3.3.1 - Source Test Results 67

3.3.2 - Test Beam Results 70

3.4 - Conclusion 78

3.5 - References 80

3.6 - Figure Captions 82

Chapter IV - The Omega Spectrometer and Particle Identification 83

4.1 - Introduction 84

4.2 - The Target Region 86

4.3 - The Omega Spectrometer 87

4.4 - The Ring Image Čerenkov Detector 91

4.5 - The Photon Detector 98

4.6 - The Transition Radiation Detector 101

4.7 - The Trigger Detectors 104

4.8 - References 107

4.9 - Figure Captions 108

Chapter V - The Trigger and Data Acquisition System 109

5.1 - Introduction 110

5.2 - The Trigger 111

5.2.1 - The Interaction Trigger 112

5.2.2 - The Hadron Guillotine Trigger 113

5.2.3 - The Good Event Trigger 155

5.2.4 - The Dead Time Gating 117

5.3 - The Data Acquisition System 120

5.4 - On line Monitoring and Control 123

5.5 - Trigger Performance 125

5.6 - References 129

5.7 - Figure Captions 130

Chapter VI - Off line Monitoring and Production Analysis 131

6.1 - Introduction 132

6.2 - Off-line Monitoring 133

6.3 - Production Analysis 134

6.3.1 - TRIDENT 135

6.3.2 - PEDRO 137

6.3.3 - The Simulation and MAP 139

6.3.4 - DST Writing, Reading and Analysis 141

6.4 - General Features of the Data 144

6.5 - References 152

6.6 - Figure Captions 153

Chapter VII - Physics Analysis 154

7.1 - Introduction 155

7.2 - Data Selection 156

7.3 - Charged Particle Photoproduction and KNO scaling 159

7.3.1 - The Proton Fragmentation Region 168

7.3.2 - The Photon Fragmentatation Region 170

7.4 - Inclusive Rho(770) production 177

7.5 - Elastic Rho(1600) Production 187

7.6 - Conclusion 196

7.7 - References 199

7.8 - Figure Captions 200

Acknowledgements 202

ABSTRACT

This thesis describes the preliminary data from the photoproduction experiment WA69 performed at CERN (Geneva, Switzerland) by the Eγ collaboration of physicists based at Lancaster, Manchester, Sheffield Universities and the Rutherford Appleton Laboratory in England, and Bonn University in West Germany.

A tagged photon beam, of energy 70 - 170 GeV, derived from the CERN SPS proton beam, was incident on a liquid hydrogen target in the magnetic field of the Omega Spectrometer. The beam line, photon tagging system, the down stream particle identification detectors and trigger system are described. The development of a high rate, high resolution beam profile detector using a secondary emission cathode and channel plate electron multipliers is also described.

The inclusive photoproduction of single charged pions has been investigated and has been found to be broadly similar to that in hadron-hadron scattering at similar energies. The charge-multiplicity distributions have been compared with KNO scaling predictions and a hadron-hadron model.

The inclusive photoproduction cross-section for the Rho(770) vector meson was found to be 27 ± 6 μb. The Rho meson production distributions have also been investigated.

In the elastic photoproduction of $2\pi^+2\pi^-(p)$ a broad enhancement at about 1600 MeV has been seen with an estimated cross-section of about 0·45 ± 0·26 μb.

PREFACE

The author of this thesis obtained his first degree (in Mathematics and Physics) at Manchester University, England, in June 1981.

From October 1981 to September 1984 the author has been working with the Eγ group at Manchester University, contributing to the WA69 photoproduction experiment at the CERN SPS. The author was involved with the channel plate detector development, the installation and setting up of the beam and tagging system, as well as the analysis of the preliminary WA69 data taken in December 1983.

No portion of the work referred to in this thesis has been submitted in support of an application for another degree at this or any other university.

CHAPTER I

PHOTOPRODUCTION

Chapter I

1 - Photoproduction

1.1 - Introduction

Photons are thought of as neutral point-like particles which mediate electromagnetic interactions, although above about 1 MeV they cease to behave as point-like objects, due to virtual pair production. As the photon propagates through space it can make transitions to virtual e^+e^- pairs, which by the Heisenburg Uncertainty Principle (and more accurately described by QED) can exist for a short time before reverting back to the photon. At energies above about 500 MeV the photon also exhibits a behaviour similar to a hadron of the same energy. The process by which the photon couples to hadrons is usually described by the vector dominance model where the photon with $J^P = 1^-$ couples to neutral vector mesons (ρ, ω, ϕ, J/ψ, $\cdots$) which then interact with the proton. Although the general features of photon-vector meson-proton scattering are similar to those of hadron-proton scattering but with smaller cross-sections, details of the interactions will be different due to the different quantum numbers of the projectile compared with those of the usual beam hadrons and the short life-time of the vector mesons.

Photoproduction experiments are used to investigate these vector mesons, which are produced in large quantities by diffractive processes. Charm production can also be studied in photoproduction since the production of $c\bar{c}$ pairs in the form of J/ψ is as probable as production of the lighter quark-antiquark pairs.

Chapter I

Inclusive photoproduction can be used to compare photoproduction and hadroproduction and can be used to study these interactions in terms of the quark fusion model; inclusive vector meson production can also give information on the quark content of the photon through leading particle effects.

In the analysis presented in this thesis three aspects of the photoproduction from protons are investigated in the photon energy range 70-170 GeV. The inclusive photoproduction of single charged pions is studied,

$$\gamma + P \longrightarrow \pi^{\pm} + X$$

and comparisons made with inclusive pion production in hadron scattering. The scaling properties of the single particle production distributions and the multiplicity distributions are investigated. The inclusive photoproduction of the $\rho(770)$ meson,

$$\gamma + P \longrightarrow \rho + X$$
$$\qquad\qquad\quad \big| \longrightarrow \pi^{+}\pi^{-}.$$

is also considered and compared with its photoproduction at lower energies. Finally, the elastic photoproduction of the vector meson $\rho'(1600)$ is investigated through its decay into four charged pions,

$$\gamma + P \longrightarrow \rho' + P$$
$$\qquad\qquad\quad \big| \longrightarrow \pi^{+}\pi^{-}\pi^{+}\pi^{-}.$$

1.2 - Photons and the Vector Dominance Model

In many respects the interactions of photons with nucleons are similar to the interactions of hadrons with nucleons. The hadronic nature of the photon only becomes visible once the dominant electromagnetic interactions have been taken into account. These electromagnetic interactions are dominated by pair production and have a large cross-section of ≈ 20 mb. The total hadronic cross-section (Fig. 1.1, and Ref. 1-1) for photons on a hydrogen target is by contrast ≈ 120 μb and shows many similar features to the total cross-sections for incident hadrons. The total hadronic cross-section for incident photons shows resonant structures at low photon energies ($\sqrt{s} \lesssim 3$ GeV) and flattens out to a smooth constant cross-section at higher energies. The major difference between the photon hadronic cross-section and the hadron cross-section is that the photon hadronic cross-section is a factor of 200 less.

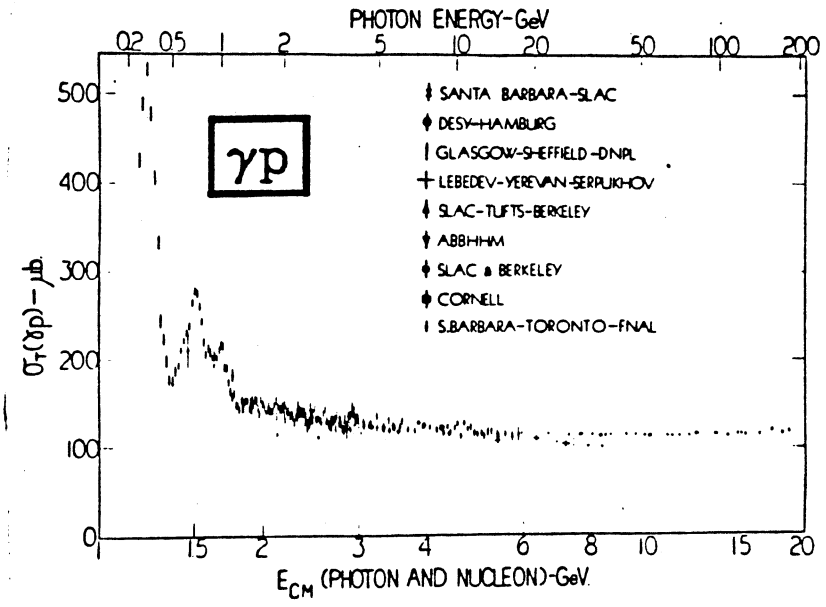

Fig. 1.1 Total hadronic Photon-Proton Cross-Section

This hadronic nature of the photon can be understood if a photon couples first electromagnetically to a hadron, which then interacts with the proton target hadronically. The photon has spin parity $J^P = 1^-$, so any hadron coupling electromagnetically to the photon must also have $J^P = 1^-$. The neutral vector mesons ρ, ω, ϕ, and J/ψ satisfy this requirement. These vector mesons, in terms of the quark model are bound state $q\bar{q}$ pairs with their spins aligned. In the vector meson dominance model the photon makes transitions to virtual, neutral vector mesons in the same way as it can make transitions to virtual e^+e^- pairs. The total hadronic photon-proton cross-section is then given in terms of the cross-sections for the vector mesons on protons with a coupling strength of $4\pi\alpha/g_v^2$,

$$\sigma(\gamma P) = \alpha \sum_v (4\pi/g_v^2)\, \sigma(vP).$$

The coupling constant $g_v^2/4\pi$ has been measured in many different experiments for many of the vector mesons and is consistent with predictions obtained using the quark model. Table 1.2 summarises some of the properties of the vector mesons. All the vector mesons with mass up to the centre of mass energy will contribute to the sum above. In the energy range of this experiment the ρ, ω, ϕ and J/ψ and their radial excitations will contribute to the total cross-section and at photon energies above 100 Gev there will also be a contribution from the Y.

Vector Meson	Quark Content	Coupling Constant (theory)	Coupling Constant (exp. e^+e^-)	Coupling Constant (exp. γp)
Rho	$\sqrt{\frac{1}{2}}(u\bar{u}-d\bar{d})$	1.21	0.64	0.61
Omega	$\sqrt{\frac{1}{2}}(u\bar{u}+d\bar{d})$	10.9	4.6	9.6
Phi	$s\bar{s}$	5.45	2.8	5.9

Fig. 1.2 Properties of Vector Mesons

1.3 - Diffractive Photoproduction of Vector Mesons

Photons in the form of vector mesons can diffractively scatter off protons and become real. The real vector meson will then typically decay hadronically to a small number of pions and kaons.

Diffractive scattering is an elastic process characterised by sharp forward peaking in the angular distribution of the final state particles with the total and differential cross-sections roughly constant with energy. The diffractive behaviour can be considered as the exchange of a series of virtual particles in the t-channel, with the same quantum numbers as the vacuum (B=0,S=0,C=0,I=0,J=0).

This series of particles can be interpreted in terms of the Regge Theory (Ref. 1-2). In this model the series of particles (poles) lie on a well defined trajectory describing the relationship between the spin and mass of the particles. Using the ideas of crossing symmetry the t-channel exchange particles are the same as the s-channel resonances seen at low energy. In the case of diffractive scattering the exchanged particles lie on the Pomeranchuk trajectory.

Diffractive photoproduction can be used to study the vector mesons because of the clear signature of the reaction; low multiplicity and energy balance between the in-coming photon and out going forward mesons (because the recoil proton takes very little energy). The ground state vector mesons (ρ, ω, ϕ, J/ψ and Υ) have been well established in both photoproduction and electron-positron annihilation experiments. Radial excitations of the vector mesons are predicted by both the quark model and in Regge theory (in which they are said to lie on daughter trajectories parallel to the vector meson trajectories). The radial excitations of the high mass vector mesons J/ψ and Υ are well established from electron-positron annihilation experiments. At the lower masses, the radial excitations of the ρ, ω and ϕ are less well established, but have been seen in photoproduction and electron-positron annihilation experiments. The first radial excitation on the ρ was thought to have a mass of 1·25 GeV but it is now believed to be at 1·6 GeV, but further experimental evidence is needed to fully establish the state. Table 1.3 summarises the masses and widths of the vector mesons and their radial excitations.

Vector Meson	Quark Content	Radial Excitation	Mass (MeV)	Width (MeV)
Rho	$\sqrt{\frac{1}{2}}(u\bar{u}-d\bar{d})$	1 2	770 1600	145 400
Omega	$\sqrt{\frac{1}{2}}(u\bar{u}+d\bar{d})$	1 2	783 1670	10 166
Phi	$s\bar{s}$	1 2	1020 1684	4.2 126
$J\psi$	$c\bar{c}$	1 2 3 4 5	3097 3770 4030 4160 4415	.063 25 52 78 43
Upsilon	$b\bar{b}$	1 2 3 4	9456 10020 10347 10570	.042 .03 ? 14
Top	$t\bar{t}$	1	?	?

Fig. 1.3 Properties of Vector Mesons and Their Radial Excitations

1.4 - Inclusive Single Particle Photoproduction and KNO Scaling

Scaling in high energy particle physics is normally associated with deep inelastic lepton scattering (Ref. 1-3) in the reaction:

$$l + P \longrightarrow l + X$$

The point-like nature of the partons (quarks) in the proton imposes constraints on the energy and angle of the scattered leptons. These constraints depend only on the energy of the incident leptons and the process is said to scale because the cross-section does not depend on

any distance or mass scale to do with the proton. As the Q^2 of the scattering increases the effective wave-length of the virtual photon probe decreases and if the partons cease to behave as point-like objects the scaling will be broken. At even higher Q^2 new point like pre-partons may be resolved and a new set of scaling distributions would be found.

A similar effect takes place in inelastic hadron-hadron interactions:

$$h + P \longrightarrow h + X$$

In this case the single particle distributions have a smooth regular dependence on the centre of mass energy and do not depend on a distance or mass scale within the hadrons. In the language of lepton scattering inelastic hadron-hadron interactions may be regarded as inelastic quark scattering off hadrons. The single particle scaling is described in terms of the single particle differential cross-section $d^3\sigma/dX_f dP_t^2$ using the single particle Feynman function

$$F(X_f, P_t) = \frac{1}{\sigma_{tot}(s)} \cdot \frac{2E^*}{\sqrt{s}} \cdot \frac{d^3\sigma}{dX_f dP_t^2},$$

where E^* is the energy of particle, P_t is the transverse momentum and X_f is the longitudinal momentum fraction ($X_f = 2P_l^*/\sqrt{s}$) of the particle in the centre of mass system. The Feynman function $F(X_f, P_t)$ eventually becomes independent of the centre of mass energy $\sqrt{s}$ as s increases (Ref. 1-4).

By extending the ideas of single particle scaling to multiple particle systems, the multiple particle Feynman functions can be defined as

$$F^{(m)}(X_{fi},P_{ti}) = \frac{1}{\sigma_{tot}(s)} \prod_i \frac{2E^*_i}{(\sqrt{s})^m} \cdot \frac{d\sigma^{3m}}{dX_{fi}dP^2_{ti}}, \quad i = 1,\cdots,m,$$

where m is the number of particles considered and i the index of the individual particles. These functions will become scale independent if they asymptotically approach a constant value at large s without any variation of the form ln(s). With this assumption and the additional assumption that they are non-singular at $X_{fi} = 0{\cdot}0$, these multiple particle Feynman functions can be integrated over the transverse momentum and Feynman X of all the particles and the moments of the multiplicity distribution

$$C_k(s) = \sum_k \frac{n^k}{\langle n \rangle^k} P_n(s)$$

can be calculated, where k is the order of the moment and $P_n(s)$ the probability of getting n particles in the final state. The multiplicity probability distribution can be written in the form

$$P_n(s) = \frac{\sigma_n(s)}{\sigma_{tot}(s)},$$

where $\sigma_n(s)$ and $\sigma_{tot}(s)$ are the multiplicity n and all multiplicity cross sections respectively at the centre of mass energy $\sqrt{s}$. Using the scale independance of the moments of the multiplicity distribution it has been shown that not only does the mean multiplicity ($\langle n \rangle$) scale (as constant×Ln(s)) but also that the shape of the multiplicity distribution is constant. This multiple

particle scaling has become known as KNO scaling after the authors of the original paper on the subject (Ref. 1-5). This can be expressed in the form

$$P_n(s) = \frac{1}{\langle n \rangle} \cdot \psi\left[\frac{n}{\langle n \rangle}\right],$$

where the KNO scaling function $\psi(z)$ has no explicit dependence on the centre of mass energy $\sqrt{s}$ except through the reduced multiplicity

$$z = \frac{n}{\langle n \rangle}.$$

Using an analagous argument it can also be shown that these scaling rules also hold when the particles are classified according to type, thus

$$P_{ni}(s) = \frac{\sigma_{ni}(s)}{\sigma_{tot}(s)} = \frac{1}{\prod_i \langle n_i \rangle} \cdot \psi\left[\frac{n_i}{\langle n_i \rangle}\right]$$

where there are n_i particles of type i. The multiplicity distributions for individual types of particles would then also scale. In particular, if the selection is made according to the charge of a particle then the charge-multiplicity distributions will then obey the KNO scaling rules,

$$P_{nc}(s) = \frac{\sigma_{nc}(s)}{\sigma_{tot}(s)} = \frac{1}{\langle n_c \rangle} \cdot \psi\left[\frac{n_c}{\langle n_c \rangle}\right].$$

The functional form of $\Psi(z)$ will in general be different for different inelastic interactions and different choices of the types of particles studied. Using statistical models for inelastic interactions the KNO scaling function $\Psi(z)$ has been predicted for hadron-hadron collisions, deep inelastic lepton scattering and e^+e^- collisions (Ref. 1-6). The hadron-hadron model can also be applied to inelastic γP and soft inelastic e^-P interactions because through the vector dominance model, the real and low Q^2 photons behave as hadrons. The model considers the beam and target hadrons as spatially extended bodies with many degrees of freedom. When these bodies interact the energy is distributed into three regions; a beam region, a target region and a central region. In each of these regions a highly excited body (known as a 'fire ball') is formed which decays to multi hadron systems. Using this 'Three-Fireball' model the KNO scaling function was predicted to be

$$\Psi(z) = \frac{16}{5} (3z)^5 e^{-6z}.$$

It is traditional in KNO scaling involving only charged particle to normalise $\Psi(z)$ to 2 because charged particles are only producted in pairs. Hence, in complete γp events only the odd multiplicities are populated, so that $\Sigma P_{n(odd)}$ is normalised to 1. Figure 1.4 shows the scaling function $\Psi(z)$ deduced from hadron-proton scattering, from low Q^2 electron-proton and low energy photon-proton scattering. The predicted scaling function, from the model discribed above is plotted as a solid line.

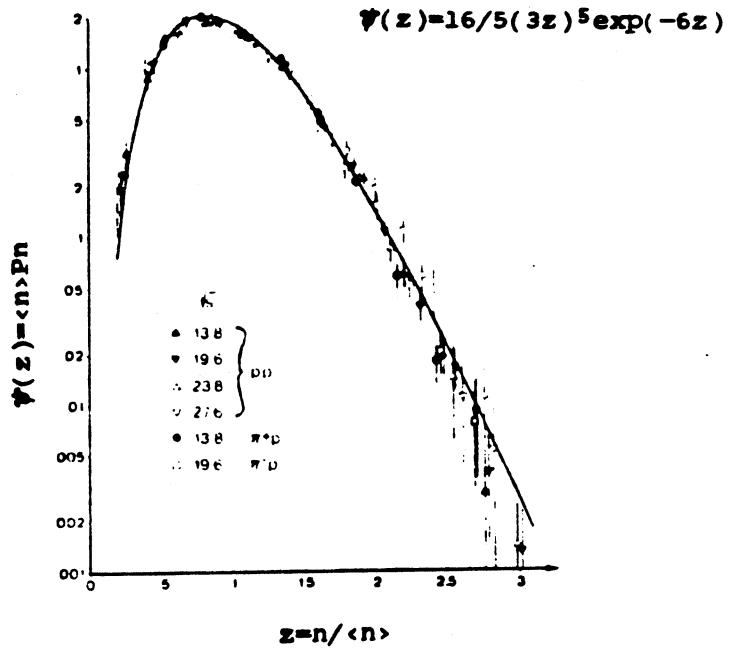

γp
e⁻p(small Q^2) } nondiffractive

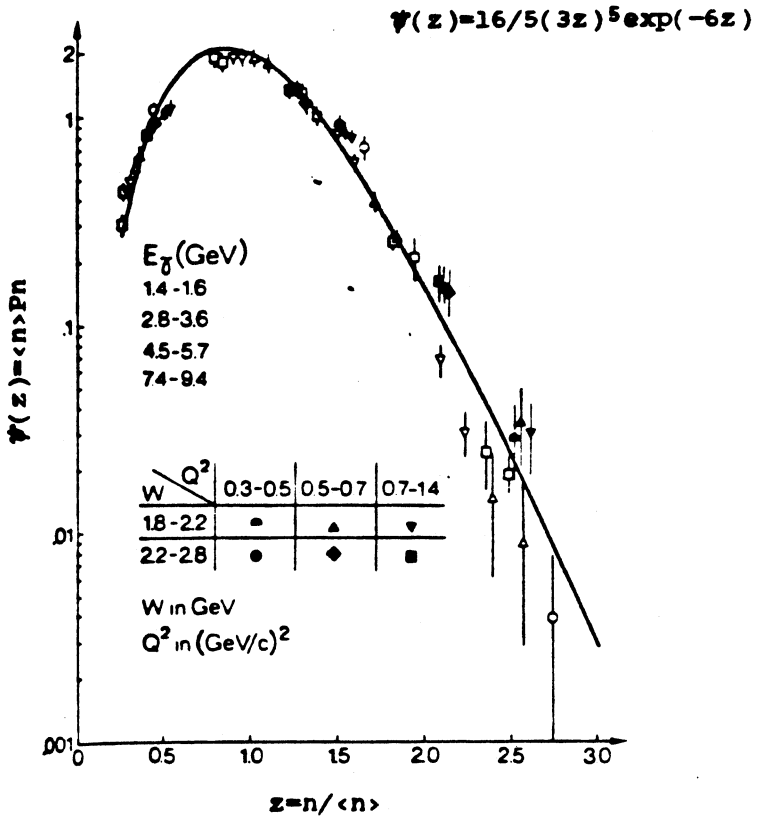

Fig. 1.4 Hadronic KNO Scaling

1.5 - Inclusive Vector Meson Photoproduction

In the inclusive photoproduction of vector mesons there are two possible reaction mechanisms. It is possible for vector mesons to be produced by double diffractive dissociation. In this process the vector meson is produced and decays to pions in the forward direction in a similar way to elastic vector meson production, and in the backward direction, unlike the elastic case, the proton fragments into hadrons. The other process producing vector mesons is quark fusion, where a quark in the photon (in the form of a vector meson) fuses with a quark from the proton. This process gives rise to production of vector mesons in the central region. It has been shown at lower energies that inclusive vector meson photoproduction in the central region is similar to pion induced vector meson production (Ref. 1-7 and Ref. 1-8).

The diffractive component can be estimated using Pomeron dominance in the Triple-Regge formalism (Fig. 1.5). Using this approximation the diffractive component of the inclusive cross-section is given by

$$\frac{d^2\sigma_D}{dtdX_f} = \frac{\beta_{ppP}(0)\beta^2_{\gamma VP}(t)G_{ppp}}{16(1-X_f)},$$

where β_{ppP} and $\beta_{\gamma pv}$ are the proton-proton-pomeron and photon-pomeron-vector meson vertex factors and G_{ppp} is the triple pomeron vertex factor. This gives a prediction that

$$\frac{2E^*}{\sqrt{s}} \cdot \frac{d\sigma_D}{dX_f} \sim \frac{2E^*}{\sqrt{s}} \cdot \frac{1}{(1-X_f)}.$$

The diffractive component has been calculated for ρ^0 and ω inclusive photoproduction using this model and has been compared with inclusive photoproduction data at 20 - 70 GeV (Ref. 1-7). This comparison is shown in Figure 1.6 with the prediction as a band.

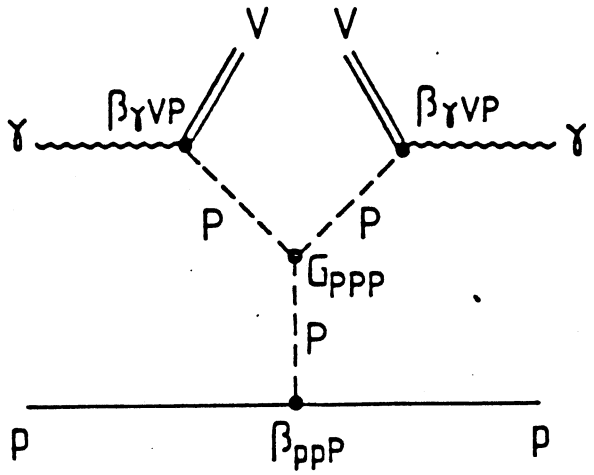

Fig. 1.5 Diagram for Diffractive Vector Meson Photoproduction

The non-diffractive component can be estimated using the quark fusion model (Ref. 1-8), from the structure functions of the quarks in the photon $(F_\gamma^q, F_\gamma^{\bar{q}})$ and proton $(F_p^q, F_p^{\bar{q}})$.

$$\frac{2E^*}{\sqrt{s}} \cdot \frac{d\sigma_N}{dX_f} = \left[\frac{4\pi^3}{3m_c^2}\right] \Sigma_q \left[\frac{g_q^2}{4\pi}\right] \left[F_\gamma^q(X_1)F_p^{\bar{q}}(X_2) + F_\gamma^{\bar{q}}(X_1)F_p^q(X_2)\right],$$

where $g_q^2/4\pi$ is the coupling constant between the $q\bar{q}$ and the vector meson and X_1 and X_2 are the fractional momenta of the quarks in the photon and proton respectively, where

$$X_1 - X_2 = X_f \quad \text{and} \quad X_1 \cdot X_2 = M_V^2/s.$$

Because of this constraint forward vector meson production at high energy is dominated by fusion of the high X quarks (valence quarks) in the photon and low X quarks (sea quarks) in the proton. Since the quark and anti-quark distributions in the photon must be equal and writing the proton structure function in terms of valence and sea contributions, the non-diffractive component of the inclusive vector meson distribution may be parameterized;

$$\frac{2E^*}{\sqrt{s}} \cdot \frac{d\sigma_N}{dX_f} \sim F_\gamma^q(X_1) \left[\alpha F_p^v(X_2) + \beta F_p^s(X_2) \right],$$

Taking the quark distribution in the photon (F_γ^q) to be the same as that in the pion ($\sim X(X-1)$) and suitable distributions for the valence and sea quarks in the proton (F_p^v and F_p^s) predictions for the vector meson distributions have been made. These predictions have been compared with ρ^0, ρ^+ and ρ^- inclusive photoproduction in the energy range 20 - 70 GeV (Ref 1-7) and are shown in Figure 1.7.

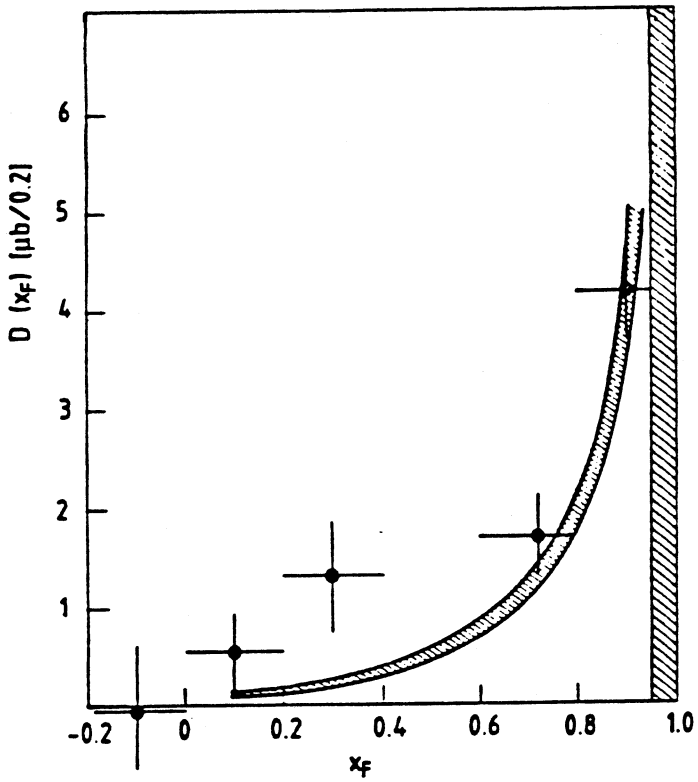

Fig. 1.6 Diffractive Component of Inclusive Vector Meson Photoproduction

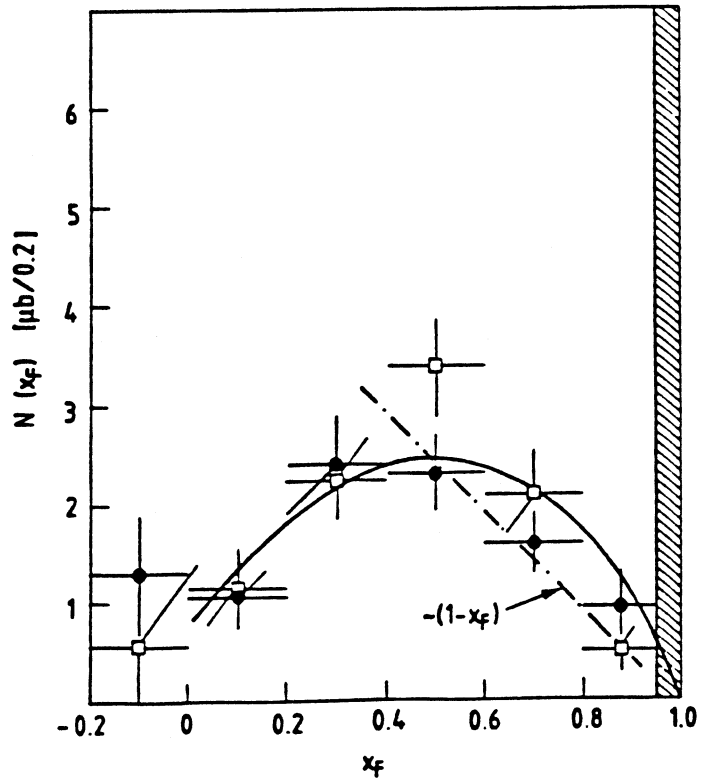

Fig. 1.7 The Non-Diffractice Component of Inclusive Vector Meson Production

1.6 - Conclusion

Photons can make transitions to virtual vector mesons which can interact with protons hadronically. The process of photons coupling to vector mesons is well described by the vector dominance model for both real and virtual photons. The vector mesons produced by the vector meson dominance model can interact with a proton target either elastically or inelastically. In elastic scattering the virtual vector meson scatters and becomes real by a diffractive mechanism and this gives rise to a small number of forwardly produced scalar mesons from the decay of the vector meson. Elastic scattering accounts for $\approx$ 20 μb of the total hadronic photon cross section of 120 μb in the photon energy range 70 - 200 GeV. Almost all of the rest of the hadronic cross section is characterised by soft inelastic scattering. At lower photon energies it has been shown that the soft inelastic scattering is similar to that in meson-proton, proton-proton and proton-antiproton scattering. This similarity shows up in the single particle inclusive Feynman-X distributions (or equivalently the rapidity distributions) and in the shape of the multiplicity distributions, as well as in the Ln(s) behaviour of the mean multiplicity. Within the inelastic portion of the photon-proton cross-section vector mesons can be produced. The inclusive vector meson production has two components. The first component is due to double diffractive dissociation and is similar to elastic-diffractive production of vector mesons. The second component is due to fusion of leading quarks in the photon with the quarks in the proton.

1.7 - References

1-1 Particle Properties Data Book
Particle Data Group CERN and Berkeley labs
25 th edition April 1982

1-2 Elementary Particle Physics Chapt. 20
D. C. Cheng and G. K. O'Neil
Addison-Wesley Publishing Company 1979

1-3 An Introduction to Quarks and Partons
P. Close Academic Press 1979

1-4 Very High-Energy Collisions of Hadrons
R. P. Feynman
Phys. Rev. Lett. 23 (1969) 1415

1-5 Scaling of Multiplicity Distributions in
High Energy Hadron Collisions
Z. Koba, H. B. Nielsen and P. Olesen
Nucl. Phys. B40 (1972) 317-334

1-6 Koba-Nielsen-Olesen Scaling and Production
Mechanism in High-Energy Collisions
C. Kuang-chao, L. Lian-sou and M. Ta-chung
Phys. Rev. D 28 1080 (1983)

1.7 Koba-Nielsen-Olesen Scaling and Rapidity
distributions in Nondiffractive Hadron Reactions
Cai Xu, Liu Lian-sou and Meng Ta-chung
Phys. Rev. D 29 869 (1984)

1-7 Inclusive Photoproduction of ρ and ω in the
Photon Energy Range 20 to 70 GeV
M. Atkinson et al CERN-EP/84-30
(Submitted to Nucl. Phys. B)

1-8 Inclusive Photoproduction of γ in the
Photon Energy Range 20 to 70 GeV
M. Atkinson et al Nucl. Phys. B179 (1981) 215

1.8 - Figure Captions

1.1 Total hadronic Photon-Proton Cross-Section

1.2 Properties of Vector Mesons

1.2 Properties of Vector Mesons

1.4 Hadronic KNO Scaling

1.5 Diagram for Diffractive Vector Meson Photoproduction

1.6 Diffractive Component of Inclusive Vector Meson Photoproduction

1.7 The Non-Diffractice Component of Inclusive Vector Meson Production

CHAPTER II

THE BEAM LINE AND

TAGGING SYSTEM

Chapter II

2 - The Beam Line and Tagging System

2.1 - Introduction

The incident photon beam was derived from a 200 GeV/c electron beam using Bremsstrahlung in a thin heavy metal target (the Tagging Target). In order to measure the energy of each photon it was necessary to measure the momentum of the beam and scattered electrons. The electron beam spectrometer was used to measure the momentum and trajectory of each electron in the beam. This spectrometer consisted of three assemblies of MWPC's (Multi-Wire Proportional Chambers) and beam scintillation counter hodoscopes with a series of bending magnets between the first two of these assemblies. The forward scattered, reduced energy electrons from the Tagging Target were deflected out of the photon beam into an array of MWPC's, a pair of scintillation counter hodoscopes and an array of lead glass shower counters. Reconstruction of the trajectory of the scattered electron from the tagging MWPC's together with the incident electron from the beam spectrometer enabled the calculation of the energy of each tagged photon. Fast signals from the lead glass and scintillation counter hodoscopes provided a fast trigger for the experiment corresponding to a 'tagged photon' entering the liquid hydrogen target in Omega.

The measurement of the photon energy enabled quantities involved in photoproduction to be measured as a function of energy. The precise measurement also allowed preferential selection of elastic physics channels. If all the particles in the final state were

detected, the energy loss (Ediff) between the photon beam and final state particles would be consistent with zero. This selection of elastic events was used to enhance the diffractive fraction of the data. In this class of events the photon produces a vector meson which interacts diffractively with the proton, producing a few forward mesons from the vector meson decay and a low energy (possibly unseen) recoil proton.

The electron beam used in this experiment was derived from the E1/H1/P1 beam line (Fig. 2.1), in the up-graded West Hall at CERN (Ref. 2-1). In electron mode this beam line was capable of transporting 200 GeV/c electrons with an intensity of 5×10^{6} for 2×10^{12} incident protons per SPS spill. The electrons were produced by irradiating the primary target (T1) with an Extracted Proton Beam (EPB) from the SPS. From the secondary particles produced in this target the electron beam was created. High energy electrons were then selected with a momentum ≈ 200 GeV ±2% and transported into the West Hall and towards Omega. The last two bends of the beam line also served as the Beam Spectrometer and Tagging System bends respectively.

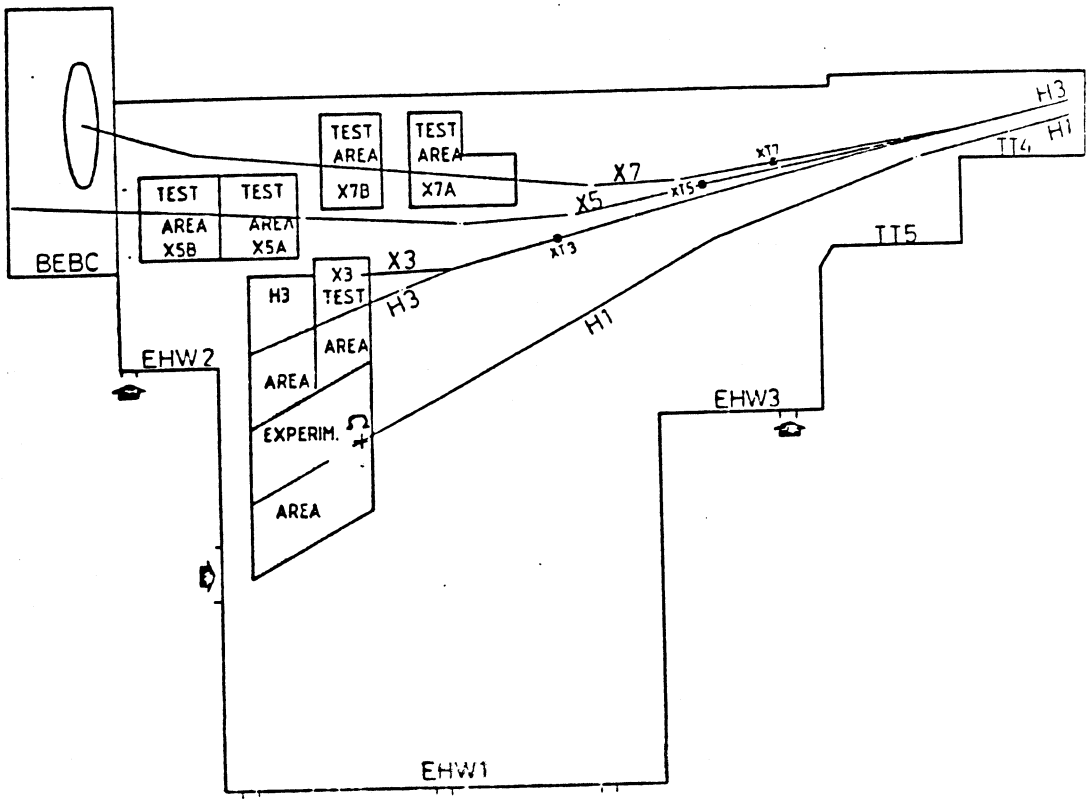

Fig. 2.1 The Layout of the Upgraded West Hall

2.2 - The Beam Line

Simultaneous slow extraction of protons at 450 GeV from the SPS to the North and West Areas made it possible for experiments to run in both parts of CERN together. At the West Area Switch Yard (TCC6) the EPB for the West Area was focussed on to the primary Target T1 (0·5 of a radiation length of beryllium). From this target two secondary beams were extracted. The E1/H1/P1 beam line was provided for the Omega facility and the H3 beam line for other West Hall users. In an attempt to decouple the particle types and momenta in the H1 and H3 beam line a Wobbling Station (Fig. 2.2) was set up round the target area. The Wobbling Station allowed the angle of the incident EPB on the target to be varied, hence controlling the production angle of the two beams. In electron mode bend 3 of the Wobbling Station was used to select photons from the decay of neutral pions from the primary target. The photons were converted into e^+e^- pairs in a silicon crystal target, from which electrons were selected for the beam. An electron beam was chosen in preference to a positron beam to avoid contamination of protons. Backgrounds were further reduced by having the target station deep underground and on a different plane to the West Hall Experiments.

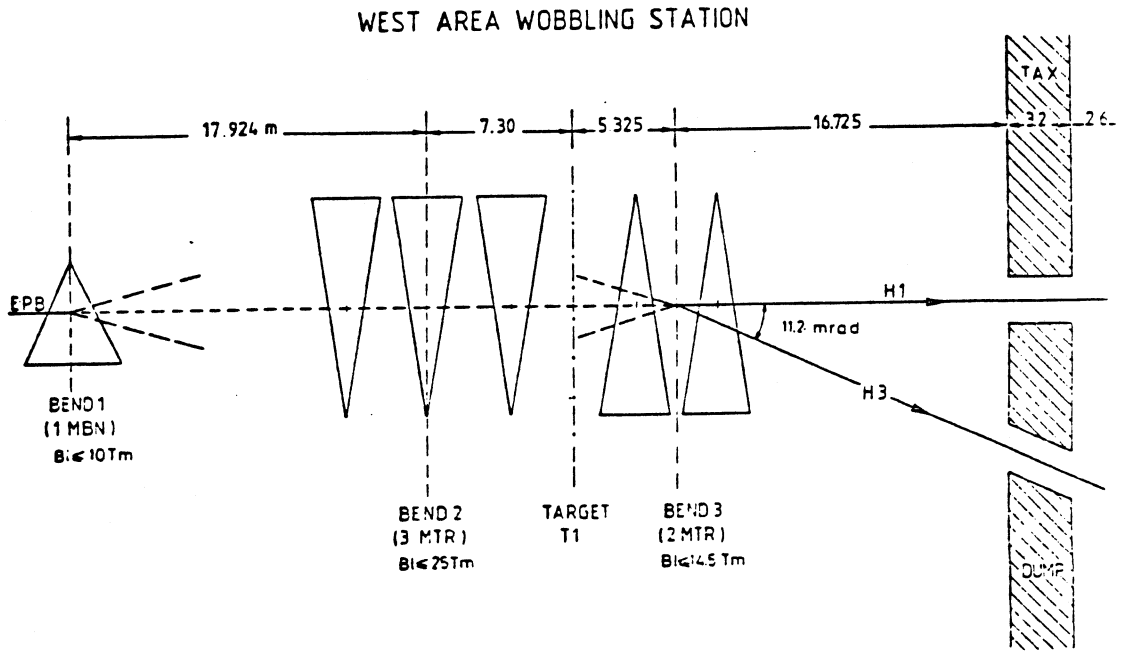

Fig. 2.2 The West Area Wobbling Station

The front end optics of the E1 beam line was used to defined the acceptance and the momentum bite of the beam. The bending magnets in bend 2 were used to bring the beam into the transfer tunnel TT61 (Fig. 2.3a). At the top of the transfer tunnel bend 3 was used to corrected the vertical deflection caused by bend 2. The remaining vertical bends in the beam line (Fig. 2.3b) brought the beam horizontally into the West Hall. The horizontal bends 6 to 10 were used to bend the beam south towards Omega and away from the H3 beam line. The quadrupole magnets in this region served to increase the beam size for the beam spectrometer (see section 2.3) to improve the spatial resolution and reduce saturation effects in the MWPC's and then focus the beam on to the hydrogen target. Bend 9 was used for the momentum resolving part of the beam spectrometer.

Horizontal Beam Profile /mm.

a/

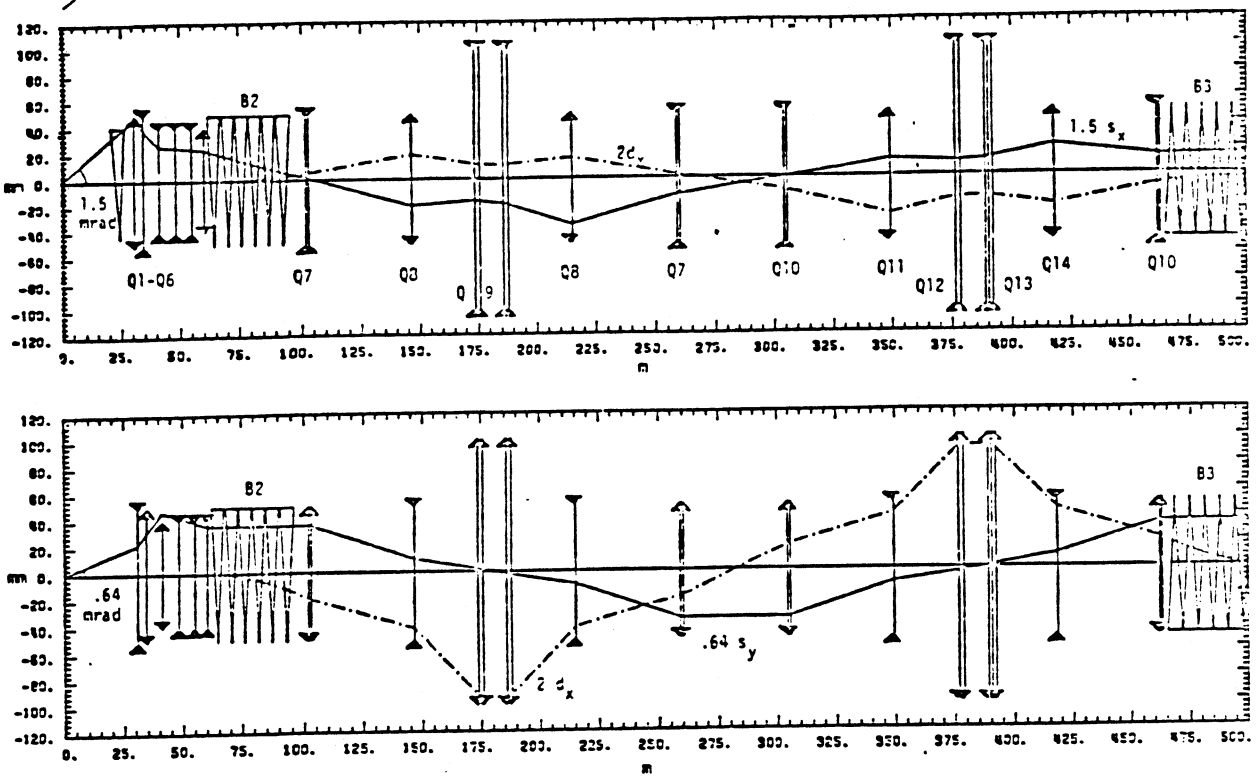

Vertical Beam Profile /mm.

Horizontal Beam Profile /mm.

b/

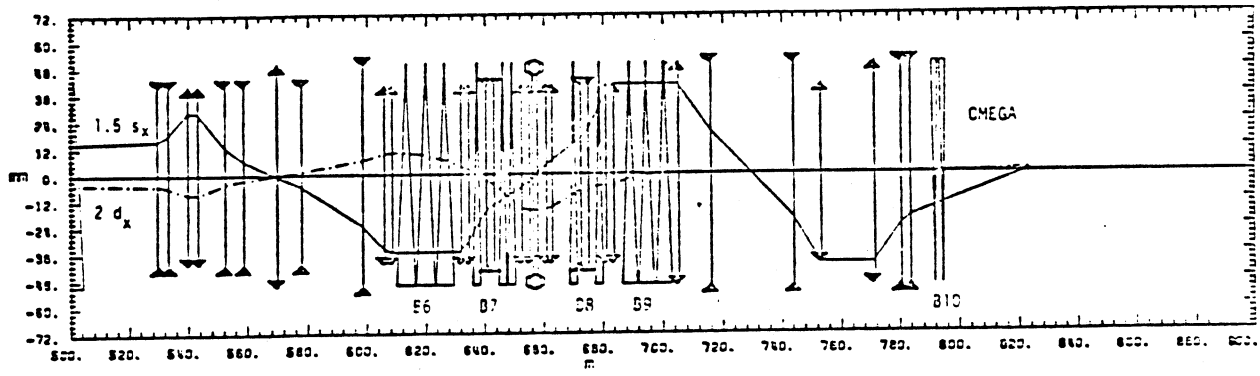

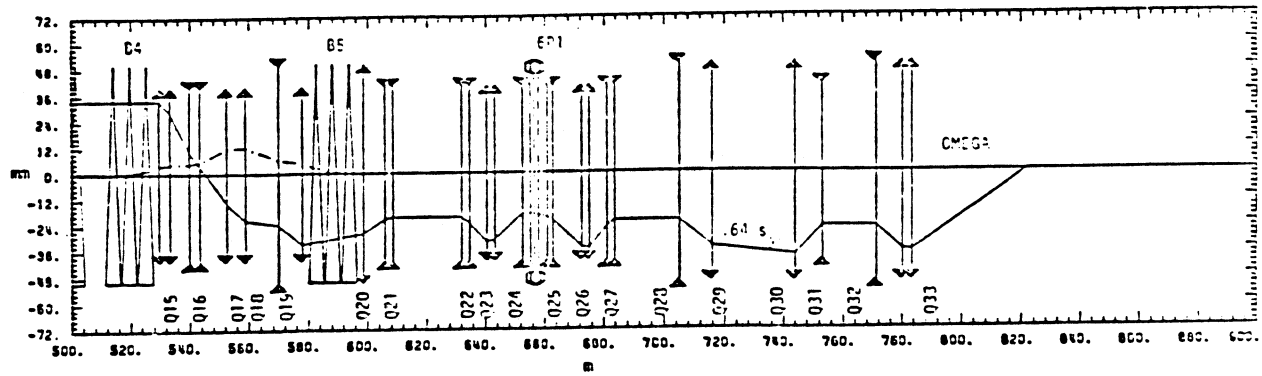

Vertical Beam Profile /mm.

Fig. 2.3 The H1/E1/P1 Beam Line

In our photon mode bend 10, tagging magnets were set to deflect the unscattered electron beam into a beam dump in front of Omega and to allow the photons produced in the tagging target (between the tagging magnets) to enter Omega. The H1 beam line parameters are summarised in table 2.4.

Maximum momentum	450 GeV/c
Horizontal Acceptance	1.5 mrad at 200 GeV/c
Vertical Acceptance	0.64 mrad at 200 GeV/c
Solid Angle	3.0 μsr at 200 GeV/c 2.1 μsr at 350 GeV/c
Momentum bite	± 2 %
Dispersion at momentum slit	47 mm/%
Intrinsic momentum resolution	± .08 % at 1 sigma
Spectrometer resolution	.05 - .08 % for hadrons
Beam height in EHW1	3.66 m
Beam length	822 m
Particle Identification	2 CEDAR's

Fig. 2.4 Parameters of the H1/E1/P1 Beam Line

For setting up and controlling the beam line elements, the beam line was instrumented (independently of the experiment) with a series of beam profile counters and trigger counters. These detectors (provided by the EA division at CERN) were controlled and read out using an EA division NORD computer. This computer also controlled the magnet and collimator settings, which made it possible to monitor the beam while varying their settings. Communication with and control of the beam line was derived through the interactive program TREE (Ref. 2-2) running on the EA's NORD.

The intensity of the secondary beams as calculated using a modified Hagedon-Ranft model (Ref. 2-3, Fig. 2.5) predicted an intensity of about $1 \cdot 7 \times 10^6$ electrons at 200 GeV per burst for 10^{12} protons at 450 GeV on the primary target. It was found that the actual electron intensity was about $1 \cdot 2 \times 10^6$ for 10^{12} protons with the original lead converter. However, using the silicon crystal converter the design intensity was realised. This improvement was due to coherent pair production in the crystal. Calculations showed that the loss of energy due to synchrotron radiation in the beam magnets should be about 6 GeV ±0·22 GeV at 200 GeV for this electron beam. Thus, as the beam started off at 200 GeV the magnet currents had to be gradually reduced from their 200 GeV equivalent pion mode settings to allow for the 6 GeV loss.

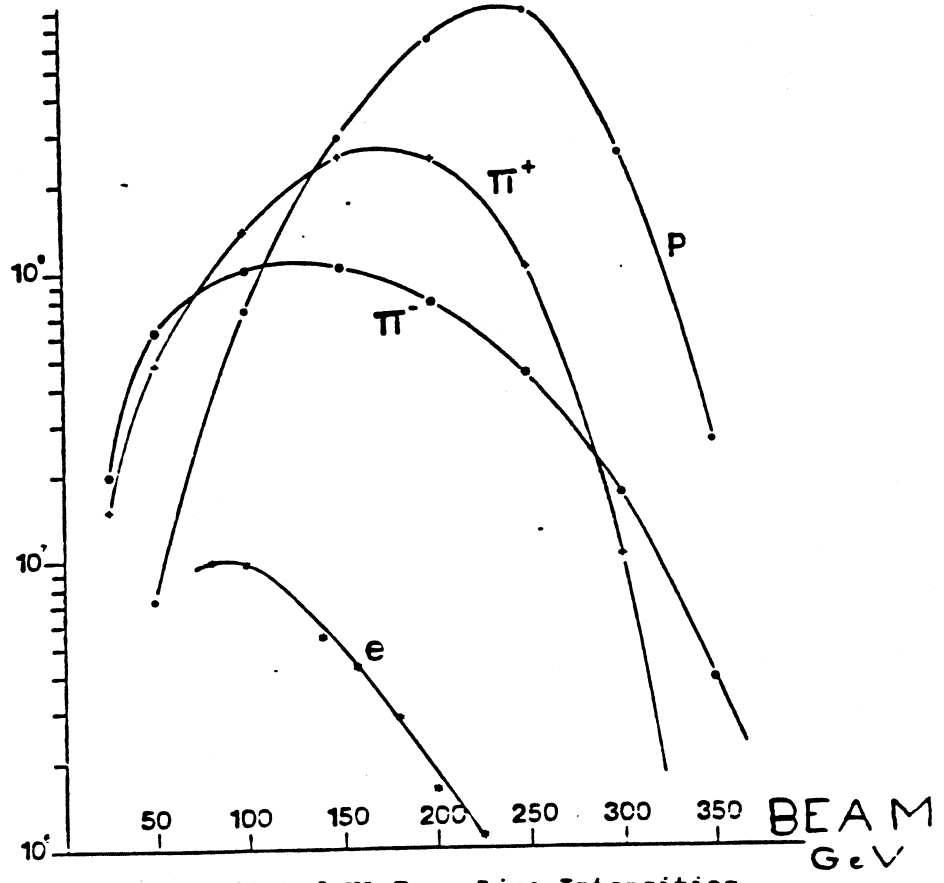

Fig. 2.5 Predicted H1 Beam Line Intensities

2.3 - The Beam Spectrometer

The beam spectrometer consisted of three regions containing the beam profile detectors, and the bending magnets, bend 9 (Fig. 2.6). Region 1 and Region 2 together with the horizontal bend, bend 9, provided the momentum sensitive part of the beam spectrometer. Region 2, the straight part of the beam line and Region 3 provided the position sensitive part of the spectrometer, used to predict the interaction point at the tagging target and its projection in to Omega.

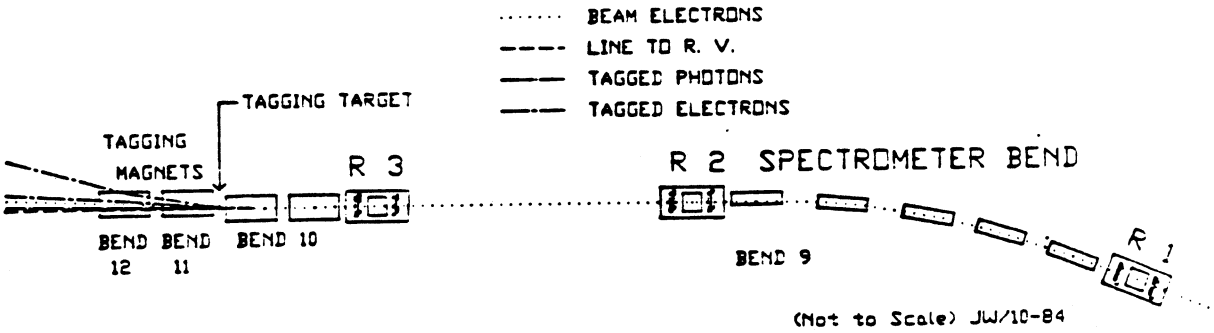

Fig. 2.6 The Beam Spectrometer

In each of the Regions 1, 2 and 3 the beam profile detectors consisted of a set of 8 MWPC planes and two planes of scintillation counter hodoscopes (Fig. 2.7). Each MWPC plane had 96 wires at 1 mm spacing. The wire chambers were mounted in orthogonal pairs in screened boxes together with their associated electronics (amplifiers, discriminators and MECL line drivers). The chambers were mounted in the region with four chambers in front of the hodoscopes and four behind. The chambers were arranged in the order Y(0°), Z(90°), U(-45°), V(+45°) in the direction of the beam. Due to experience in previous experiments using these chambers (Ref. 2-4) it was found necessary to run them on a gas mixture of Argon, Isobutane, Freon and Meythalal (Magic gas), with the cathode planes between 4·0 and 5·0 KV to allow the chambers to run on plateau. This gave good efficiency (98%) in the chambers and a long life despite the high flux rate through the chambers (about 10^6 electrons $cm^{-2}s^{-1}$). The signals from the chambers were delayed in twisted pair cable layed down the beam line then passed through the 'Rate Gates'. The Rate Gates were used to reduce the rate from the chambers and to select only the hits in time with interactions in Omega. The information from the chambers then passed down more delay cable to be read out using the CERN RMH (Read and Memorize Hybrids) system (Ref. 2-5).

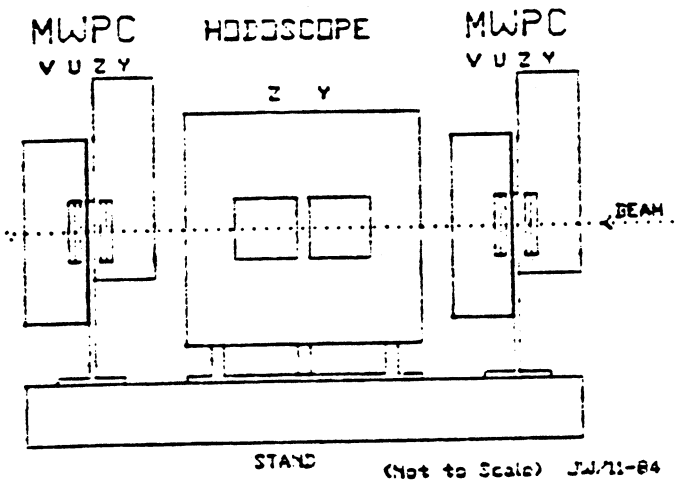

Fig. 2.7 The Layout of the Beam Profile Detectors in each Region

The scintillation counter hodoscopes consisted of two orthogonal arrays of 32 scintillator slats, each 3 mm wide and 0·5 mm thick. These slats were individually wrapped with aluminized mylar to form air light guides of about 15 mm diameter and were viewed with 19 mm Photo-multiplier tubes (EMI Type 9826b). For economy only the centre 16 vertical slats and 24 horizontal slats had photo-multiplier tubes and read out. Despite the reduction in active area the hodoscopes covered 95% of the beam. The signals from the hodoscope tubes passed through local discriminators before being sent down delay cables. They then passed through gated discriminators (serving the same purpose as the Rate Gates) before being read out using TDC's (Lecroy type 2228).

The jitter time of the MWPC signals of about 15 ns due to different arrival times at the wires, required a gate of about 25 ns to be used at the rate gates. This meant that with a high intensity beam (about 2×10^6 s^{-1}) the chance of seeing more than one track in the beam line was high. To resolve this ambiguity, 'in time' hits in the hodoscopes with a time resolution of about 2 ns were used to define areas in the MWPC's where the hits from the 'in time' track would be found. Any remaining ambiguity due either to multiple hits in the search area or failure of a hodoscope slat or MWPC wire to fire could be resolved using the ±45° wire chambers U and V as well as the 0° and 90° chambers Y and Z. This combination provided the spatial resolution of the MWPC's with the time resolution of the hodoscopes. A Channel Plate Detector is currently being developed to provide both of these features in a single detector (described in Chapter 3). Following the identification of the good chamber hits the beam line reconstruction program PEDRO (Ref. 6-4) made a fit using all these hits and the field map for the magnets in the beam line to calculate P, Y, Z, Y', Z' and their errors at the tagging target.

2.4 - The Tagging System

The tagging system (Fig. 2.8) was installed in Region 4 of the beam line just upstream of Omega. It consisted of three bending magnets (bend 10), the tagging target, the recoil electron detectors, monitors and veto counters. Electrons from the beam line passed through the first tagging magnet on to the tagging target. In the tagging target a small fraction of the electrons radiated a bremsstrahlung photon. These photons then travelled into the Omega target unaffected by the other two tagging magnets. Electrons which did not radiate a photon were deflected 2 mr by the tagging magnets, through the beam stop counters and into the beam dump. The electrons which did radiate a photon, because they had less energy, were deflected more by the tagging magnets. These electrons passed through an array of wire chambers (W4.1 to W4.5), through two planes of scintillation counter hodoscopes (H4.1 and H4.2) and then into the Lead Glass shower counter (LG). The tagging target consisted of a four headed rotating target assembly, with 3 thin metal targets of 4.2%, 7.6%, and 15% of a radiation length, the fourth head being left blank to give a null reference target.

The arrival of a photon at the hydrogen target was tagged in the sense that a signal from the scintillation counter hodoscopes (H4.1 and H4.2) and lead glass counters (LG) gave a fast trigger to the rest of the trigger logic and read out system. The scintillation counter hodoscopes and lead glass together with the field in the tagging magnets defined the range over which photons could be tagged. An electron beam energy of 194 GeV at the tagging target gave tagged

photons over the energy range 64 to 172 GeV. The tagging hodoscopes consisted of one plane (H4.2) of 16 slats of 10 mm plastic scintilator 80 mm wide, and the other plane (H4.1), 12 slats of 10 mm plastic scintillator of increasing width away from the beam giving roughly equal energy bin widths. The time reference for the whole experiment was taken from the 'OR' of the slats in H4.2. The lead glass counter consisted of three rows of lead glass blocks 80 × 80 × 400 mm^3 (13·6 radiation lengths). In the experiment only the centre row was used. The lead glass provided positive identification of the scattered particle from the tagging target as an electron and not a contaminant beam hadron.

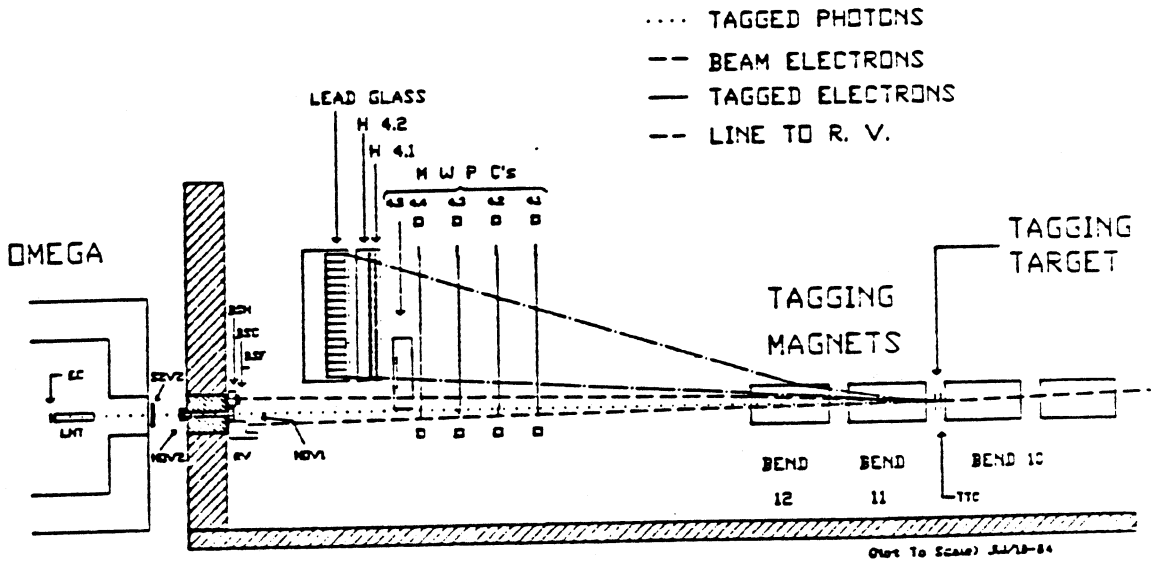

Fig. 2.8 The Layout of the Tagging System

The lead glass and tagging hodoscopes on their own provide an energy resolution of about 2 GeV. To improve this four large MWPC's were installed between the tagging magnets and hodoscopes. These chambers (W4.1 to W4.4) were 2 m long and spanned the full width of the hodoscopes and lead glass. They had vertical wires at 2 mm separation. To avoid damage in the region of the unscattered electron beam, wires were removed at the beam line side of these chambers. A fifth, smaller wire chamber (W4.5) was also installed in this region, close to the unscattered electron beam to improve the momentum resolution of the spectrometer at low photon energy (high electron momentum). This chamber was of similar design to the beam line chambers. It was 200 × 200 mm^2 with vertical and horizontal wires at 1 mm spacing. The information from the five wire chambers, the hodoscopes and the lead glass was used together with the position of the incident electron at the tagging target to reconstruct the scattered electron trajectory. This was then used to accurately calculate the photon momentum and its position at the Omega target.

The purpose of the first of the tagging magnets (upstream of the tagging target) was to separate any photons in the beam line from the electrons. These photons from synchrotron radiation in the magnets and bremsstrahlung in the chambers in Region 2 and 3 fell on to a lead scintillator sandwich shower counter, the Radiation Veto. The amount of material in the beam line in Region 2 and 3 giving rise to a false Tag signal was estimated to be about 2% of a radiation length. Two Holey Vetos were also installed in the photon beam line to remove events where the photon had the wrong direction. These counters were lead scintillator sandwiches similar to the radiation veto.

2.5 - The Tagging System Electronics

The first stage of the trigger used in this experiment consisted of forming the interaction trigger (INT). This trigger provided a fast signal to the rest of the experiment signalling the presence of a tagged photon interacting in the hydrogen target. At this stage of the trigger no attempt was made to separate the hadronic events with a cross section of 120 μb from the dominant e^+e^- pair production with a cross section of 20 mb in the hydrogen target.

The first step in the interaction trigger (Fig. 2.9) was the formation of the Quick Tag (QT). This was formed from the coincidence of the signals from the tagging hodoscopes and the lead glass.

$$QT = H4.1 \; . \; H4.2 \; . \; LG$$

This corresponded to the occurrence of an electron of lower than beam energy in the tagging system. The Quick Tag was improved by the use of the Region 4 veto counters. The radiation veto (RV) detected excessive beam energy loss due to synchrotron radiation in the magnets and early bremsstrahlung in the beam line. Its threshold was set to about 3 GeV. The holey vetos (HOV's) with holes 38 mm and 42 mm respectively ensured the photons were in-line with the hydrogen target. Finally, a charged particle veto (S2+V2) was installed between the second holey veto and the hydrogen target to veto any remaining charged particles in the photon beam.

This veto counter removed events where pairs were produced in the air, chamber walls and helium between the last tagging magnet and the hydrogen target.

$$TAG = QT.RV.\overline{HOV1}.\overline{HOV2}.\overline{S2+V2}$$

The Tag-Int was then formed from the coincidence of a Tag and a hit in the End-Cap, a 50 mm diameter circular scintillation counter mounted at the back of the hydrogen target.

$$TAG\text{-}INT = TAG \; . \; EC$$

The time reference for the experiment as mentioned earlier was taken from the 'OR' of the 16 slats H4.2. This was passed through the tagging trigger by ensuring that the front edge of the H4.2 signal defined the front edge of the interaction trigger signal. The time reference was used to provide a strobe to select only the chamber and counter digitisings corresponding to events with a tagged photon. It was also used to define a reference time for the Omega Drift Chambers, Photon Detector time-of-flight, the RICH and the beam line hodoscopes. In these detectors the time reference was used to determine the position of tracks or resolve ambiguities. To improve the time reference it may be possible to use a thick scintillation counter in front of the tagging target. This would require special electronics to cope with the high rate compared with the tag rate.

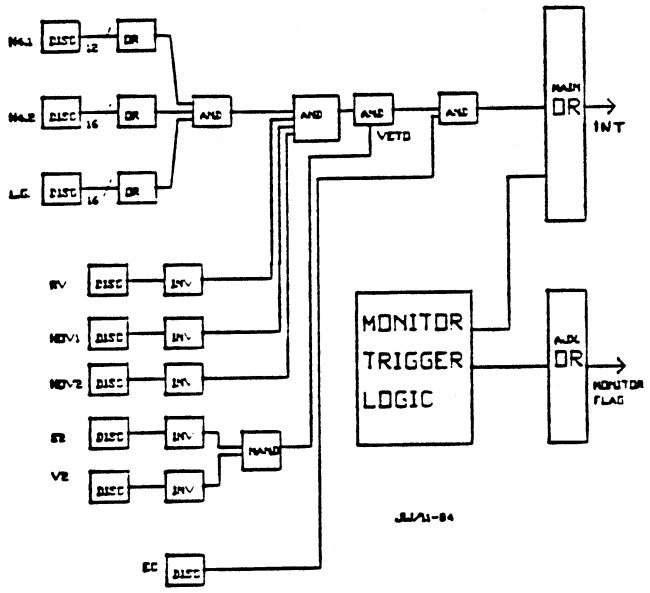

Fig. 2.9 The Interaction Trigger

At this stage various monitor triggers were included together with the Tag-Int to form the Interaction trigger, INT. Some of these monitor triggers were used during normal data taking, providing a few per cent of the final trigger rate. Other monitors provided triggers for the experiment when running in non photon modes, such as setting up modes where protons were used directly on the hydrogen target. The monitor triggers were included in the interaction trigger by including a suitably reduced rate signal (where necessary) into the main INT 'OR'. All monitor triggers also went into the AUX 'OR' to signal a monitor event and not a real event. The monitor triggers were selected and controlled using a system of control levels and reduced to a suitable rate with divide-by-2^n boxes.

The relaxed tag was used to monitor the tagging system. It required two out of the three quick tag counters to fire (H4.1, H4.2, and LG) and did not include any vetos. This allowed the monitoring of the beam line without any bias that might be included by requiring a hadronic event. It also allowed the efficiency of the vetos and tagging counters to be measured. A relaxed interaction was also provided by forming the coincidence of the relaxed tag and the end-cap.

The mini tag trigger provided a trigger for non photon events by requiring a hit in the tag target counter (TTC) and a circular beam stop counter (BSC). The mini tag was used to monitor the beam line without the tagged photon requirement. It was also used to test the Channel Plate Detector installed in Region 4.

The proton beam trigger, provided a trigger for setting up the beam and Omega detectors on proton or pion beams. This trigger was formed from the coincidence of a scintillation counter in Region 2, and two similar counters in Region 3. This trigger, the so-called pion trigger, could also include the charged particle vetos, part in coincidence (S2) and part in anticoincidence (V2). It was also possible to include the end cap to form the so called 'pion interaction' trigger.

At this stage of the trigger a pulse generator was also included. It was used to help set up the electronics and also to provide a series of calibration pulses after the end of the real SPS burst (but before the read out and data acquisition end-of-burst).

2.6 - Beam Line and Tagging System Performance

The beam profiles for the three regions (Fig. 2.10) show that the beam was contained and centred in the beam line with little loss. The phase space plots for the beam in the three regions (Fig. 2.11) show the beam diverging in Z in Region 1 and weakly converging in Y. In Region 2 the beam was diverging in both planes, and in Region 3 the beam was converging to reduce the effective spot size at Omega.

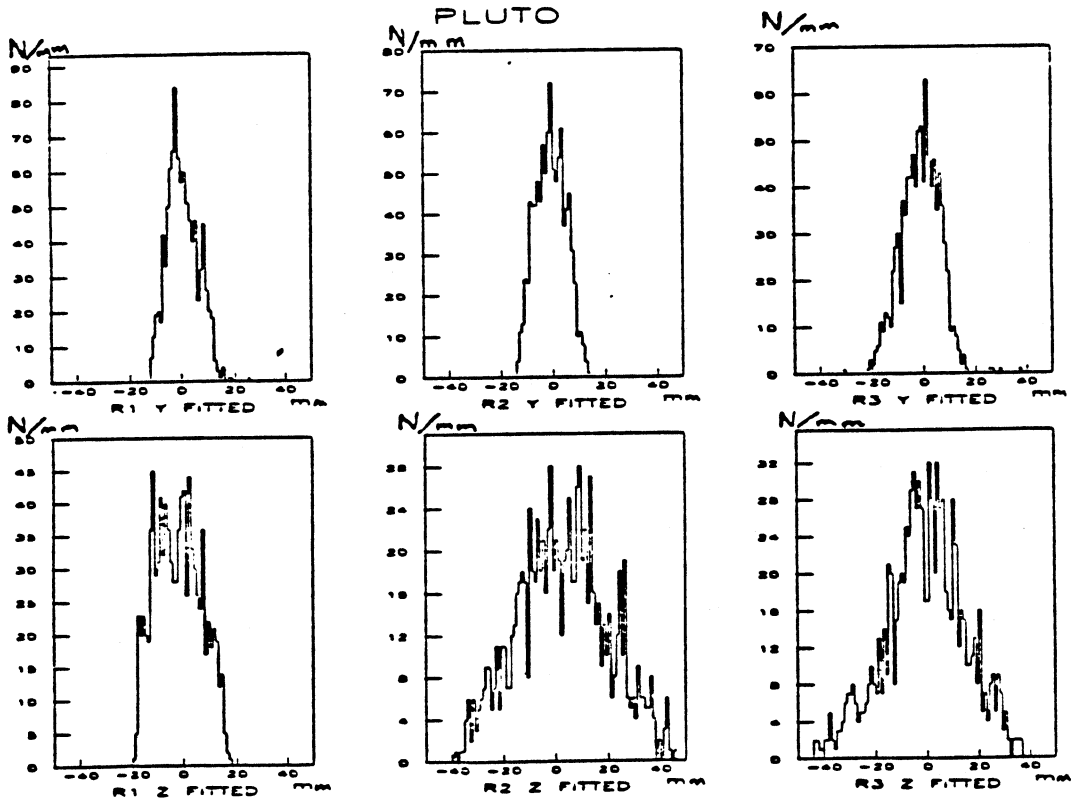

Fig. 2.10 Beam Profiles in each Region

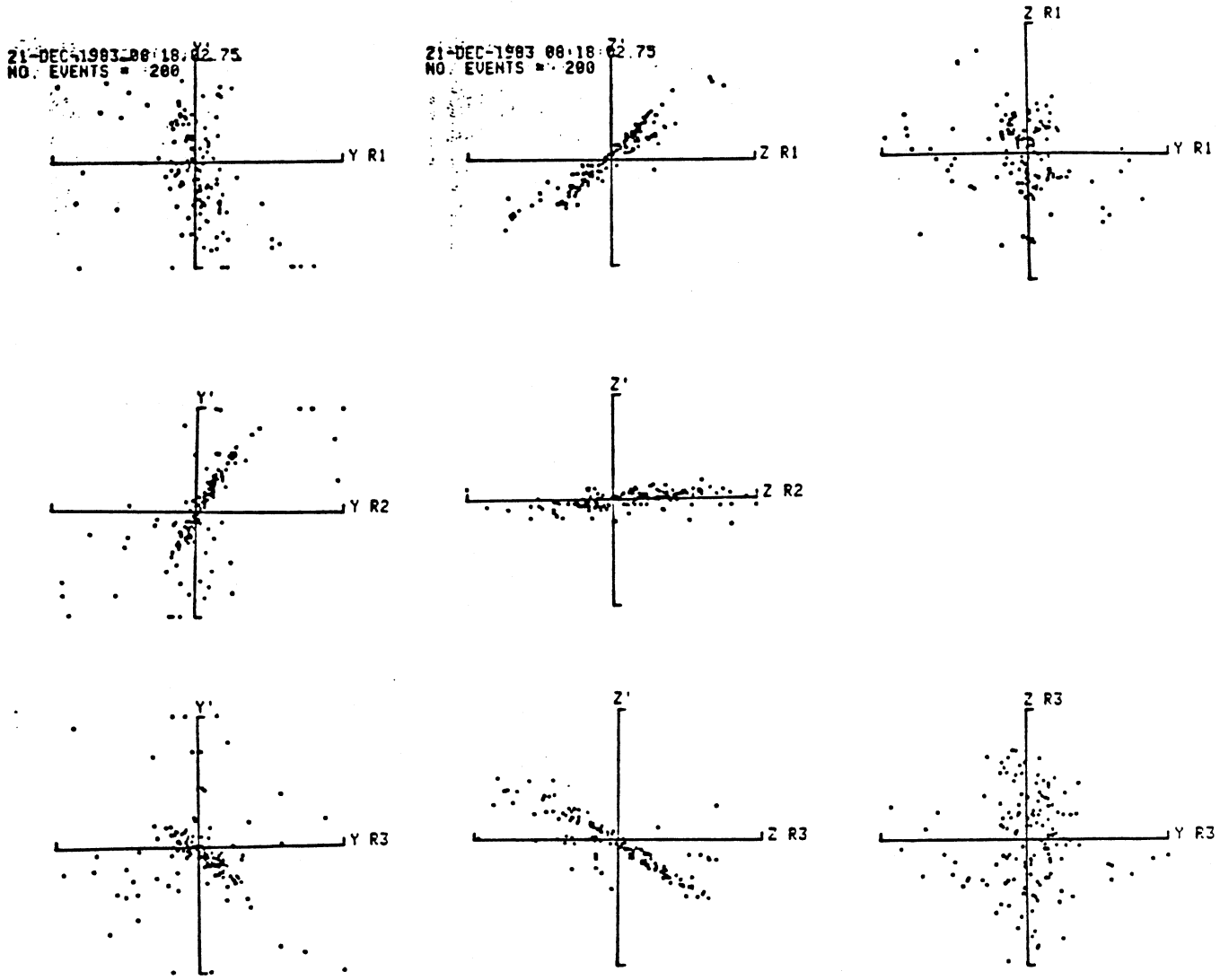

Fig. 2.11 Beam Phase Space Plots in each Region

The hit distributions in the Region 4 scintillation counter hodoscopes and lead glass (Fig. 2.12) show decreasing count rates further away from the beam line. In the H4.2 hodoscope this effect is less pronounced because the slats get larger further away from the beam line. The hit distibutions in Region 4 MWPC's also show an exponential like distribution with the maximum nearest the unscattered electron beam. This corresponds to the lower energy (and less frequent) electron being scattered the most.

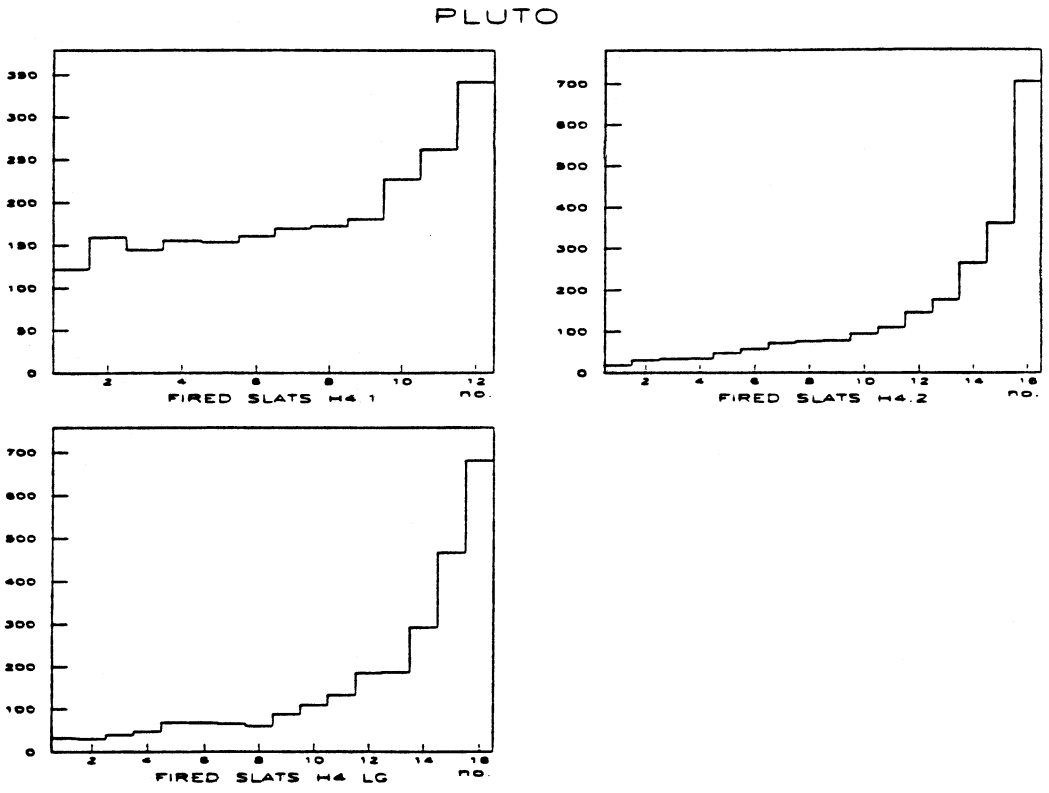

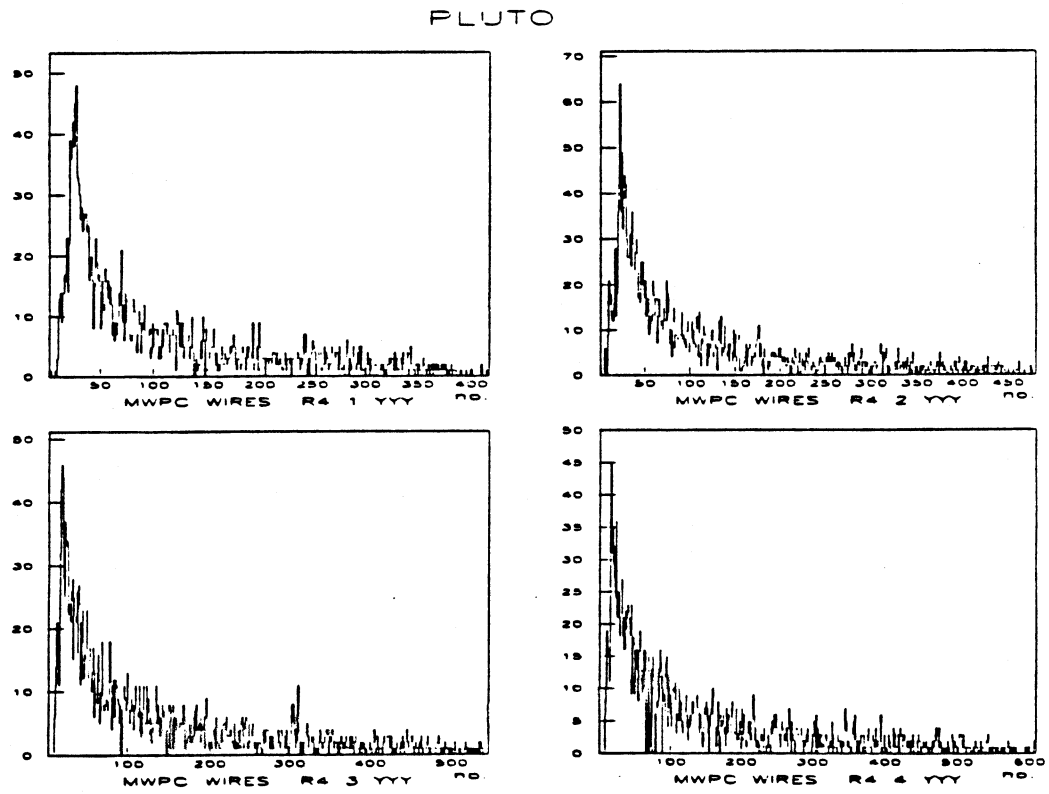

Fig. 2.12 Hit Distributions in the Region 4 Detectors

The rates in the various parts of the interaction trigger were plotted as a function of tagging target thickness and with various combinations of vetos (Fig. 2.13). These rates are shown as fractions of the count rate in the hodoscope in Region 3 and have linearly fitted line drawn on to each plot. The Tag rates plot (Fig. 2.13a) shows the Quick Tag (= Tag with no vetos) rising linearly with tagging target thickness with a zero rate intercept of about -7% of a radiation length. The addition of the tagging system vetos reduces the gradient slightly and moves the intercept down to about -4% of a radiation length. The zero rate intercept corresponds to the amount of material over and above that in the tagging target giving rise to tagged photons. The hard photon content of the Tag signal can be assessed using the coincidence rate of the Tag and Beam Veto signal (not in veto). This coincidence would fire when there was a Tag with a hard photon which did not interact in the hydrogen target. The hydrogen target was about 0·067 radiation lengths so that ideally the Tag.Beam-Veto should be about 93% of the Tag rate (assuming complete efficiency in the Beam Veto and all the non-interaction photons reaching the Beam Veto). The Tag.Beam-Veto rate (Fig. 2.13b) shows that the Tags with a good photons are not the tags killed by the veto counters. The ratio of Tag to Tag.Beam-Veto was found to be about 80%. Table 2.14 shows the rates and efficiencies of the various interaction trigger elements.

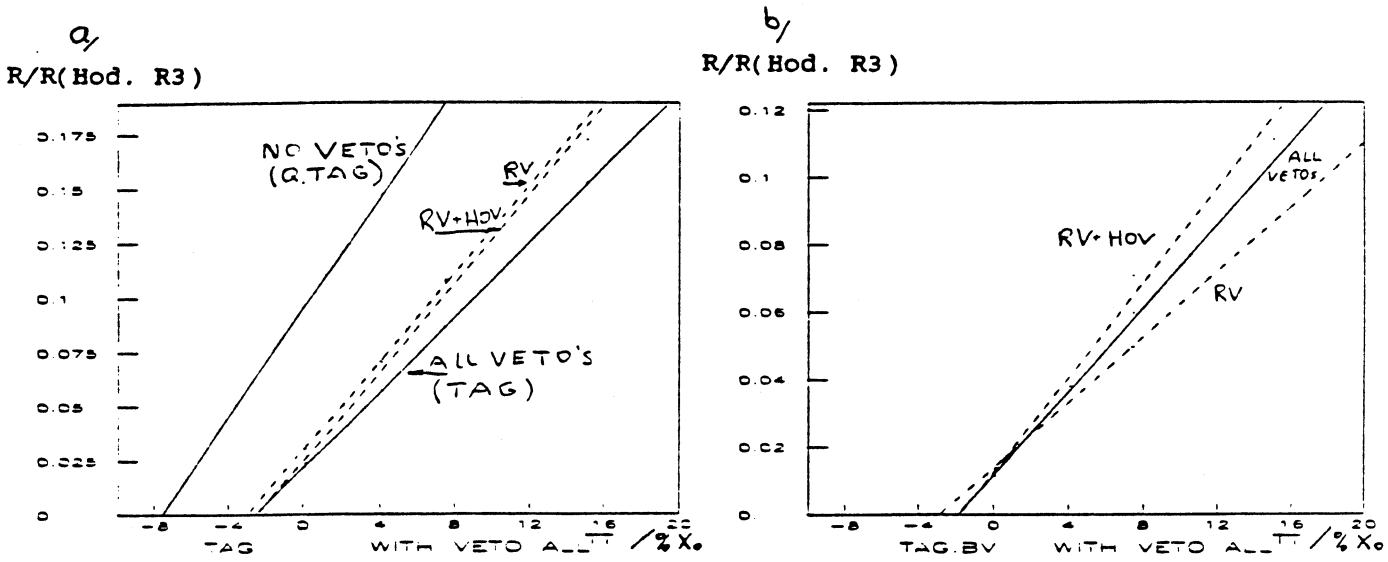

Fig. 2.13 Rates at Various Stages of the Tagging System

	Trigger Rate	Trigger Efficiency
Electron Beam (Hodo. R3)	1.31E6	0.75
Quick Tag	1.93E5	0.97
Tag	7.36E4	0.97
Interactions (Tag.EC)	8.69E3	0.95

Rates expresses as count rate per burst (out-side 'dead time')

Fig. 2.14 Rates and Efficiencies of Tagging System

2.7 - References

2-1 The West Area Beams
D. E. Plane CERN/SPS/EBP/83-22

2-2 Manual of SPS Experimental Areas Control Tree
G. Caniac and G. Dubois CERN/SPS/EBP/Note 82-7

2-3 Hagedon-Ranft Model
H. Grote, R. Hagedorn and J. Ranft CERN 1970

2-4 The 25-70 GeV Tagged Photon Facility at CERN
D. Aston et al
Nuclear Instruments and Methods 197 (1982) 287-296

2-5 A Fast and Flexible Data Acquisition System for Multiwire proportional Chambers and other Detectors
Proceedings of the Wire Chamber Conference, Vienna
NIM 156 (1978)

2.8 - Figure Captions

2.1 The Layout of the Upgraded West Hall

2.2 The West Area Wobbling Station

2.3 The H1/E1/P1 Beam Line

2.4 Parameters of the H1/E1/P1 Beam Line

2.5 Predicted H1 Beam Line Intensities

2.6 The Beam Spectrometer

2.7 The Layout of the Beam Profile Detectors in each Region

2.8 The Layout of the Tagging System

2.9 The Interaction Trigger

2.10 Beam Profiles in each Region

2.11 Beam Phase Space Plots in each Region

2.12 Hit Distributions in the Region 4 Detectors

2.13 Rates at Various Stages of the Tagging System

2.14 Rates and Efficiencies of Tagging System

CHAPTER III

THE CHANNEL PLATE DETECTOR

Chapter III

3 - CHANNEL PLATE DETECTOR

3.1 - Introduction

The Channel Plate Detector (Ref. 3-1) was conceived a alternative to the beam MWPC's. It was designed to have a time resolution as good as the scintillation counter hodoscopes together with a spatial resolution as good as or better than the MWPC's in use in the beam line. The detector had also to work at beam rates above 10^7 s^{-1} without saturation or loss of efficiency. Since the detector was for use in the electron beam line it had to have a minimum amount of material in the beam. This was of particular importance in the electron beam used in this experiment because of bremsstrahlung emission. Low energy bremsstrahlung photons radiated in a beam detector would add to the beam halo and hence cause backgrounds in both the beam line and Omega detectors. More importantly, the remaining electrons in the beam would have a reduced energy, hence be wrongly measured by the beam spectrometer and so reduce the energy resolution of the beam.

MWPC's used in high rate beam lines suffer from limitations in the following ways. The practical wire spacing limit of 1 mm imposes a limit on the spatial resolution ($\sigma=d/\sqrt{12}$) and to a certain extent on the time resolution ($\approx$ 25 ns). The time resolution is determined by two factors, the time taken for the charge to drift on to the wire and the avalanche process at the wires giving rise to the gas amplification. Decreasing the wire spacing would improve the spatial and time resolution of the chamber at the

expense of increasing the amount of material in the beam and introducing serious mechanical problems in construction of such chambers. Another problem is caused by the high rate and high gas gain in the chambers. This can cause deposits to form on the wires leading to ageing in the chamber and the loss of efficiency. It may also cause the growth of whiskers on the wires and possible sparking leading to broken wires. These problems can be alleviated by expanding the beam at the chamber to reduce the beam flux density, and reducing the gas gain at the expense of increasing the gain in the chamber electronics and causing noise pickup problems.

The channel plate detector avoids these problems by having a thin secondary emitting cathode in the beam. The secondary electrons created by the beam particles passing through the cathode were extracted from the beam and focussed on to the face of a pair of channel plate multipliers using an electrostatic lens. The channel plates provided electron amplification ($\approx 10^6$) together with the preservation of spatial resolution. The charge pulse from the back surface of the channel plates was then collected on two planes of orthogonal wires, similar to a fine grain MWPC. The detector was enclosed in a vacuum vessel with a pressure typically 10^{-6} torr. This system provided good spatial resolution by the use of fine grain multi-wire read-out arrays and the ability to use the lens to magnify the image on the cathode. The time resolution was very good because the secondary electrons travel quickly over a fixed distance in the lens at 10 KV, and because of the channel plate multiplier's fast transit time ($<$ 100 ps). In addition, the operation of the amplification process in the channel plate multipliers, rather than in a gas chamber avoids some of the problems of a MWPC.

Chapter III

In the Eγ experiment WA69 it was proposed to have one channel plate detector in the beam line in Region 3 (Fig. 3.1), and one in Region 4 (Fig. 3.2, the tagging region), in the unscattered electron beam in front of the electron beam dump. The channel plate detector in Region 3 was initially for test purposes, where the beam spectrometer could be used to predict the position of hits in the detector for comparison with the hits seen in the detector. This information could then be used to find the efficiency of the detector, the spatial resolution and any distortions in the electrostatic lens. Eventually, this channel plate detector is to be incorporated into the beam line reconstruction. The channel plate detector in Region 4 was to be used to reconstruct the trajectory of electrons that radiate little, if any, energy in the tagging target. Comparison of these electron trajectories and the corresponding beam track could then be used to measure the beam loss so help to calibrate the Radiation Veto (where the energy lost between Regions 2 and 3 is detected) and to extend the range over which photons can be tagged.

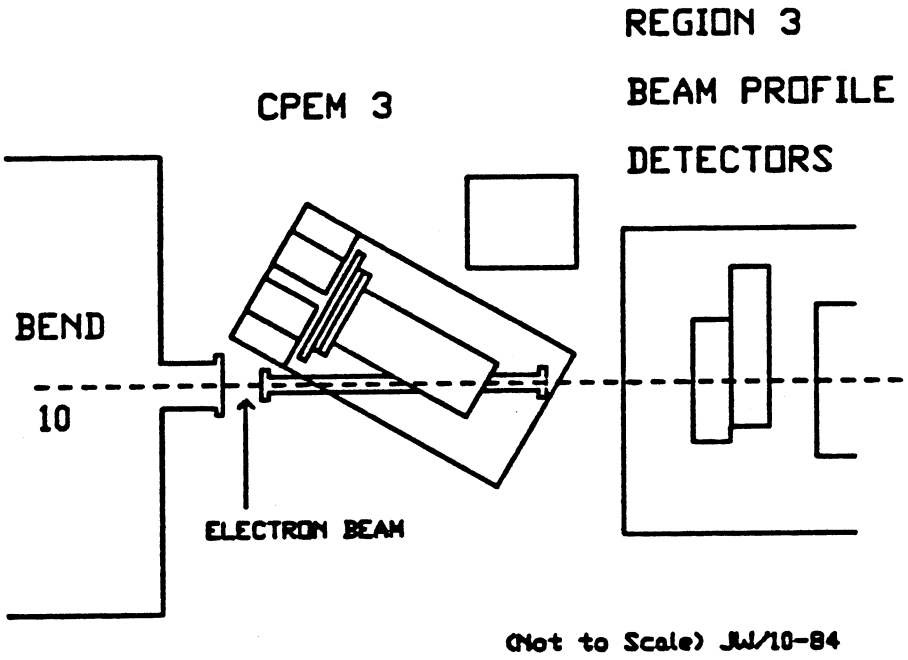

Fig. 3.1 Channel Plate Detector in Region 3

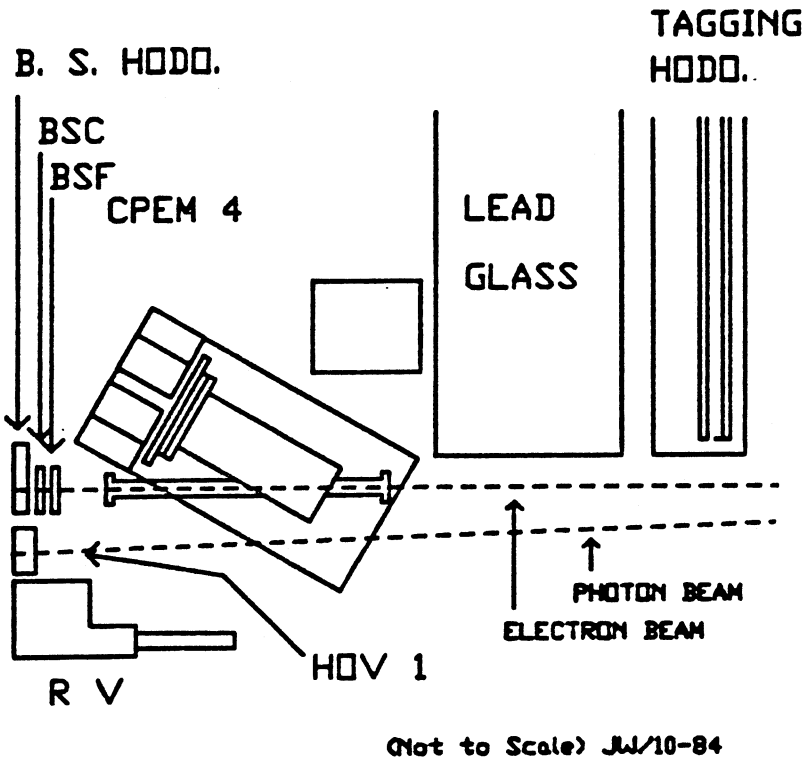

Fig. 3.2 Channel Plate Detector in Region 4

3.2 - The Detector Design

The secondary emission detector (Fig. 3.3) consisted of a thin secondary cathode at an angle of 30° to the beam line, where each beam particle as it passes through the cathode emitted a few secondary electrons. The secondary electrons were removed from the beam line and focussed on to a pair of channel plate multipliers (CPM) by an electrostatic lens. Inside the channel plates the few electrons were amplified into an electron shower of about 3×10^6 electrons. This shower was picked up by a two dimensional array of fine wires in the back-plane. A few wires in each array collected the charge from the channel plates and passed it to the read-out electronics. Thus, assuming 100% efficiency, for each beam particle passing through the detector the read-out electronics provided digitizings corresponding to the point the particle passed through the cathode. For the early testing delay lines were used to read-out the detector. However, for the high rates in beam line tests and in the final configuration the full Multi-Wire Proportional Chamber type read-out was used.

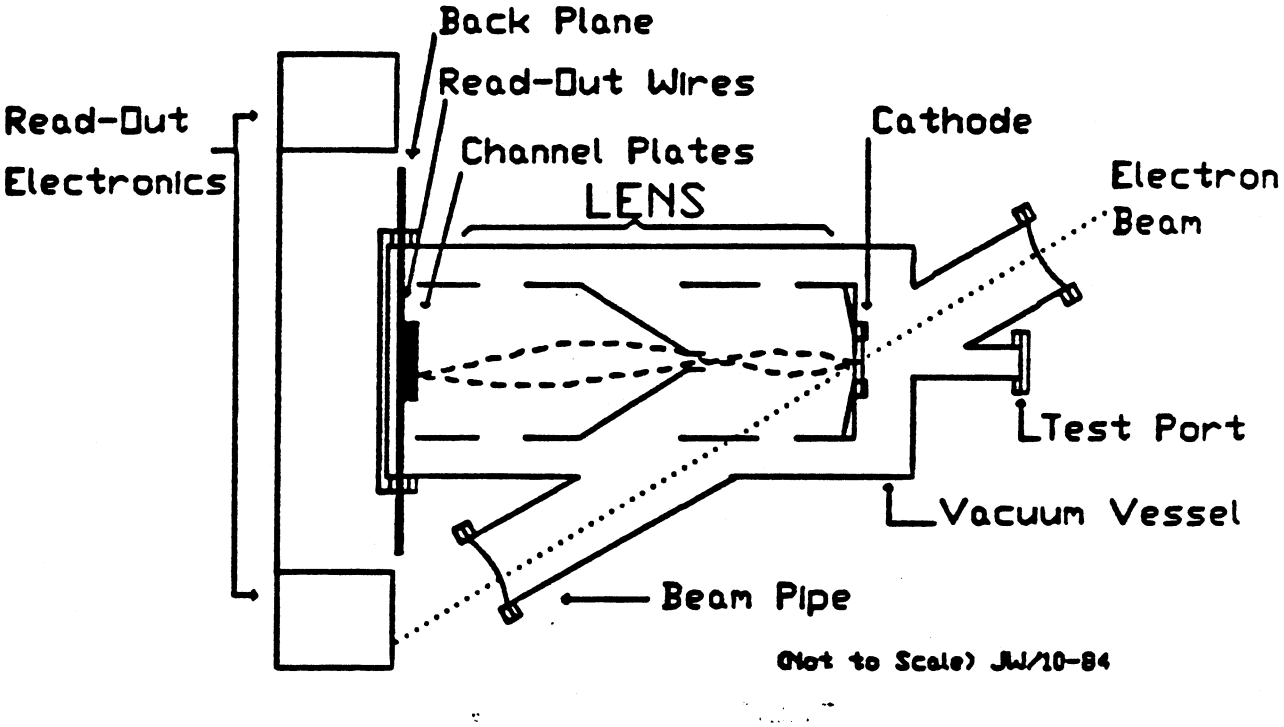

Fig. 3.3 The Channel Plate Detector

A low density Caesuim Iodide (CsI) layer between 100 μm and 300 μm thick was used as a secondary emitting cathode. In this layer the beam particles ionized the CsI producing secondary electrons (Ref. 3.2). A large electrostatic field across the layer ($\approx$ 20 KV cm^{-1}) was used to extract the secondary electrons and provide some amplification. Electron amplification takes place in the cathode because the secondary electrons are accelerated by the field across the holes in the foam and attain sufficient energy to create further ionization (Ref. 3-3). Hence, it was important that the CsI

layer was thin and of low density so that the secondary electrons could easily be extracted and amplification take place. In order to ensure a high overall efficiency the mean number of secondary electrons produced by the initial ionization had to be ≈ 6. The amplification factor (≈ 10×) then had to ensure sufficient electrons were produced to get out of the cathode to the channel plates. It was also important to have only a small amount of material in the cathode to prevent degradation of the beam. It was estimated that the detector had the equivalent of 0·2% of a radiation length in the beam. The low density CsI layer was formed by evaporation of dry CsI on to a cooled titanium foil in an atmosphere of argon at 5 torr. Once these cathodes were made they had to be kept under vacuum or in dry inert atmosphere because of the hygroscopic nature of CsI. The extraction field was provided by putting a potential between the titanium foil supporting the CsI layer and a nickel micro-mesh stretched across a pyropholyte ring above the layer (Fig. 3.4). The rest of the cathode assembly acted as a support for the cathode itself and provided electrical connections to the foil and micro-mesh. For the early tests a 300 μm layer was used with the micro-mesh supported 0·5 mm away from the titanium foil but for the beam line tests a 200 μm layer with a foil micro-mesh separation of 1 mm was found to be better.

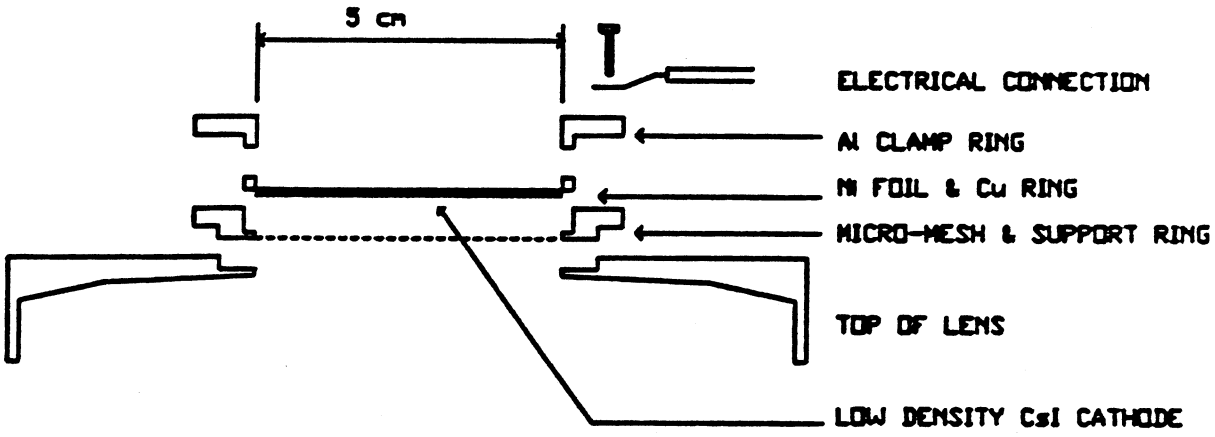

Fig. 3.4 The Secondary Emission Cathode

The lens (Fig. 3.5) consisted of a four element axially symmetrical electrostatic zoom lens. The lens was designed by scaling up (Ref. 3-4) existing image intensifier lenses (Ref. 3-5). Similar lens designs have also been used on different scales in position sensitive photo-multiplier tubes (Ref. 3-6). The lens provided point to point focusing between the cathode and the CPM with magnification between 0·5× and 2×. The voltages for the lens elements and the cathode were provided by tappings of a resistor chain powered by a variable high voltage supply.

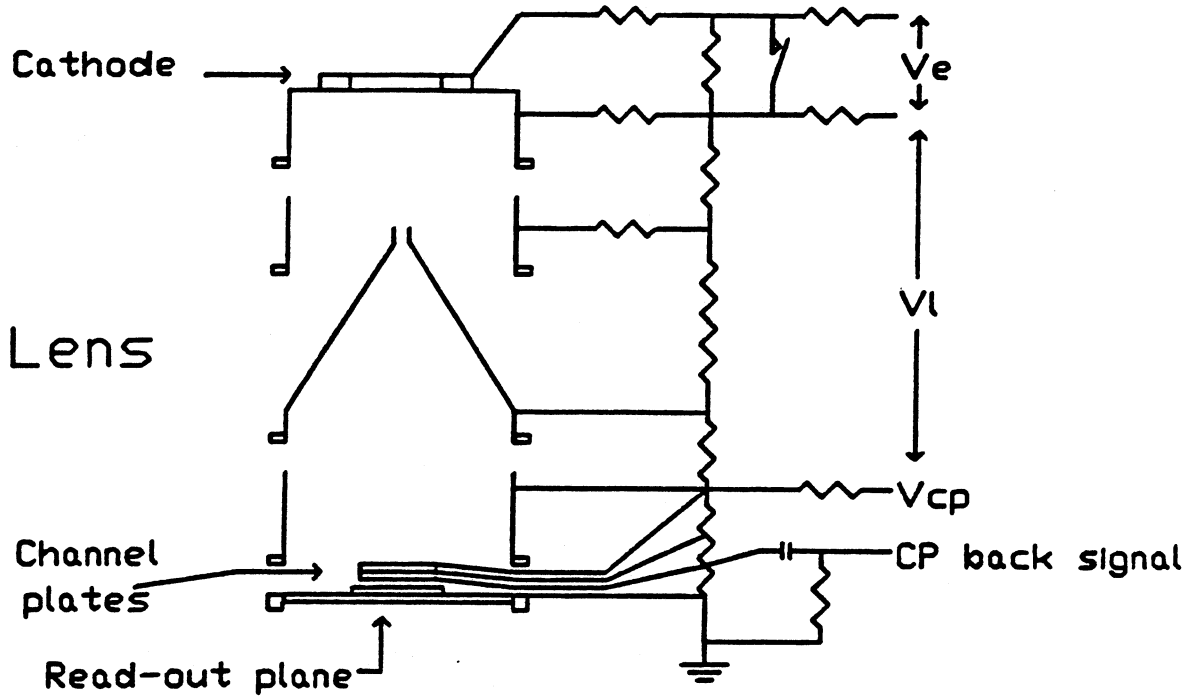

Fig. 3.5 The Lens Assembly

A tandem channel plate multiplier assembly (Mullard G25-70's) was used to provide point-wise amplification for the electrons from the cathode. Channel plates are wafers of lead glass about 1 mm thick with an array of many tiny ($\approx$ 25 μm) holes through them (Fig. 3.6). A thin film of nickel is evaporated over the surfaces of the plates across which a voltage is applied. When electrons enters the holes they are accelerated by the electrostatic field across the plate. When the electrons hit the walls of the holes more secondary electrons are produced by secondary emission and accelerated down the

hole, hence amplifying the signal. In this way each hole can be considered as a 'continuous dynode' photo-multiplier tube (Ref. 3-7). The electron showers from the back of the channel plates was collected on wire arrays connected to the read-out electronics. In the detector the channel plates were run at about 1·3 KV each, providing a gain of $\approx 10^3$ per plate. The channel plates were mounted in close proximity to each other and the back-plane with a voltage of about 100 V across the gaps ($\approx$ 0·5 mm) to ensure proximity focusing beween them. The channel plates output about 0·5 pC ($\approx 3\times10^6$ electrons) to the back-plane to trigger the read-out electronics.

The location of the showers in the channel plates was detected using two perpendicular arrays of 285 wires at 250 μm spacing mounted in the back-plane. One of the two arrays was formed as tracks on a printed circuit board (PCB) and the other a grid of 80 μm stainless steel wires held above the PCB plane on notched spacers. Electrical connections to the wire array was via a second set of connections on the PCB. The back-plane PCB was sandwiched between two stainless steel vacuum flanges and sealed with vacuum ceramics. The tracks on the PCB came out through the ceramic seal to arrays of sockets for connection to the read-out electronics. E. Kellogg et al (Ref. 3-8) has shown that it is possible to obtain equal charge sharing between perpendicular wire planes by biasing the wires by a few volts (Fig. 3.7) but this biasing will have to be determined experimentally.

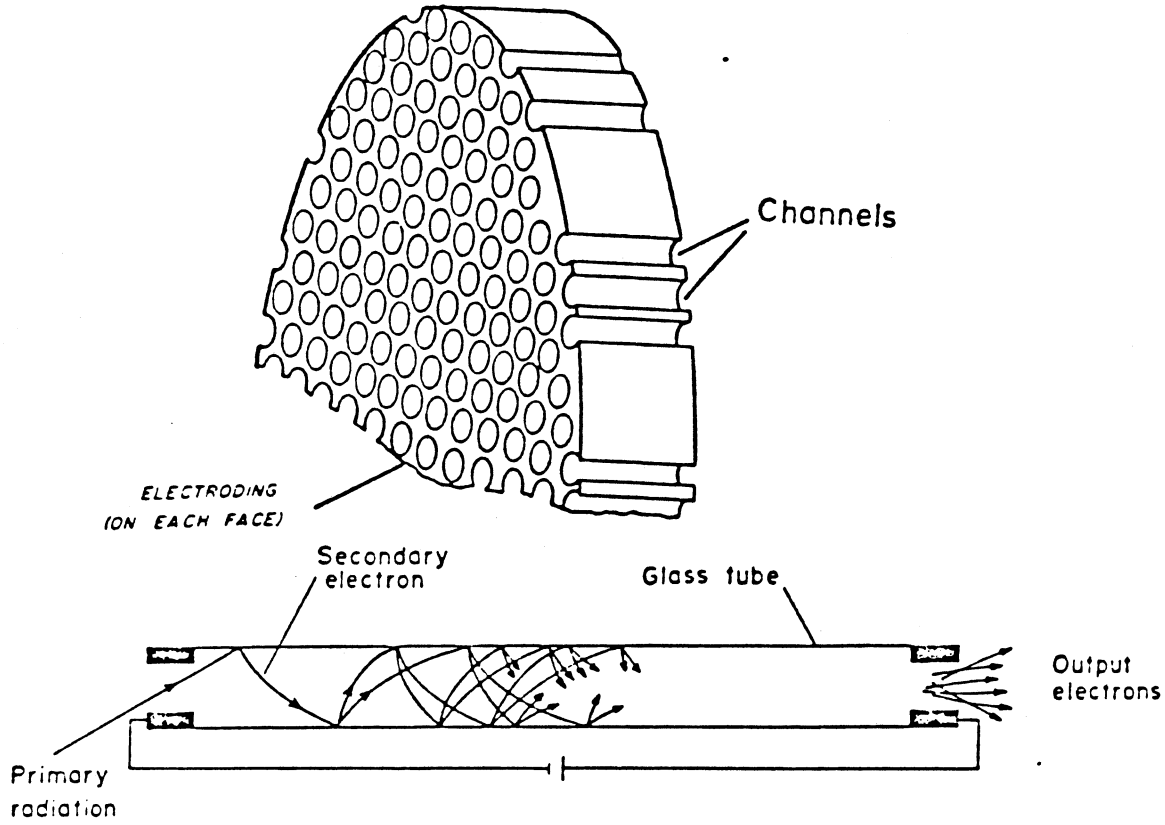

Fig. 3.6 Diagram showing Channel Plates

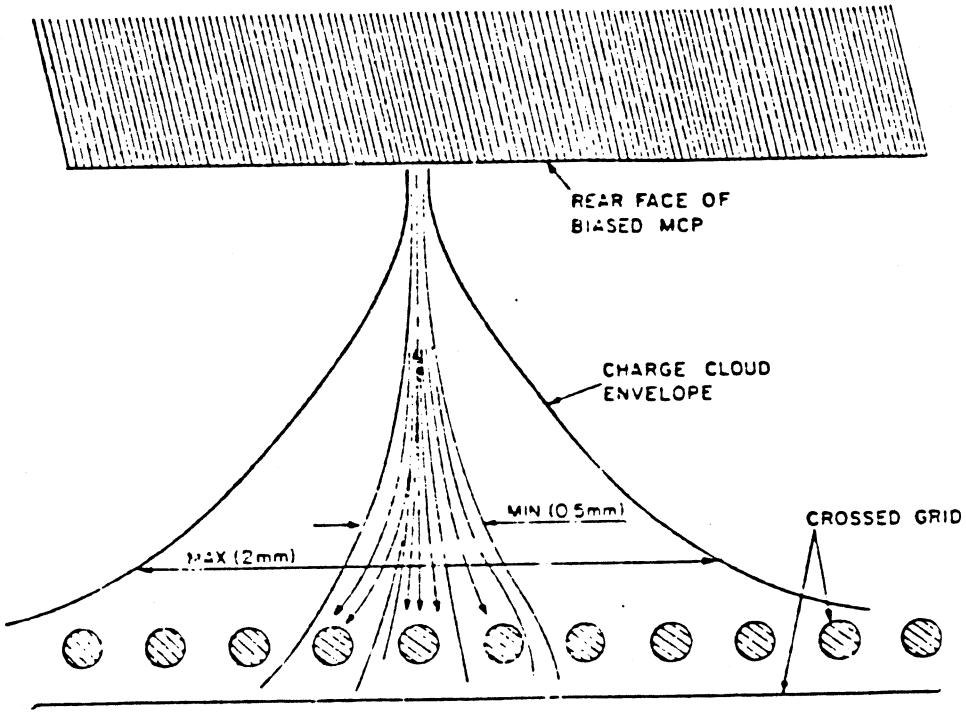

Fig. 3.7 Charge Sharing on the Read Out Wires

The whole detector was enclosed in a large high vacuum stainless steel vessel. This consisted of a 220 mm diameter tube housing the lens, with the back-plane flange at one end. At the other end the lens tube intersected the beam pipe (100 mm Dia.) at an angle of 30° so that the cathode lay in the beam. There were also subsiduary pipes and flanges for the test port, the vacuum pump connections and pressure gauges. The lens and CPM were initially mounted on the back-plane flange so that the whole detector assembly could be removed with the back-plane flange. The electrical connections to the cathode, lens and CPM were connected to feed through insulators on the back-plane flange behind the wire arrays and the PCB. This arrangement was changed due to electrical breakdown problems on the feed through insulators in the back flange and the difficulty of removing the back-plane and lens assembly. In the final arrangement the lens was separated from the back-plane and supported directly in the main part of the vessel. The electrical connections used high voltage vacuum feed through insulators mounted in a port underneath the detector. The vacuum system used a turbo-molecular pump (Leybold-Heraeus: Turbovac) to maintain a pressure of about 10^{-6} torr in the detector, and a rotary backing pump. The vacuum pressure was monitored with a VG Ion Gauge and a VG ANAVAC2 (vacuum mass spectrometer). The backing pressure was monitored with an Edwards Pirani Gauge.

For the early tests of the detector with radioactive sources delay lines and constant fraction discrimiators (Ref. 3.9) were used to read-out the detector. For both planes in the detector, each wire was connected to parallel strips on a printed circuit board. Upon

these printed circuit boards delay lines were clamped providing capacitive coupling between the read-out wires and the delay lines. The position of the charge shower was determined by the difference in the arrival time of the induced pulses at the ends of the delay lines. A typical delay time of 300 ns limited the maximum rate at which the detector could work to about 10^6 s^{-1} (not including data conversion and computer dead times). This was adequate for source tests. For the beam line tests the full read-out electronics was used. This consisted of modified existing beam MWPC electronics consisting of amplifiers, discriminators and MECL line drivers (Kake amps) for each wire (Ref. 3-10). These amplifiers had a low threshold of $\approx$ 5 fC and had been modified to allow the biasing of the readout wires. This was followed by the usual MWPC read-out system of twisted pair cables, rate gates and the CERN RMH system. This read-out system limited the maximum rate to about 5×10^7 s^{-1} (under the same assumptions as before). This was an electronics limitation not an intrinsic detector limitation. The detector also provided a very fast signal from the back face of the channel plate (<1 ns wide), which corresponded to an inverted 'OR' of the signal on the read-out wires. With suitable fast electronics this could be used as a fast trigger giving a strobe for each particle passing through the detector.

3.3 - Results

The channel plate detector was initially tested using radio active sources at the Rutherford Appleton Laboratory and at Manchester University. These tests were used to assess the imaging properties of the detector and learn about the secondary emission process. The detector was then taken to CERN and put in a test beam to assess the performance of the detector in a particle beam and find its operating conditions and overall efficiency. It is hoped to be able to repeat the efficiency tests and investigate the imaging properties of the detector in the WA69 electron beam line ready for use in the main WA69 experiment data taking.

3.3.1 - Source Test Results

The early tests of the Channel Plate Detector used a source and a shadow mask to illuminate the cathode from the test port, together with the delay line read-out. Using an Fe^{55} source and a mask containing a line of holes a time difference distribution (Fig. 3.8) was obtained. The mask consisted of a line of 7 holes 5 mm apart, with the holes increasing in diameter towards the edge in equal steps of diameter from 0·2 mm to 0·8 mm. The time difference distribution shows 7 equally spaced peaks. The smallest peak in the centre is due to the hole in the centre of the mask. The small peak at the right hand side is due to a mask hole but because of acceptance effects has a reduced area. Using this distribution and other similar distributions the resolution was estimated to be better than 250 μm.

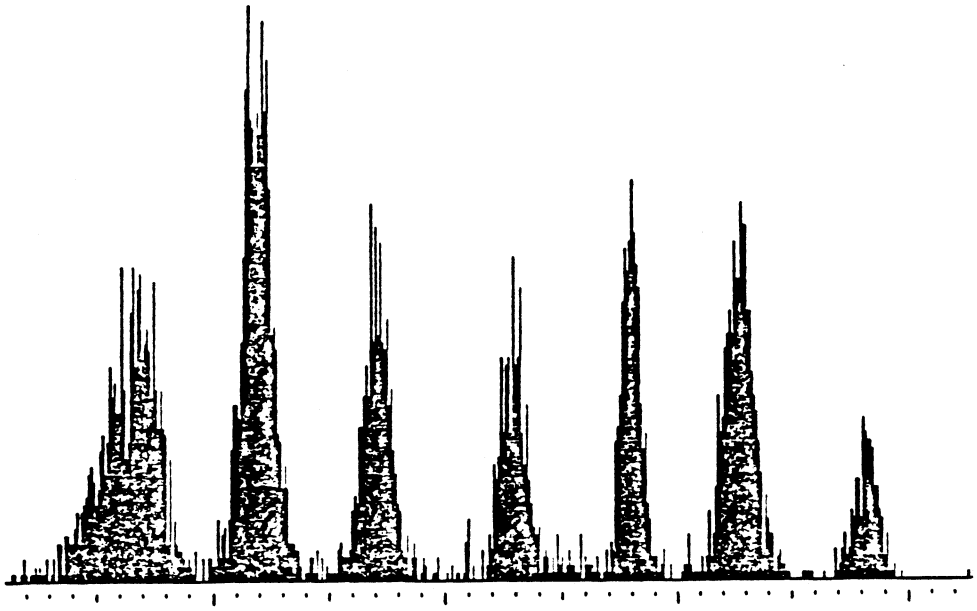

Fig. 3.8 Delay Line Output

In order to find the operating conditions for maximum efficiency the count rate from the delay lines (for events with a pulse at both ends of the delay lines) was plotted against the channel plate voltage, V_{cp} and extraction voltage, V_e. For this test the Fe^{55} source illuminated the cathode from the down-stream beam pipe rather than from the test port. This was because it was found that the 5·9 KeV photons from the Fe^{55} source did not penetrate very far through the low density CsI layer and it was suspected that electrons were only being extracted from a surface layer of the cathode. In this configuration the graphs of count rate

against V_e and V_{cp} (Fig. 3.9) did not show any signs of plateaus. It was found that due to coupling losses to the delay lines the 'effective threshold' presented to the read-out wires was high and so the read-out system was very inefficient.

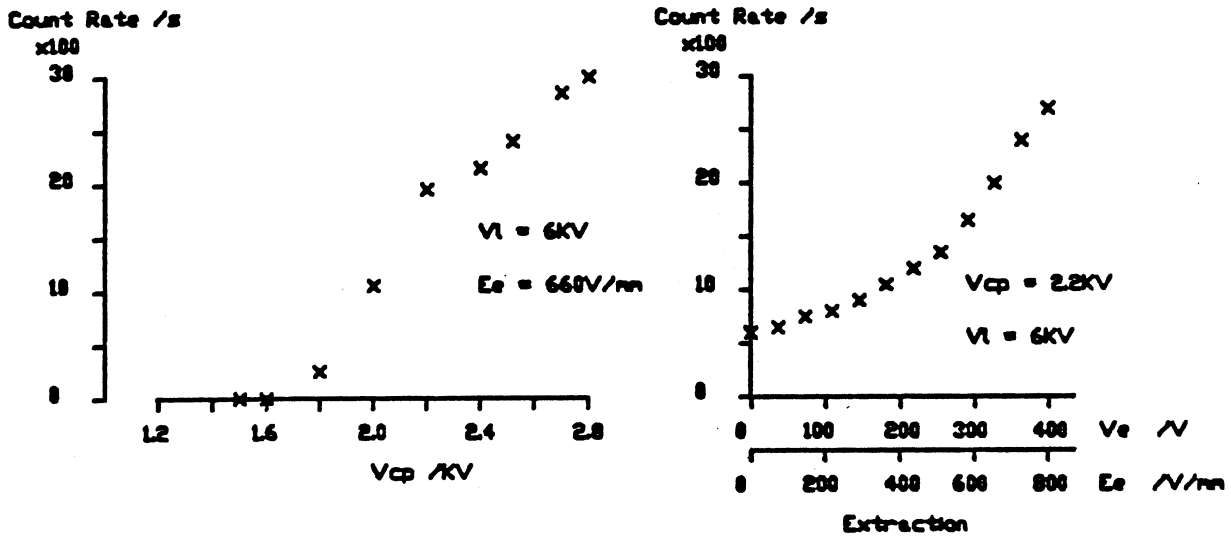

Fig. 3.9 Rate against extraction and Channel Plate Voltage

3.3.2 - Test Beam Results

The channel plate detector was installed in an East Hall Test Beam (C13) at CERN in the summer of 1982 for its beam line tests. The beam tests were carried out in conjunction with the early beam tests for the Ring Image Čerenkov detector used in the WA69 experiment (see Section 4.3). Five scintillation counters were set up in the beam line to provide triggering on beam particles; two large counters and one small counter were installed at the front of our beam area, and one large and one small counter at the back. Coincidences between the three large counters were used as a general beam trigger and the coincidence of all five counters used to provide a trigger for a pencil beam of approximately 1 cm diameter. An array of four MWPC was also installed at each end of the beam area to enable reconstruction of the trajectory of the beam particles. A PDP 11/34 together with a small CAMAC system was used for data acquisition. The PDP 11/34 also enabled on-line monitoring of aspects of the test experiments and the writing of events to the MSS in the CERN computer centre via a CERNET link.

Using the pencil beam trigger as a strobe it was possible to detect positive going pulses from the back of the channel plates. This signal was inverted using a transformer and amplified, then split to drive both a CAMAC ADC (analogue to digital converter) and a discriminator. The ADC was strobed with a dead time gated beam trigger signal and read into the PDP 11 with every event. This provided two methods of measuring the efficiency of the detector, the first using the direct coincidence between the discriminator on the

channel plate back face signal and the beam trigger, and the second using the charge spectrum from the ADC. Using the direct coincidence logic the efficiency was defined as the ratio of the number of channel plate back signals in coincidence with beam triggers to the number of beam triggers. Using the charge spectrum it was defined as the ratio of the number of events with charge above a threshold to number of events recorded. For this the charge threshold was set just above the noise on the ADC pedestal. Similar results were obtained by both methods.

Figure 3.10 shows the efficiency plotted against discriminator threshold and the ADC charge spectrum with fixed channel plate, lens and extraction voltages. The discriminator threshold was set to a value just above the noise. This value, in terms of charge leaving the channel plates was about 50 fC per event ($\approx 3\times10^5$ electrons emitted from the channel plates) which is about the same as the threshold chosen on the charge spectrum to separate the noise on the pedestal from the true signal. Using the ADC charge spectrum the efficiency was measured as a function of channel plate voltage, lens voltage and extraction electric field (extraction voltage). The efficiency against channel plate voltage (Fig. 3.11a) shows the efficiency rising above 1·8 KV in a similar way as in the source tests, then flattening out above 2·3 KV to a plateau at about 30% efficiency. Against lens voltage (Fig. 3.11b) the efficiency rises then plateaus out at about 9 KV. The efficiency against extraction voltage (Fig. 3.11c) shows the efficiency rising at first, then flattening out before rising again to reach a plateau at about 30% with an extraction voltage of 1·6 KV (an extraction field of 1·6 KV cm^{-1}).

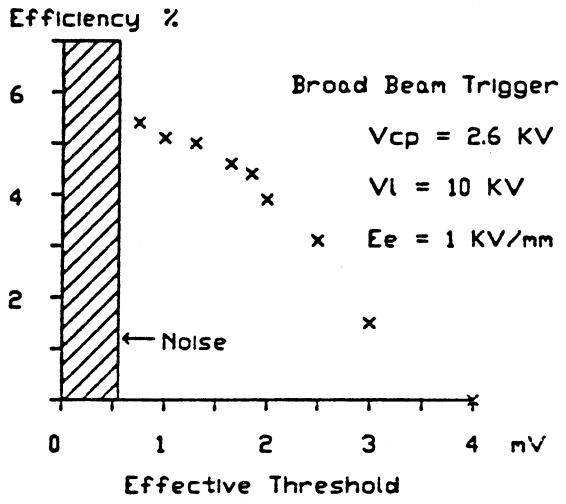

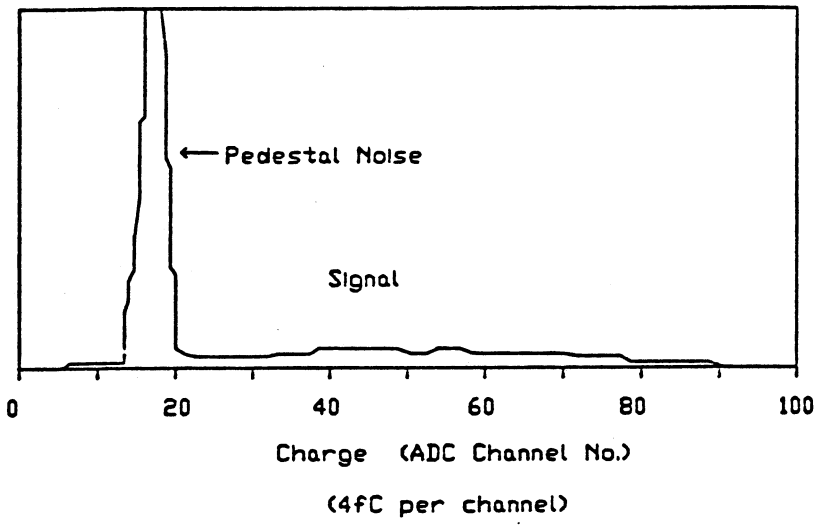

Fig. 3.10 CPM Back Signal Charge and threshold Distributions

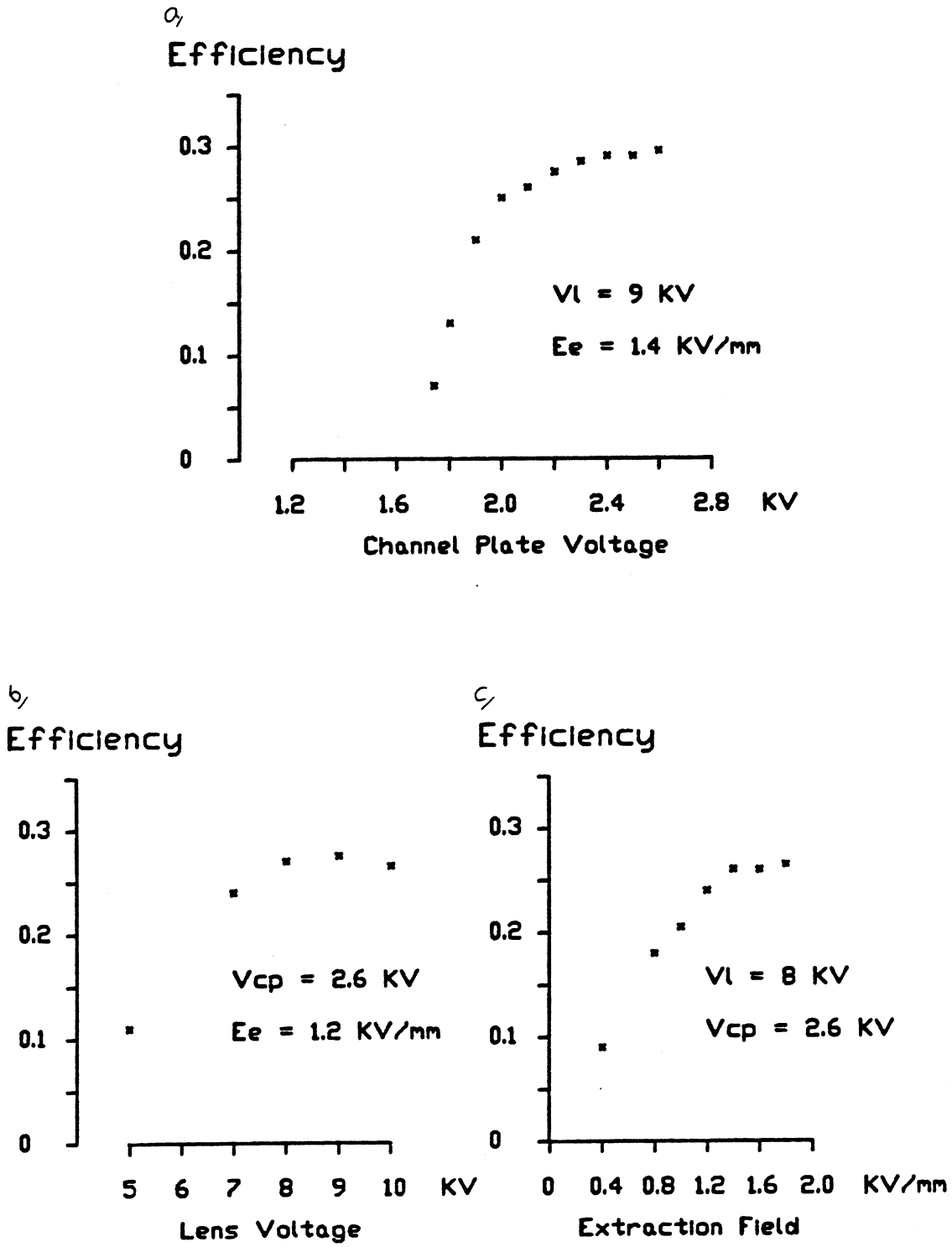

Fig. 3.11 Channel Plate Detector Efficiency

The measurements of efficiency presented above were taken some time (≈ 10 m) after the conditions were set up to allow the count rates to stabilize. It was found that after the extraction voltage was changed the efficiency varied rapidly. When the extraction voltage was increased the efficiency was initially higher than expected and then dropped to an equilibrium level. When the extraction voltage was decreased the efficiency dropped and then increased to an equilibrium level. In order to investigate this time dependence and hysteresis effect the extraction voltage was switched from zero to 20 KV cm^{-1} with the channel plate voltage and lens voltage set to 2·7 KV and 10 KV respectively. The efficiency was then measured as a function of time after 'switch on' (Fig. 3.12). Initially the efficiency was found to be ≈ 90%, it then started to fall, rapidly at first, before reach an almost constant value of ≈ 25% after about 10 m. Similar effects have also been seen in other detectors using dielectric secondary emission cathodes (Ref. 3-11).

The efficiency measurements against channel plate voltage and extraction voltage were then repeated with the extraction voltage switched off (with a high voltage read relay) between beam bursts on during the beam spill. The extraction voltage was off for 6 s before the start of burst then on during the 1 s spill and a further 3 s after (The PS provided a 1 s spill every 10 s). The efficiency curves obtained with the pulsed extraction voltage (Fig. 3.13) show the same features as those obtained without the pulsed extraction voltage with the plateaus at ≈ 95% efficiency. Figure 3.14 shows the development of the charge spectrum from the back of the channel plates with

increasing channel plate voltage and extraction voltage. As the channel plate voltage is increased the signal in the charge spectrum was seen to move out of the pedestal as the gain of the channel plate increases. With increasing extraction voltage the signal increases as the chance of extracting any electrons increases. Then as the extraction voltage is further increased the over all gain of the detector increases as the chance of getting more than one electron extracted increases without much increase in efficiency.

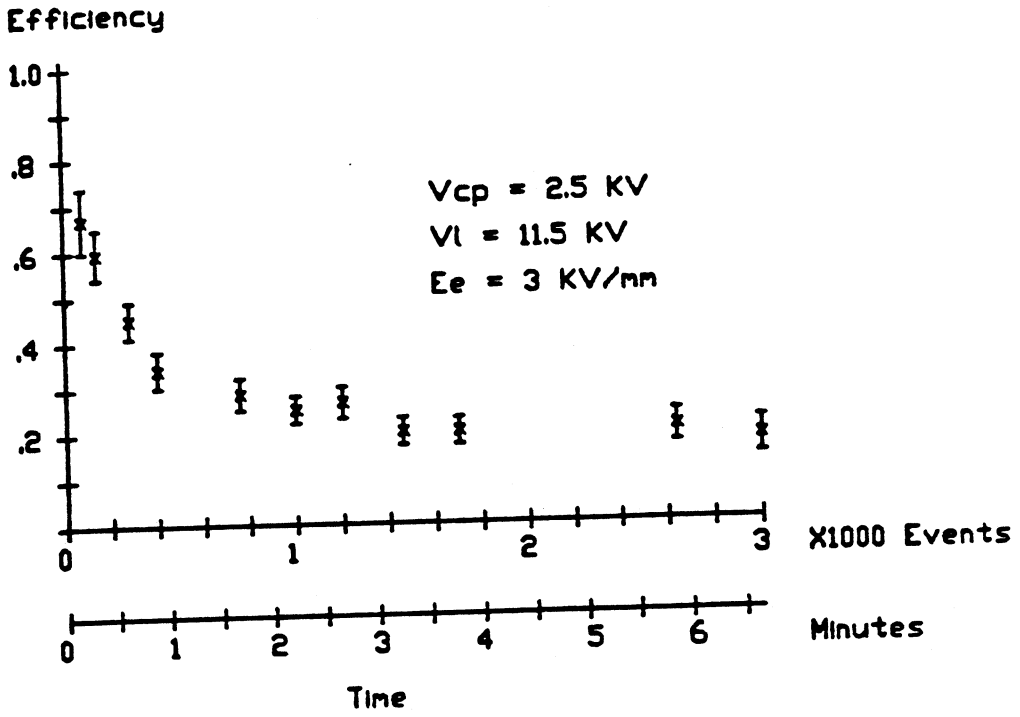

Fig. 3.12 Channel Plate Efficiency as a Function of Time

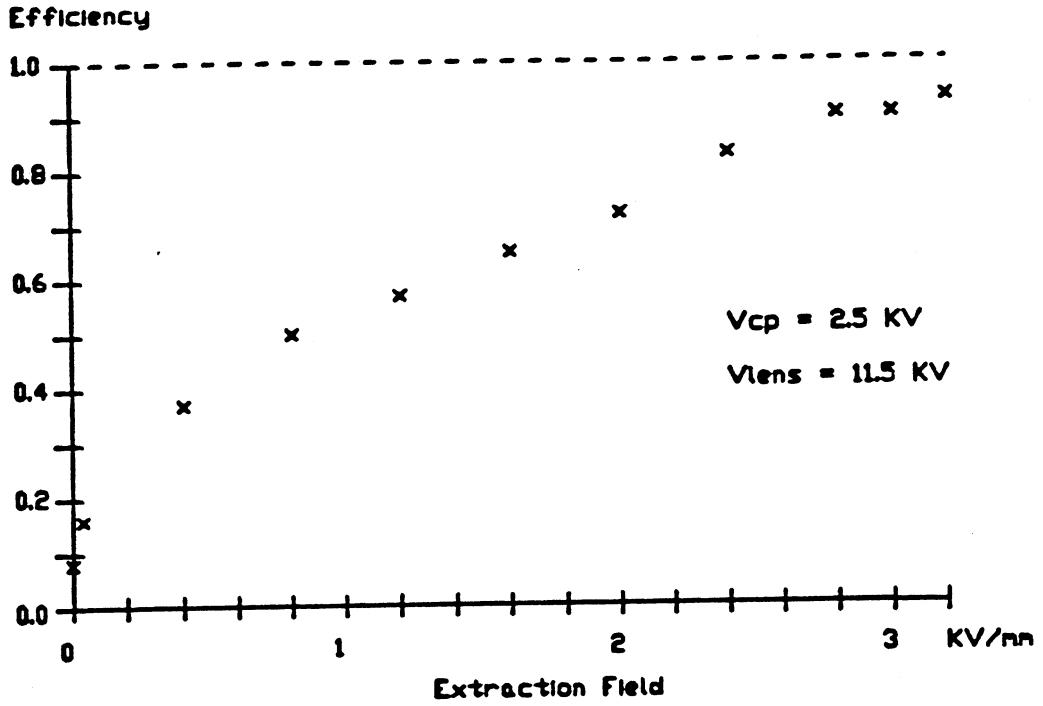

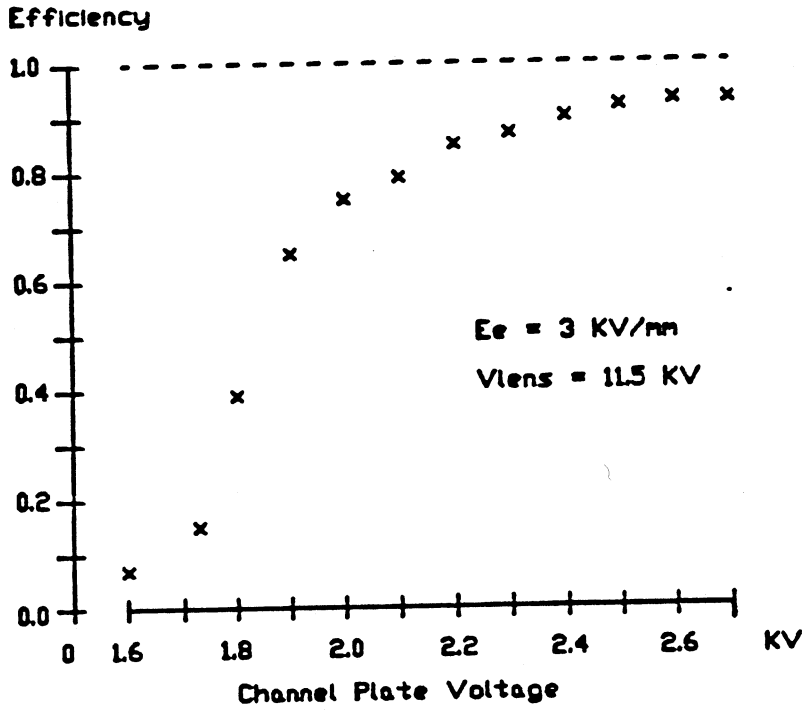

Fig. 3.13 Channel Plate Efficiency Curves With Pulsed Extraction

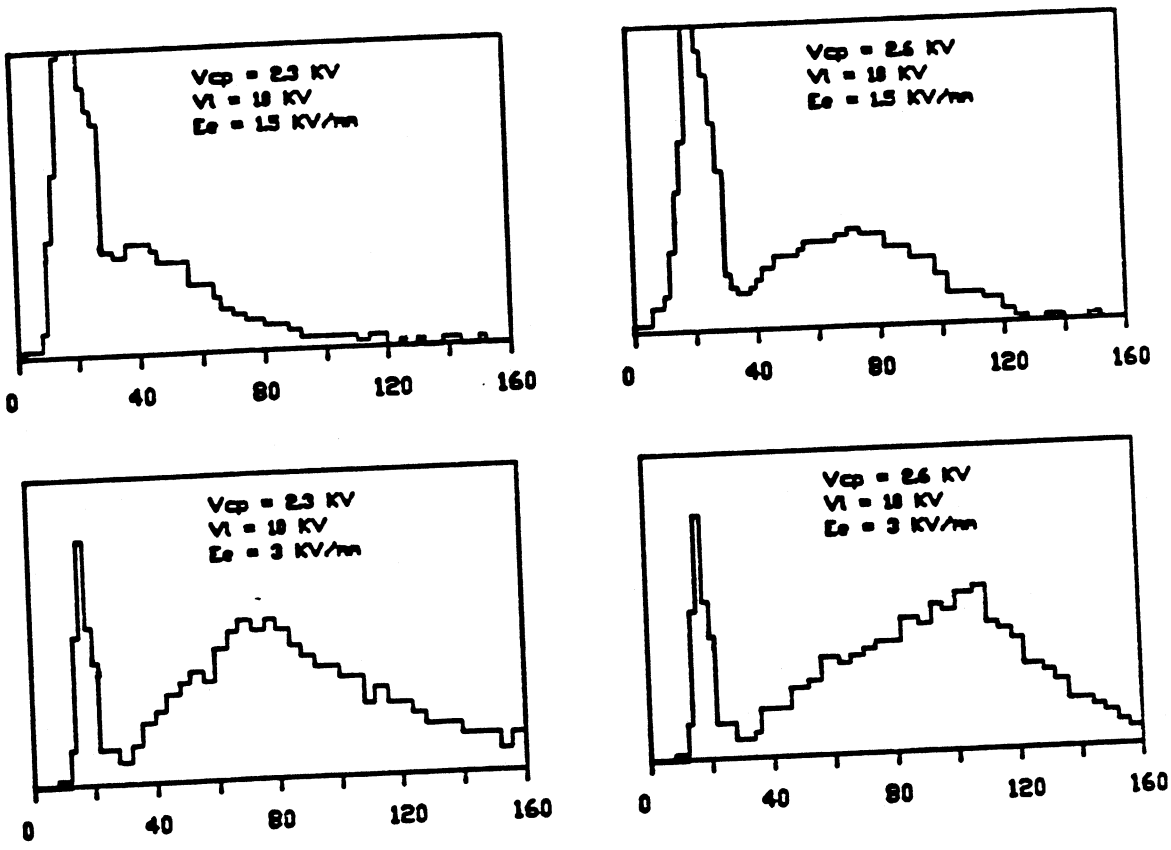

Fig. 3.14 Channel Plate Charge Against Ve and Vcp

3.4 - Conclusions

The early work on the channel plate detector showed that a device of this type could be used as an imaging detector with a resolution better than 250 μm. The potential spatial resolution of the detector should be $\approx$ 70 μm assuming the lens was not being used to magnify the cathode image although this resolution has not yet been attained. It is hoped to attain this resolution with the full RMH read-out with the detector installed in the WA69 electron beam during the main experiment data taking.

The tandem channel plate multipliers have been found to give a gain of about 10^6 with a voltage of 2·7 KV across them. The single electron efficiency of the channel plates was estimated to be about 50%, most of this is accounted for by the fact that only 60% of the channel plate surface is active, the rest being the glass between holes. The lens was found to become efficient with a voltage drop of over 11 KV across it, but the imaging properties of the lens at these voltages are not known. The dependence of the overall efficiency on the lens voltage is determined by three factors, the transport efficiency in the lens itself, the quantum efficiency of the channel plates as a function of the energy of the incident electrons (this peaks at about 7 KeV and then fall slowly) and the efficiency with which electrons are extracted through the micro-mesh in the cathode. The cathode was found to require an electric field of about 30 KV cm^{-1} to get an overall efficiency of 95%. It was found that the cathode has a time hysteresis characteristic when the extraction field was changed. This is due to charging effects in the CsI foam in

the cathode. The charging may be dependent on the beam rate but this has not yet been investigated fully. To alleviate the hysteresis effects and attain efficiencies of 95% it was found necessary to turn off the extraction field between beam bursts and on during the beam spill. Assuming a channel plate and lens efficiency of 40% the number of secondary electrons leaving the cathode was estimated to be of the order 8 although this number is poorly define. By assuming that the initial secondary electron production determines the overall efficiency and that this process is governed by Poisson statistics, an overall efficiency of 95% implies that a mean of 3 secondary electrons are initially produced. The amplification process then increases this number to $\approx 7{\cdot}5$ electrons leaving the cathode, corresponding to a cathode gain of $\approx 2{\cdot}5$. The actual gain in the CsI foam will be higher than this due the loss of electrons at the micro-mesh. All these factors have a significant uncertainty at this point in time as the physics processes involved in the cathode were not fully undestood.

3.5 - References

3-1 High Intensity Beam Profile Detector for Ω'
R. J. Thompson and M. Ibbotson
Manchester Internal Note 1978

3-2 Minimum Ionizing Particle Detection by
Secondary Electron Emission
J. C. Faivre et al IEEE Vol. NS-24, No. 1 Feb 1977

3-3 A New Photocathode for X-Ray Image Intensifiers
Operating in the 1-50 KeV Region
E. Bateman et al RL 79-087

3-4 Introduction to Electron Optics
P. Dahl

3-5 An Image Intensifier Astronomical Telescope
A. W. Woodhead
Philips Technical Review 1963, No. 64, Vol. 4 pg. 88

3-6 Microchannel Plate Photodetectors
Characteristics and Applications
Koichiro Oba Hamamastsu TV Co., LTD. JAPAN

3-7 Development Status of Microchannel Plate Photomultipliers
S. Dhawan IEEE vol. NS-24, No. 1 Feb 1977

and Microchannel Plate Detector
J. L. Wiza NIM 162 (1979) 587-601

3-8 High-Resolution Imaging X-Ray Detector
E. Kellogg et al
Rev. Sci. Instrum., Vol 47, No. 3 (282) Mar 1976

3-9 A Constant Fraction Discriminator for use in
Precise Delay Line Readout Systems
R. Stevenson RL-78-043

3-10 The 25 - 70 GeV Tagged Photon Facility at CERN
D. Aston et al
Nuclear Instruments and Methods 197 (1982) 287-296

3-11 Investigation of the Dielectric Particle Detector
S. M. Gukasian et al NIM 167 (1979) 427-430

3.6 - Figure Captions

3.1 Channel Plate Detector in Region 3

3.2 Channel Plate Detector in Region 4

3.3 The Channel Plate Detector

3.4 The Secondary Emission Cathode

3.5 The Lens Assembly

3.6 Diagram showing Channel Plates

3.7 Charge Sharing on the Read Out Wires

3.8 Delay Line Output

3.9 Rate against extraction and Channel Plate Voltage

3.10 CPM Back Signal Charge and threshold Distributions

3.11 Channel Plate Detector Efficiency

3.12 Channel Plate Efficiency as a Function of Time

3.13 Channel Plate Efficiency Curves With Pulsed Extraction

3.14 Channel Plate Charge Against Ve and Vcp

CHAPTER IV

THE OMEGA SPECTROMETER

AND PARTICLE IDENTIFICATION

Chapter IV

4 - The Omega Spectrometer and Particle Identification

4.1 - Introduction

The Omega Spectrometer and particle identification detectors (Fig. 4.1) were located at the end of the new E1/H1/P1 beam line in the up-graded West Hall at CERN. The Omega Spectrometer consisted of the Omega Magnet and a series of Multi-wire Proportional Chambers (MWPC's) and Drift Chambers inside the Omega field. The hydrogen target was located in the Omega field towards the front of the magnet, with the Omega MWPC's behind and on either side of it. Charged particles produced in the target were tracked through the field using the hits in the chambers and from the curvature of the tracks their momentum was measured..

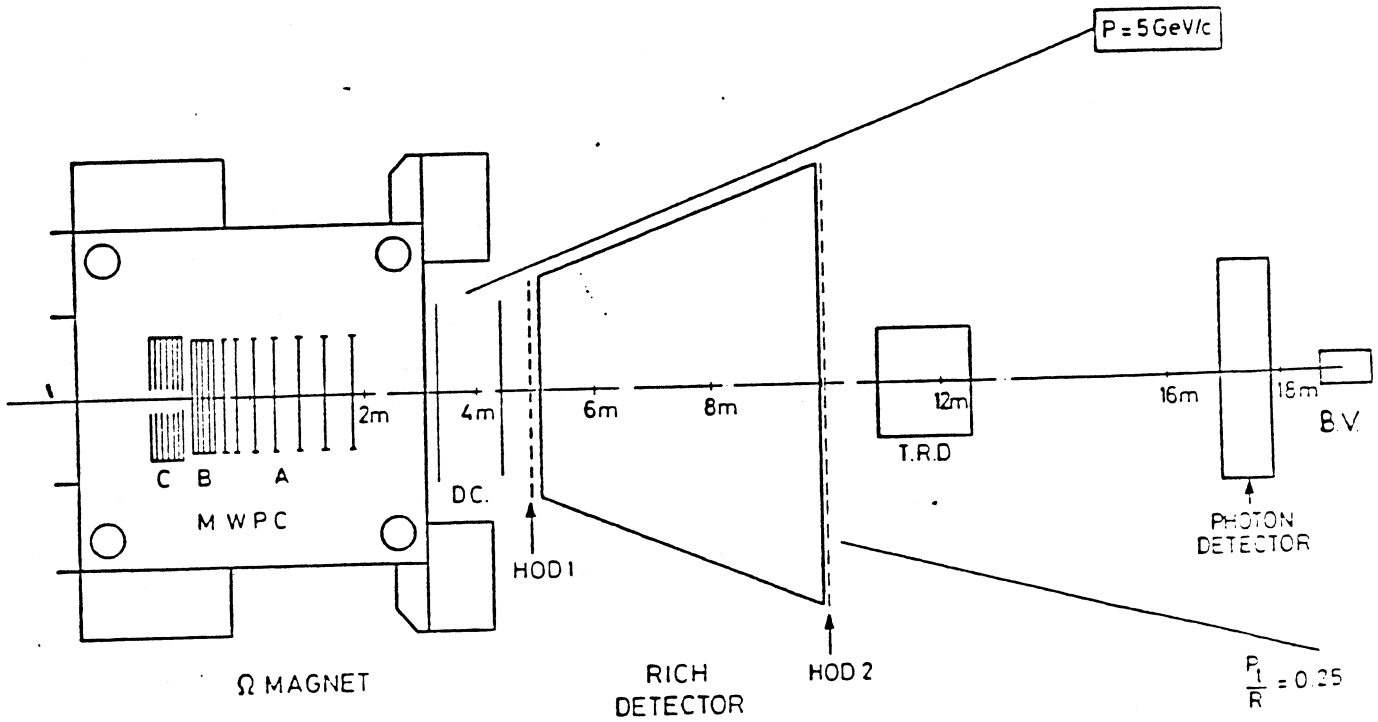

Fig. 4.1 Omega and Particle Identification Detectors

Chapter IV

Charged Particle identification was done using two detectors behing Omega, the Ring Image Čerenkov Detector (RICH) and the Transition Radiation detector (TRAD). The RICH discriminated between π, k and P in the energy range 10 - 70 GeV. The RICH acceptance was closely matched to the size of the aperture in the back of the Omega magnet. The TRAD was used to identify the most forward particles (> 70 Gev). This detector was located behind the RICH with two small active areas either side of the projected photon beam direction.

Neutral particles produced in the target (γ, π^0 and η which decay to $\gamma\gamma$) were detected in the Photon Detector. The Photon Detector was located at 17·5 m behind Omega centre and had an active area of 8 m^2. It measured the position and energy deposited of the incident photons.

A series of trigger detectors were placed between the particle identification detectors. An End-Cap scintillator placed immediately behind the hydrogen target was used to trigger on all photon interactions. The discrimination between hadronic interactions in the hydrogen target and the electromagnetic interactions was achieved using two scintillation counter hodoscope guillotines. These hodoscope guillotines were located either side of the RICH. A Beam Veto was used to remove events where a photon had interacted in the hydrogen target and a second double bremsstrahlung photon had not interacted. The Beam Veto was located behind a hole in the centre of the Photon Detector.

4.2 - The Target Region

The Liquid Hydrogen Target was 60 cm long (≈ 0·006 radiation lengths) and 4·8 cm diameter (Fig. 4.2), it mounted in the forward part of the Omega magnetic field. In front of the target were two scintillation counters (S2 and V2). The small circular counter, S2 was normally used as a trigger with charged beam particles, with the large concentric holey veto V2 to veto stray tracks. In our photon experiment both of these counters were used in veto in the trigger to remove events where photons converted between the tagging target and the hydrogen target. Downstream of the hydrogen target was the End-Cap counter. This scintillation counter was 10 cm diameter and 6 mm thick. It was mounted on a long vertical light guide so that it's photo-multiplier tube could be mounted outside the Omega field (in the hole in the top pole piece). The End-Cap was used in the trigger to detect charged particles leaving the target. It therefore triggered on the full electromagnetic cross-section as well as the smaller hadronic cross-section. Around the target assembly was mounted the Barrel Hodoscope. This counter had 24 slats the length of the target which were arranged radially. The barrel hodoscope was used to detect large transverse momentum tracks from the target fragmentation region. It provided angular measurement as well as a dE/dx measurement for these tracks.

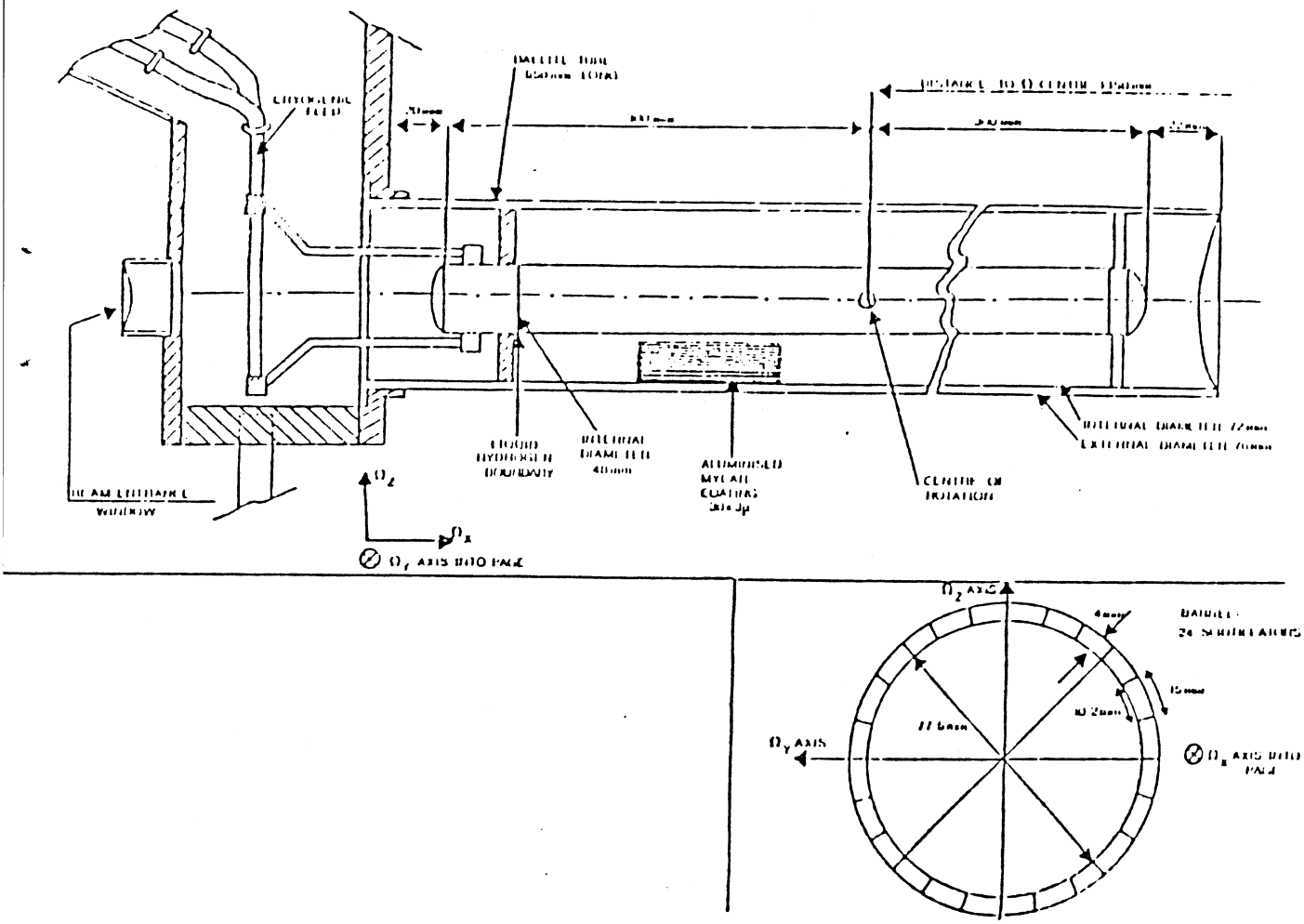

Fig. 4.2 The Liquid Hydrogen Target

4.3 - The Omega Spectrometer

The Omega spectrometer consists of the Omega magnet, three sets of Multi-Wire Proportional Counters (MWPC's), and a pair of large Drift Chambers (Fig. 4.3).

The Omega magnet has two superconducting coils about 2 m radius, and cooled with high pressure helium at 4·2 K. The coils are supported on iron pole pieces held apart by four brass pillars, with

iron return yokes around the front and sides of the magnet. Omega provides a maximum field of 1·8 T in the vertical direction over a volume of about 2 m radius and 1·5 m high. In the WA69 configuration Omega was run at full field. Slight distortions were present in the field due to a large hole in the top pole piece (used to view the spark chambers used in Omega before the MWPC's were installed), and the non uniform distribution of return yokes round the magnet. These were taken into account in the off-line reconstruction program TRIDENT.

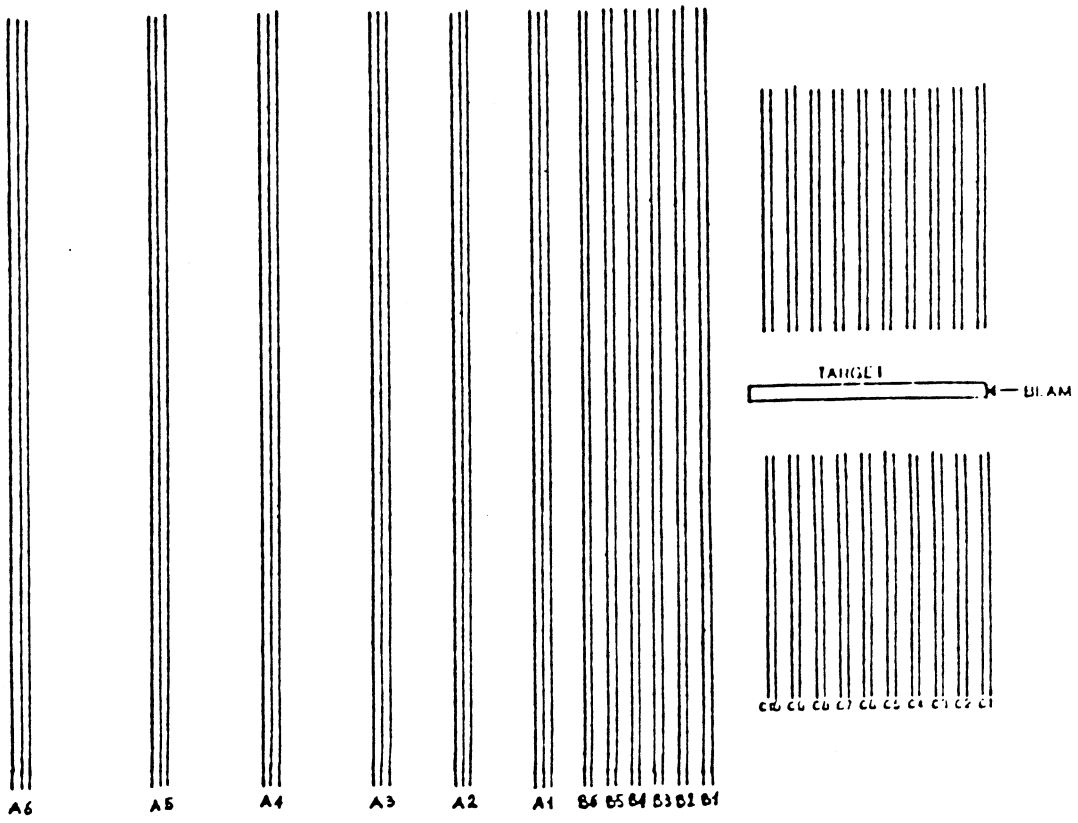

Fig. 4.3 Layout of the Omega Spectrometer

Inside Omega were the three sets of MWPC's, the 'A', 'B', and 'C' chambers. On either side of the target were 10 'C' chambers to

detect tracks from low energy, high P_t charged particles. Each 'C' chamber had 2 planes of wires at 2 mm spacing and orientated (U,Y) and (V,Y) in alternate chambers (where Y denotes planes with vertical wires and U,V denote planes with wires at ±10·14° to vertical). These chambers had an active area of 60 cm either side of the target and 80 cm high. Behind the target and End-Cap were the 8 'B' chambers, each with two planes of 2 mm spaced wires orientated (U,Y) and (V,Y) in alternate planes. Each of the 'B' chambers had an active area of 120 × 150 cm^2 and were spaced at 10 cm intervals. The 'B' chambers were closely spaced to provide the spacial resolution required to separate close tracks and accuretly find vertices. At the back of Omega, still inside the field were the 7 'A' chambers. Each 'A' chamber had 3 planes orientated (U,Y,V) separated by 16 mm, with the wires spaced at 2 mm. The 'A' chambers had the same active area as the 'B' chambers but were arranged with increasing separation towards the back of Omega. The 'A' chambers were further apart than the 'B' because the tracks had been spread out by the magnetic field and so there were less problems with the separation of tracks. At the back of Omega, in the aperture between the side yokes were the two drift chambers. Each drift chamber had four planes 1·8 cm apart, with the wires 5 cm apart and orientated (Y,U,Y',V) in successive planes (where Y' denotes a plane with vertical wires displaced by half a wire spacing with respect to the Y plane). The drift chambers had an active area of 3·3 m × 1·5 m and had a single track resolution of ±0·2 mm and had a two track resolution of ±1·6 mm. The chambers were used to improve the momentum resolution of fast tracks and to improve two track resolution for close tracks.

Figure 4.4 shows two typical events from the on-line event display showing the hit distributions in the Omega chambers. The first event is a multi-prong hadronic event and the second a 4-prong event which is probably a double pair.

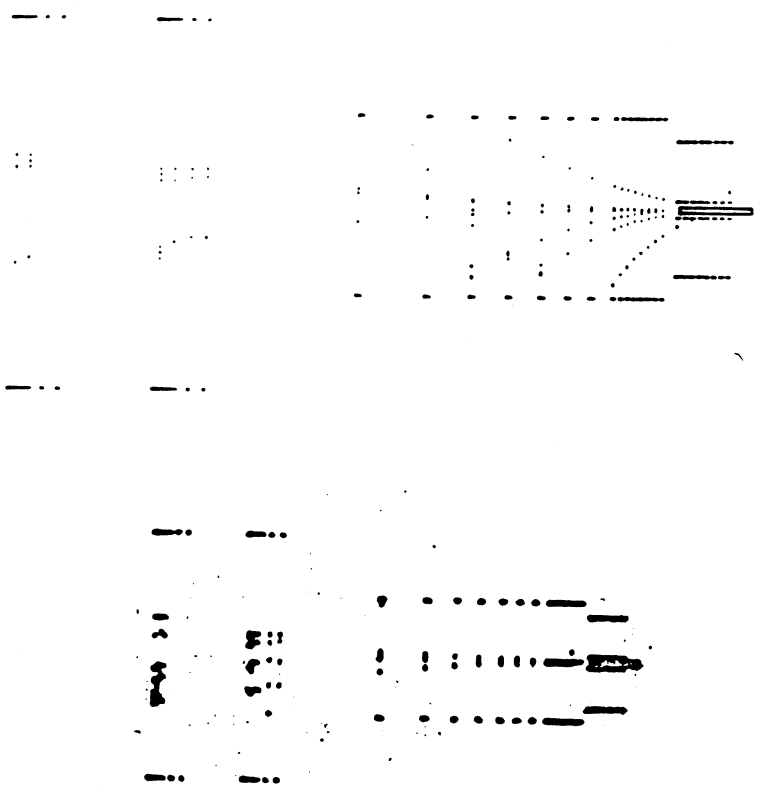

Fig. 4.4 Two Events from the Omega Event Display

4.4 - The Ring Image Cerenkov

A Čerenkov detector is sensitive to the velocity βc of charged particles. When a particle travels through a medium with velocity βc greater than the velocity of light in the medium c/n it will emit Čerenkov photons at an angle θ to the direction of travel.

$$\cos\theta = 1/\beta n$$

The number of Čerenkov photons produced is given by

$$N_\gamma = 370\ L \sin^2\theta \int dE.$$

In a RICH (Ring Image Čerenkov) the photons from particle tracks (which appear as rings at ∞) are focussed into rings on a 2-dimensional photon sensitive detector (Fig. 4.5). A RICH has the advantage over convention threshold Čerenkov's in that it can identify charged particles even if they are close together.

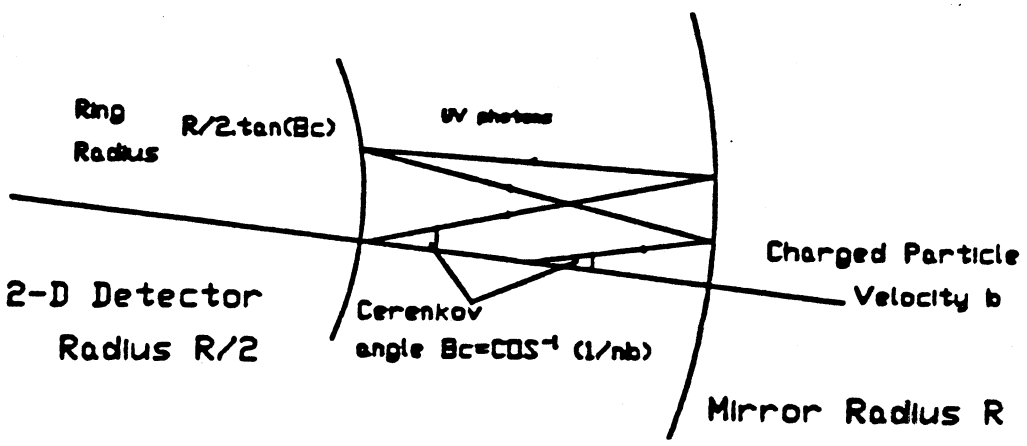

Fig. 4.5 A Schematic Diagram of a RICH

A conventional Čerenkov detector could for example identify that a pion and a kaon went through a particular cell but could not say which was which. In a RICH this problem does not arrise until the two particles pass through the detector so close and with just the right momenta to produce coincident rings. In the RICH used in the experiment (Ref. 4-1) the focussing was done with a concave mirror and the 2-D detector a series of TPC's (Time Projection Chambers) containing the photo-ionizing agent TMAE (Tetrakis dimethyliamine ethylene). The number of Čerenkov photon detected is then given by

$$N_e = 370\ L \sin^2\Theta \int Q(E)R(E)T_w(E)T_g(E)dE$$
$$= N_0\ L \sin^2\Theta \qquad L \text{ in cm.}$$

Where Q(E) is the quantum efficiency of the TMAE, R(E) is the reflectivity of the mirrors, $T_w(E)$ is the transmission of the radiator ($\approx$ 100%), and $T_w(E)$ the transmission of the windows separating the radiator and the TPC's. With the parameters shown in Figure 4.6, $N_0 \approx 150$. Using a value of $N_0 = 90$ and a 5 m argon radiator the ring radii and number of photons detected are plotted for π, k and P (Fig. 4.7).

The RICH detector (Fig. 4.8) consisted of a 5 m atmospheric pressure gas radiator. The gas in the radiator (either nitrogen or argon) was kept free of oxygen and water vapour to better than 2 ppm and 10 ppm respectively. In front of the back wall of the radiator was the multi-element mirror with a focal length of 5 m. Each of the 81 hexagonal mirror elements was made from 6 mm glass coated with aluminium and magnesium fluoride on the front surface. The mirrors had a reflectivity of better than 85% in the UV. At the front of the radiator were 16 TPC's (Time Projection Chambers) separated from the

radiator gas by quartz windows. The TPC's covered an area of $3{\cdot}2 \times 1{\cdot}6\ m^2$ and were positioned at the focal plane of the mirrors. The TPC's were run on a mixture of methane and isobutane with traces of TMAE. The TMAE was used to convert the UV Čerenkov photons focused on to the TPC's by the mirrors into electrons. The electrons drifted on to the row of sense wires at the center of the TPC's (Fig. 4.9) from which the position of the detected γ is calculated. Each chamber contained 192 wires at a 4 mm separation.

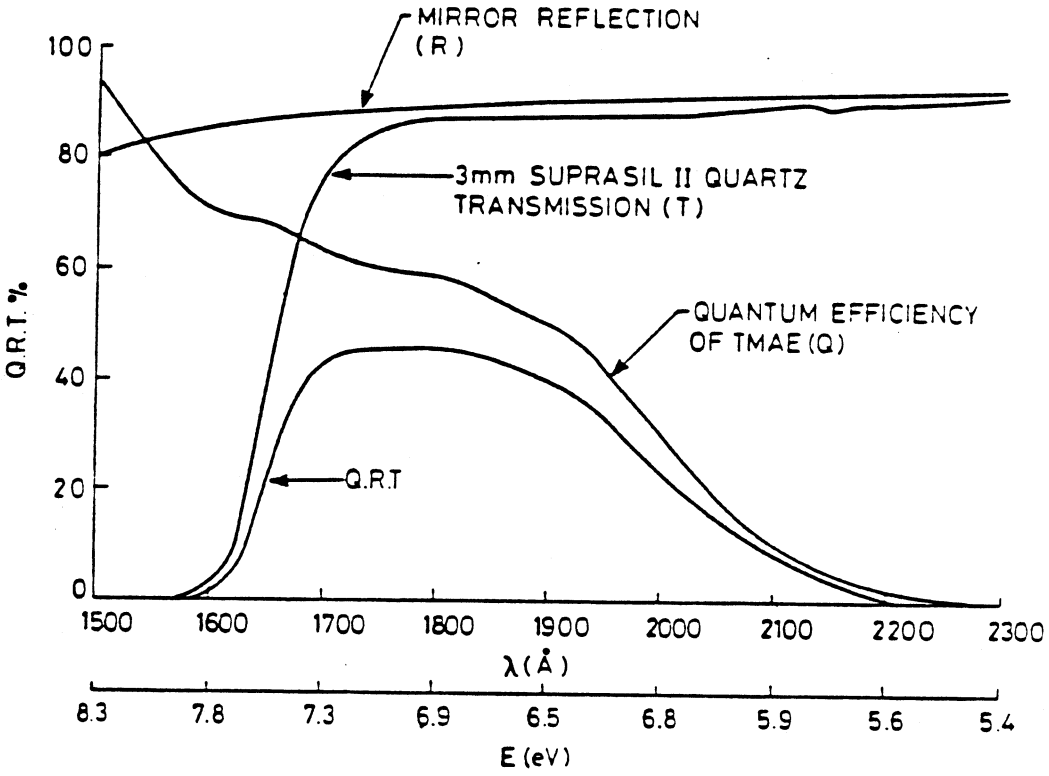

Fig. 4.6 Ring Image Cherenkov Efficiency Parameters

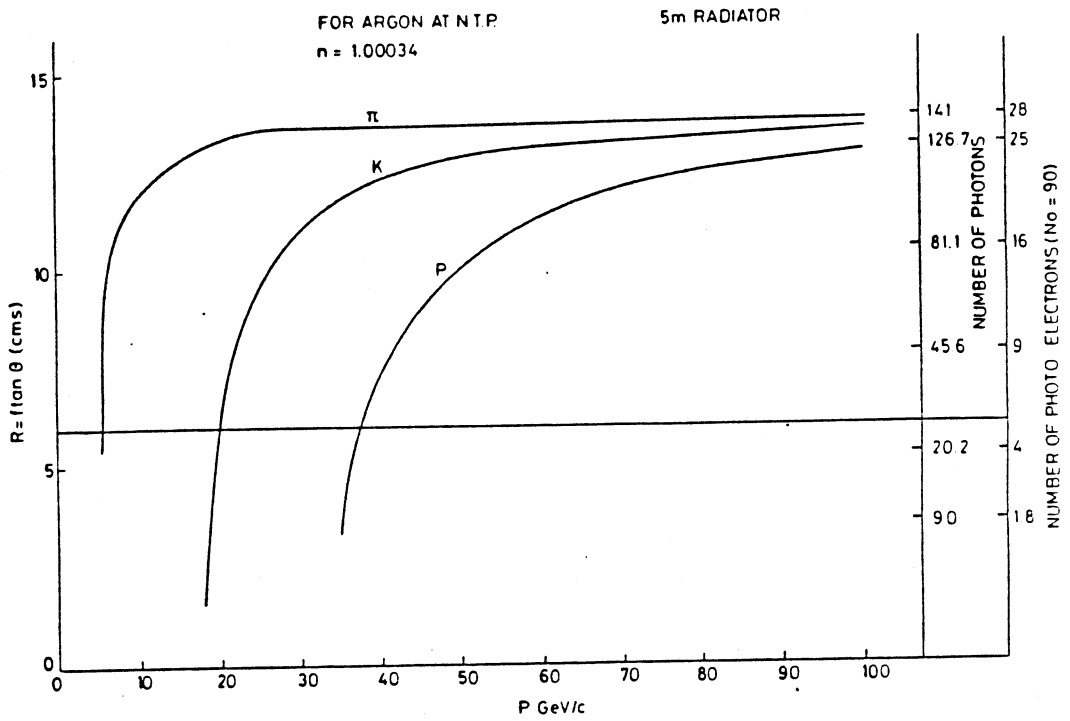

Fig. 4.7 Ring Radii and N_e against Energy

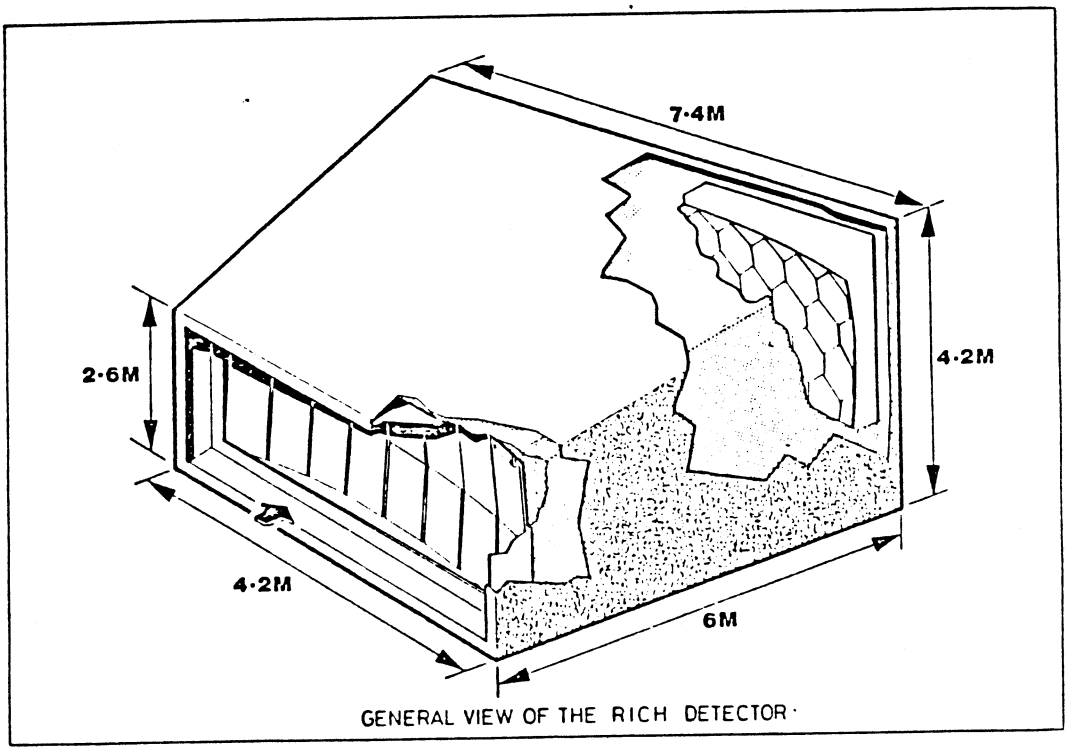

Fig. 4.8 The WA69 Ring Image Cherenkov Detector

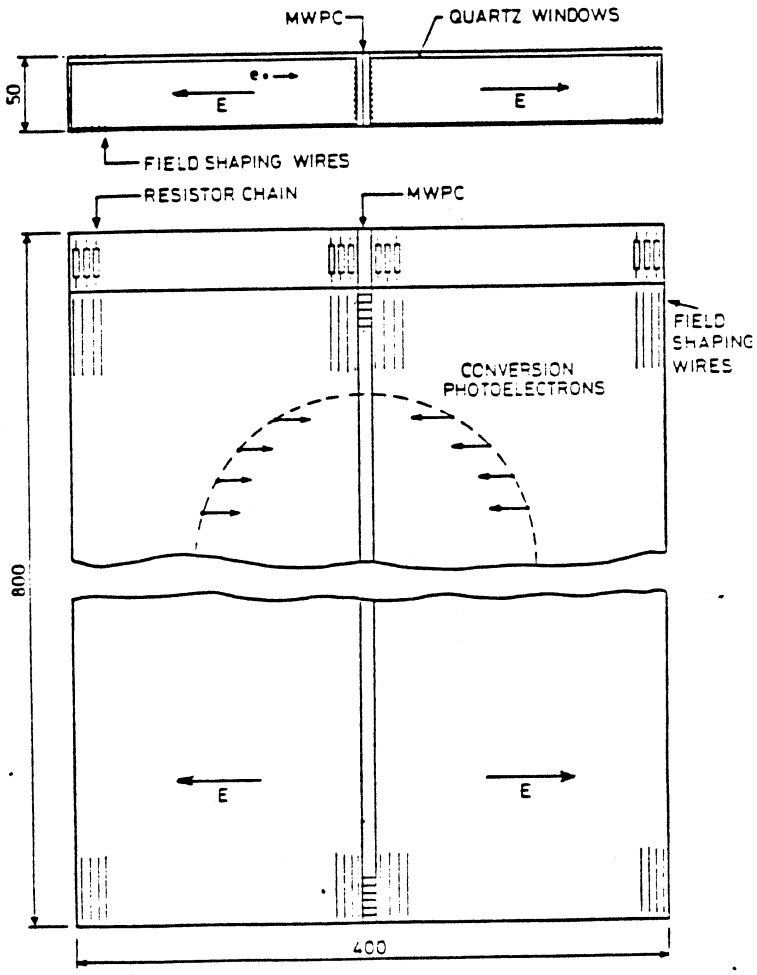

Fig. 4.9 The RICH Time Projection Chambers

Readout of the RICH TDC's used a system of TSE's (Time Slice Encoders) to provide multi-hit time measurement on each wire. Each wire was equipped with a hybrid pre-ampilfiers mounted on the chamber, followed by a discriminator and serial bit memory. The serial memory was clocked at a rate equivalent to 4 mm in the drift space of the TPC's. If a hit sensed in a particular clock cycle the current bit in the serial memory was set and if no hit was sensed the bit was cleared. If an event occured, a strobe was sent to the TSE's at a fixed time after the event. This strobe stopped the clock on the serial memories. Readout of the event consisted of working back from the address where the clock was stopped to find hits. For each hit

found the chamber and wire numbers were recorded together with the difference between the stop address and the hit address.

Analysis of the test beam data from the RICH, taken with a 100 GeV pion beam (with some K and P contamination) showed clearly separated rings in the TPC's (Fig. 4.10). From events taken with a 100 GeV pion beam the ring radii and numbers of detected photons was calculated (Fig. 4.11). From these plots an N_0 was found to be about 75. With this value of N_0 rings are clearly visible in single events. Off-line analysis of the RICH data and using the information from the Omega Spectrometer identification of the tracks was made. Figure 4.12 shows a ring due to a pion and a ring due to a proton with cirles drawn on corresponding to the radii of the pion and proton at the momentun given by Omega.

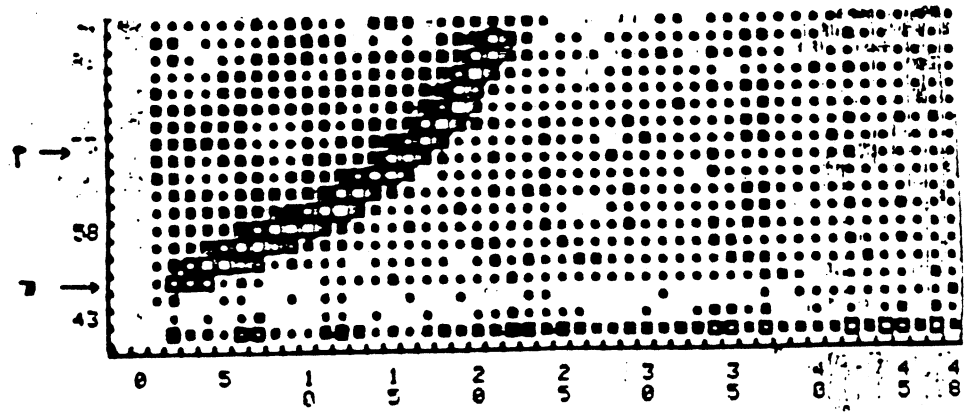

Fig. 4.10 RICH TPC Hit Distributions

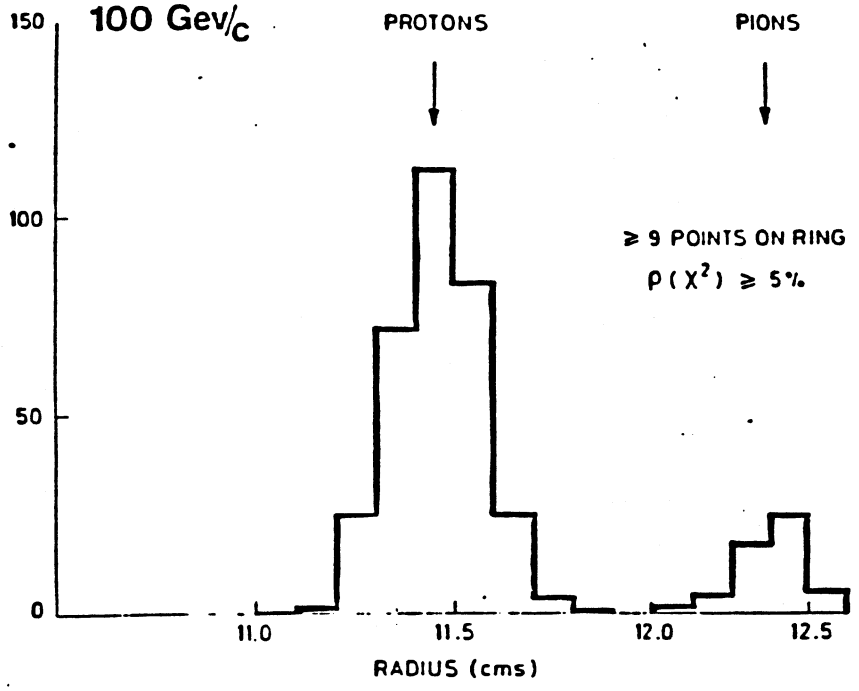

Fig. 4.11 Distribution of RICH Radii for a 100 GeV Proton Beam

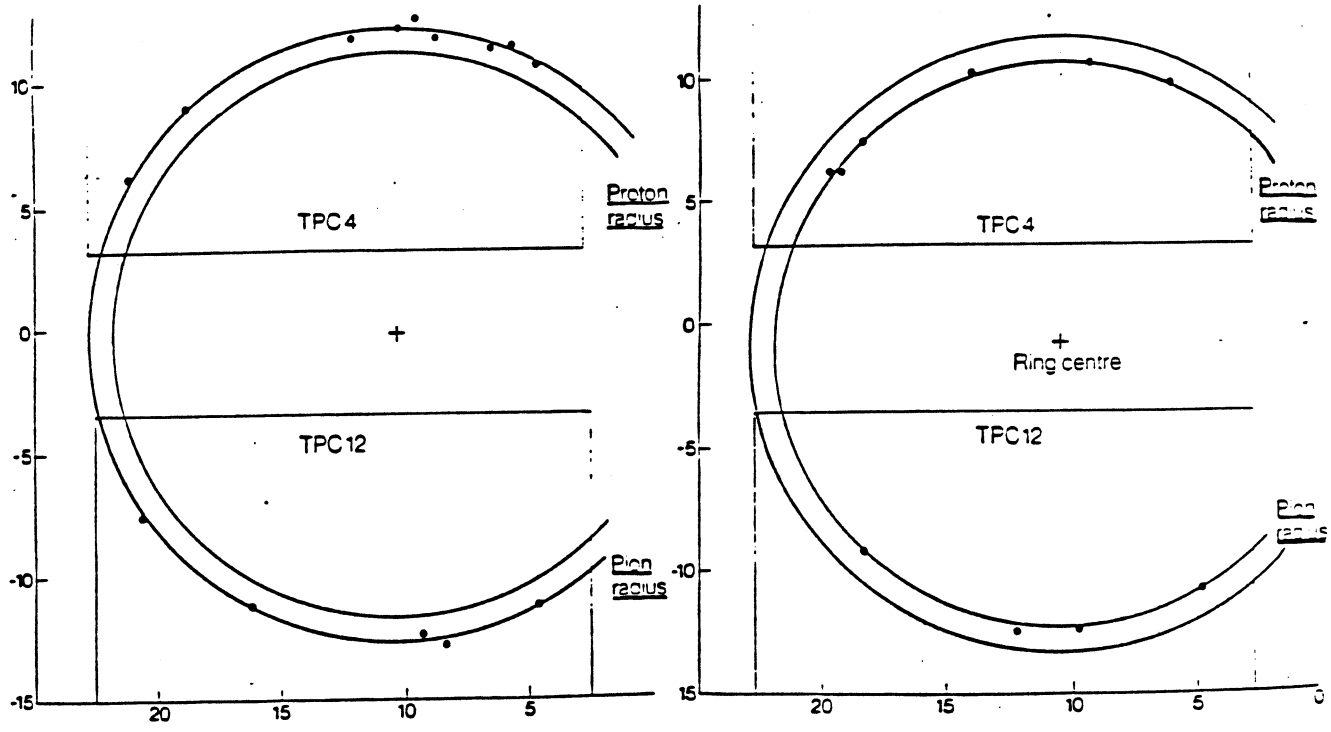

Fig. 4.12 RICH Single Events

4.5 - The Photon Detector

The Photon Detector, built by the WA70 experiment (Ref. 4-2) was used instead of the old photon detector Olga, Penelope, and Sampler used on earlier Omega experiments. The WA70 photon detector (Fig. 4.13) consisted of twelve modules of a lead liquid scintillator calorimeter arranged in quadrants, with an active area of $4 \times 4\ m^2$. Each of the twelve modules $2\ m \times 2\ m \times 10{\cdot}4\ cm$ had 10 sheets of lead 4·2 mm thick, alternating with 10 sheets of teflon tubes 4 mm diameter containing the liquid scintillator. The teflon tubes were arranged in orthogonal layers and bundled into channels to provide a crude 2-dimensional readout (Fig. 4.14). Each channel was connected to a photo-multiplier tube.

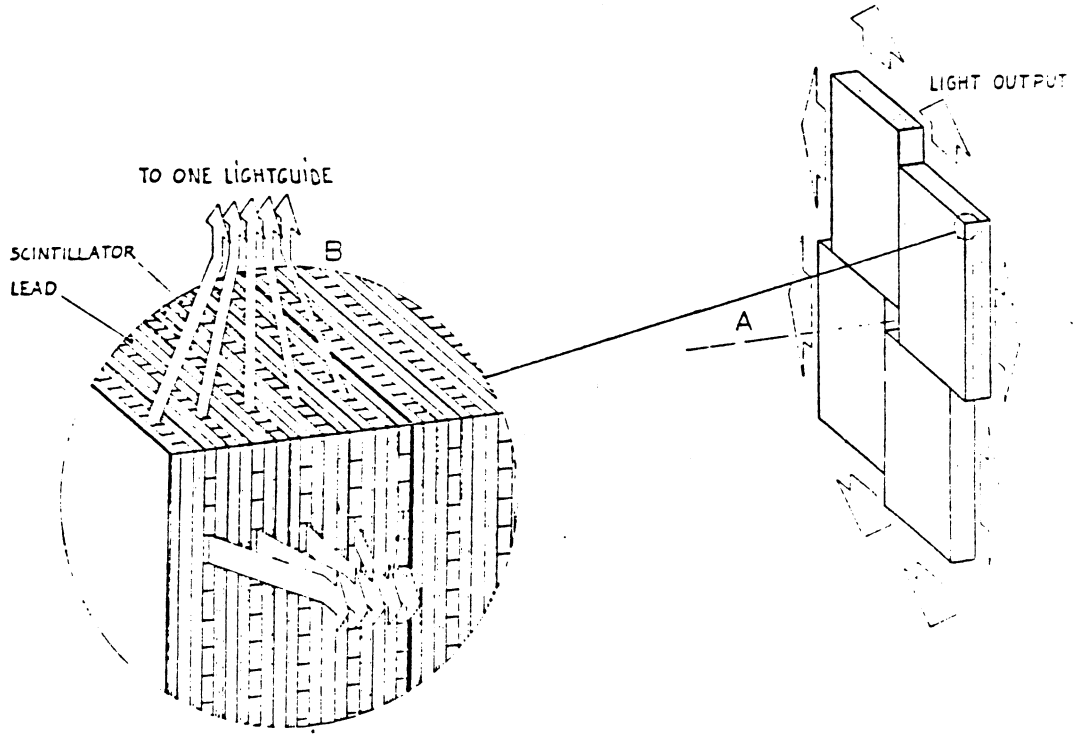

Fig. 4.13 The WA70 Photon Detector

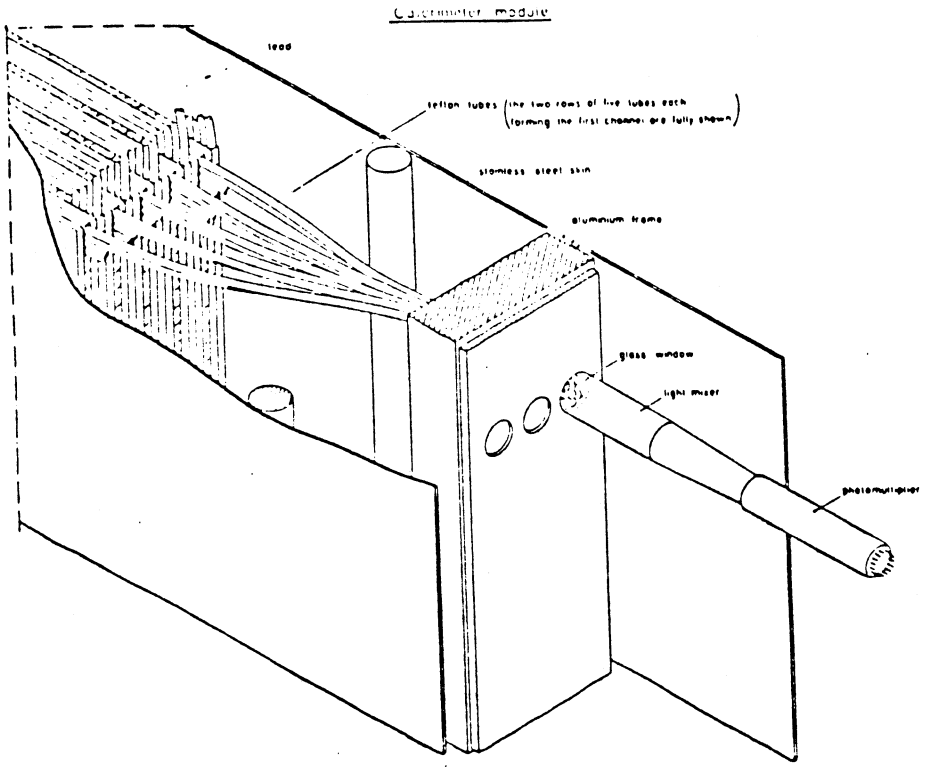

Fig. 4.14 Orthogonal Planes in the Photon Detector

Read out of the detector used ADC's to provide the energy deposition measurement and TDC on the front modules to improve the spatial resolution by time-of-flight measurement. The Photon Detector had an energy resolution of

$$\sigma/E = 0{\cdot}16/\sqrt{E} + 0{\cdot}04, \qquad (E \text{ in GeV})$$

and a spatial resolution of ≈ 4 mm.

In the WA69 configuration the Photon Detector was placed at 17·5 m from Omega centre and had a 40 × 40 cm^2 hole between the quadrants. This hole was to let the non-interacting beam photon through on to the Beam Veto. Ideally the hole should have been 6 × 6 cm^2 to contain to full photon beam, but this was not mechanically possible. To reduce the hole in the Photon Detector a

small Photon Detector is being built and will be used for the main WA69 data taking. This inner Photon Detector will be a lead-scintillating fibre sandwich with the fibres arranged longitudinally.

The Photon Detector on-line event display produced maps of the photon detector showing the position and energy deposition of showers. Figure 4.15 shows two such plots, the first an electromagnetic pair with two large showers in the medium plane and the second a multiprong hadronic event with small showers due to hadrons and some large electromagnetic showers. The off-line analysis developed to test the photon detector gave an inclusive 2 photon mass plot (Fig. 4.16) showing a clear peak at the π^0 mass.

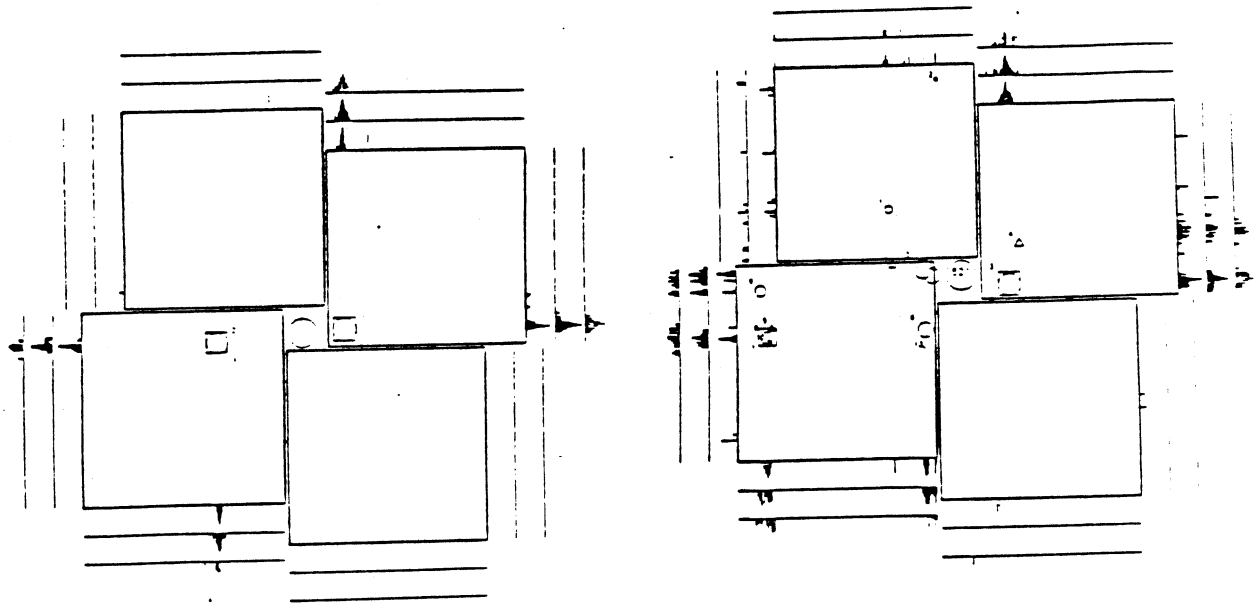

Fig. 4.15 Photon Detector Events

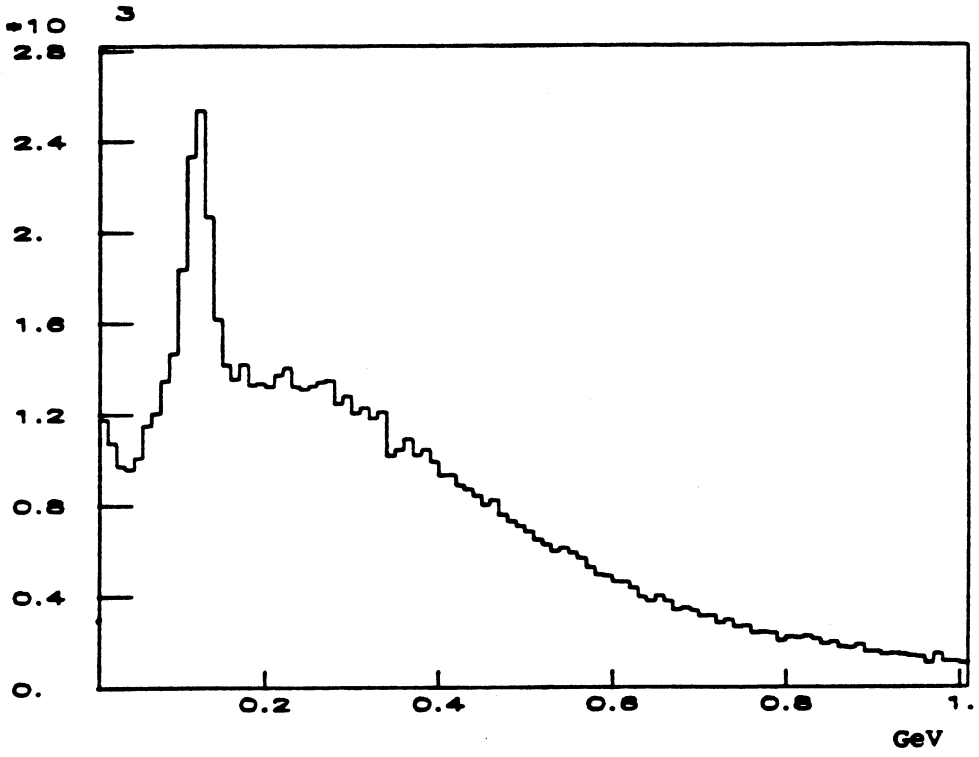

Fig. 4.16 Photon Detector Pi-Zero Inv. Mass

4.6 - The Transition Radiation Detector

The TRAD (Transition Radiation Detector) discriminates charged particles according to their lorentz γ. By a process similar to Čerenkov radiation, when a particle crosses a boundary between two mediums with different refractive indices transition radiation photons (in the X-ray region) are produced. The amount of energy produced in the transition radiation is proportional to the γ of the particle. The effect is enhanced by having many changes of refractive index in the radiator material. By careful choice of thickneses of the two materials in the radiator further enhancements can be obtained by coherent X-ray production.

The TRAD (Fig. 4.17) consisted of a series of 10 radiator filled with short strands of a man-made fibre. The X-ray photons produced were detected in a MWPC behind each radiator. Each of the MWPC's had an active area of 50 × 60 cm^2 on either side of the non-interacting photon beam. The MWPC's used a gas mixture containing Xenon to detect the X-ray photons. When a charged particle goes through the MWPC's the ionization produced drifts in on to a wire giving a pulse wide in time, due to the different distances the ionization drifts. When a transition radiation X-ray photon converts in the chamber it produces a short pulse, because the conversion takes place at a point. Since the photons are produced in the forward direction the short transition radiation pulse sat upon the longer track pulse. Read out of the TRAD consisted of a two level discriminator system on each wire, the lower level to trigger on the pulse due to a track and the upper level on a track pulse with the addition of extra energy due to transition radiation. The wires in the chambers were also clustered linearly with the resultant pulses going to ADC so that the energy deposition could be measured.

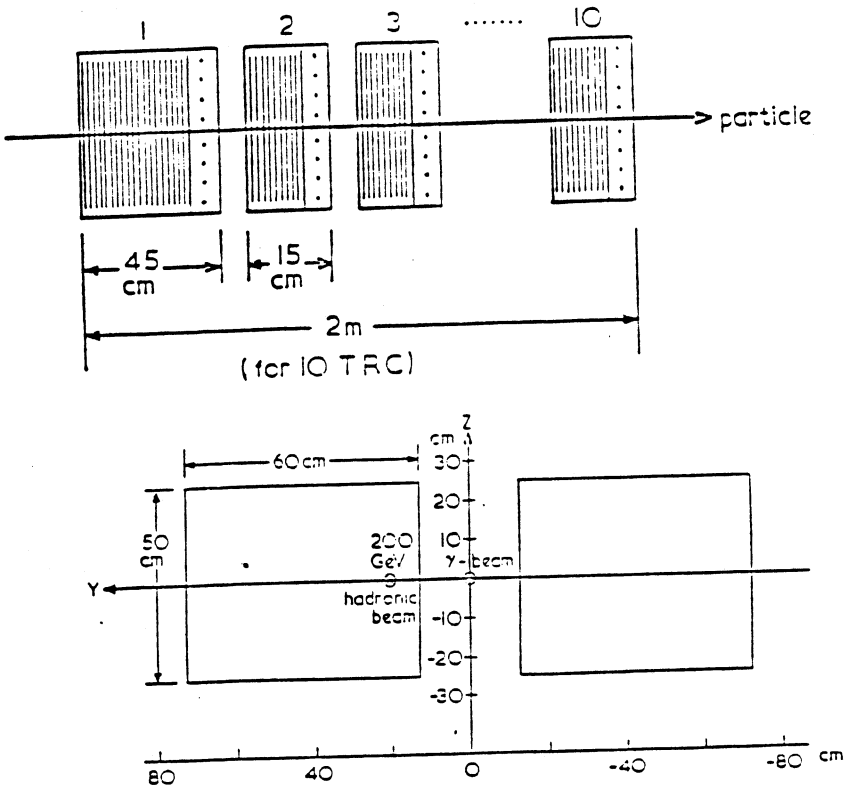

Fig. 4.17 The Transition Radiation Detector

The off-line TRAD reconstruction package can then calculate the excess energy seen in the TRAD for each track and hence calculate the particles lorentz γ using the momentum of the track from the Omega Spectrometer.

4.7 - Trigger Detectors

The main trigger detectors behind Omega were the two scintillation counter hodoscope guillotines and the beam veto.

The hodoscope guillotines consisted of the two large scintillator hodoscopes H1 and H4 (Fig. 4.18). These hodoscopes were separated into upper and lower halves with a gap in the middle corresponding to the region into which the e^+e^- pairs passed. Each half of the hodoscope consisted of an array of vertical slats (32 in H1 and 15 in H4) with a photo-multiplier tube on the outside edge. The position and width of the gap in the middle of the hodoscopes was arranged so that the electromagnetic pairs in the medium plane passed through the gap but at least one track in the hadronic events passed through the slats in both hodoscopes. The actual gap varied across the hodoscopes to account for non-uniformities in the Omega field. Monte-Carlo simulation of this type of guillotine showed that the acceptance for high multiplicity events was good, but for low multiplicity events with forward production the acceptance would be reduced due to particles going through the gap. The choice of gap was first estimated with the simulation mentioned above, then re-estimated using real data taken with the gap set too small.

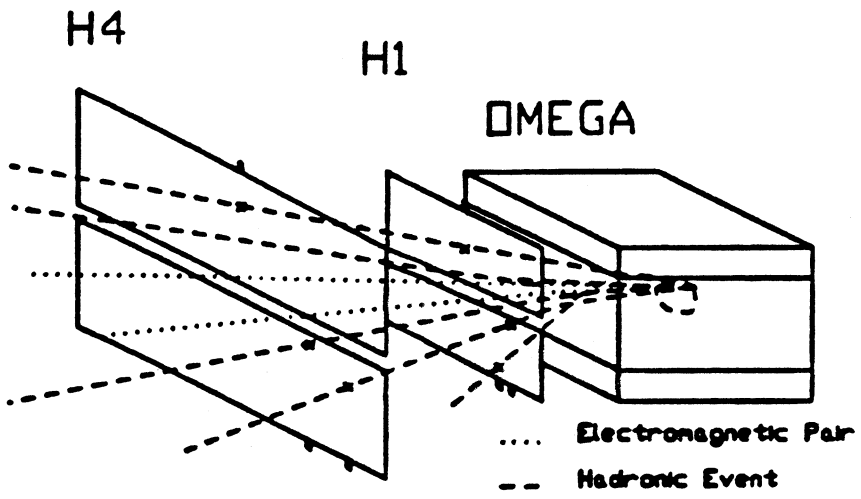

Fig. 4.18 The Scintillation counter Hodoscope Guillotines

The Beam Veto (Ref. 4-3) was used to veto events with two beam photons, one interacting in the hydrogen target and the other not interacting. These events were caused by double bremsstrahlung in the tagging target. The beam veto was set up to veto events with a photon entering it with more than 30 GeV. For lower energy photons entering the counter, the energy was measured and the position of the shower in the detector estimated. This information could be used to correct events with a second low energy photon. The detector (Fig. 4.19) consisted of 54 layers of lead 2 mm thick alternated with scintillator sheets 6 mm thick. This gave a depth of 20 radiation lengths and an effective area 16 cm × 16 cm. Three BBQ wave-length shift light guides were used (with a photo-multiplier tube on each end) along each side of the lead scintillator sandwich to collect the

light. The total energy deposition could then be calculated from the sum of the signals from the 24 photo-multiplier tubes and the position from a linear combination of the signals. The energy resolution of the beam veto was found to be

$$\sigma/E = 0{\cdot}02 + 0{\cdot}116/\sqrt{E}, \qquad E \text{ in GeV.}$$

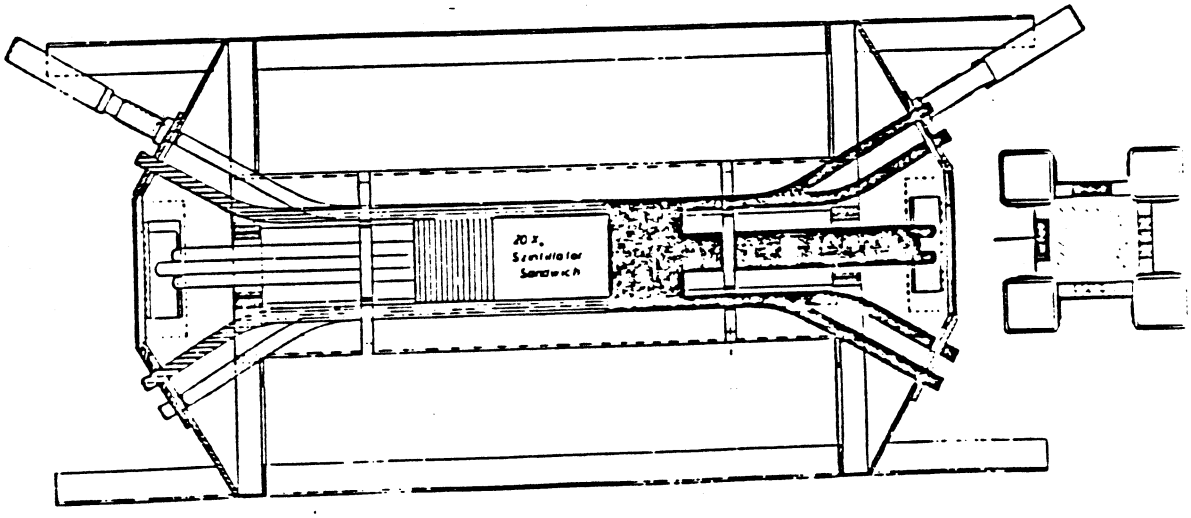

Fig. 4.19 The Beam Veto

4.8 - References

4-1 A Ring Image Čerenkov Detector for the Omega Spectrometer
M. Davenport et al
IEEE NS-30 No. 1 (1983) 35

4-2 Study of Direct Photon Events in Hadronic Collisions
M. Martin Expt. WA70 Experiments at CERN in 1983

4-3 Diploma Report
R. Oedingen
Physics Department Bonn University

4.9 - Figure Captions

4.1 Omega and Particle Identification Detectors

4.2 The Liquid Hydrogen Target

4.3 Layout of the Omega Spectrometer

4.4 Two Events from the Omega Event Display

4.5 A Schematic Diagram of a RICH

4.6 Ring Image Cherenkov Efficiency Parameters

4.7 Ring Radii and N_e against Energy

4.8 The WA69 Ring Image Cherenkov Detector

4.9 The RICH Time Projection Chambers

4.10 RICH TPC Hit Distributions

4.11 Distribution of RICH Radii for a 100 GeV Proton Beam

4.12 RICH Single Events

4.13 The WA70 Photon Detector

4.14 Orthogonal Planes in the Photon Detector

4.15 Photon Detector Events

4.16 Photon Detector Pi-Zero Inv. Mass

4.17 The Transition Radiation Detector

4.18 The Scintillation counter Hodoscope Guillotines

4.19 The Beam Veto

CHAPTER V

THE TRIGGER AND DATA ACQUISITION

Chapter V

5 - The Trigger and Data Acquisition System

5.1 - Introduction

The trigger (Fig. 5.1), used to select events, consisted of three levels. The first level (described in detail in section 2.5) triggered on good photons interacting in the hydrogen target. The second level of trigger selected potential hadronic events from the dominant electromagnetic interactions in the hydrogen target. The third level of the trigger provided a filter to remove any residual electromagnetic contamination and selective triggering on specific classes of hadronic events. Once an event had been selected by the third level of the trigger, an interrupt was sent to the DAC (Data Acquisition Computer) to initiate the reading of the event from the read out system. Associated with the trigger logic was a gating system, the so called 'dead time logic'. This prevented the DAC getting an interrupt from a second event while it was still processing the previous event. It also controlled the latching of the data from each event into the read out system. The DAC was also used to run programs to monitor the data being taken, and to control various aspects of the experiment.

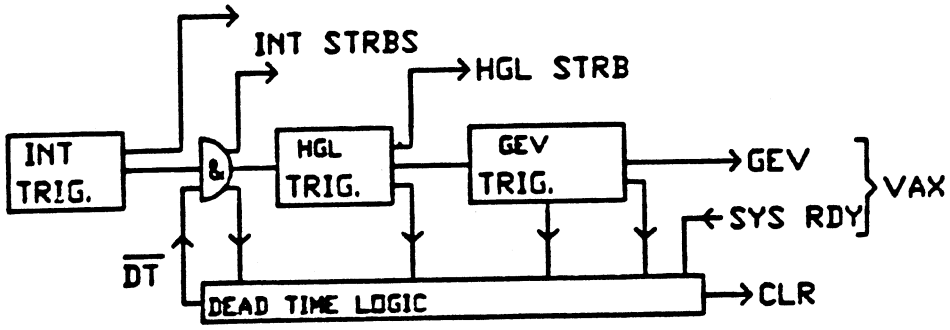

Fig. 5.1 Block Diagram of the Trigger

5.2 - The Trigger

The first stage of the trigger, the interaction trigger (INT), provided a fast strobe to intermediate gates in the read out system and strobed the logic for the second stage trigger. At this stage the trigger signals ran at the 'true' interaction rate because no dead time had been introduced. The INT passed through the dead time gate to the second level of the trigger, the hadron guillotine trigger (HGL). In the HGL trigger the interaction trigger was combined with the signals from the two guillotine hodoscopes behind Omega and the beam veto. Following the HGL trigger the data from the various detectors was strobed into their respective read out systems. Since

many of the read out devices depended on the measurement of time to determine the position of hits in chambers (eg drift chambers), the HGL trigger had to be at a fixed time after the event passed the centre of Omega (the timing reference point). Other read out devices also required a reasonably accurately timed HGL to ensure that only the true event was strobed and not part of another event or noise pulses. The HGL then started the third and somewhat slower stage of the trigger, the Good Event Trigger (GEV). Following the GEV a signal was sent to the DAC to start the read out system. If an event had satisfied an earlier level of the trigger but had not produced a GEV, the dead time logic sent a reset signal to clear the read out system and opened the dead time gate for the next event. This also happened once the DAC had finished processing an event.

5.2.1 - The Interaction Trigger

The interaction trigger as described in Chapter 2 triggered on the full electromagnetic cross-section and the small hadronic cross-section for the photons in the hydrogen target. It consisted of forming the Quick Tag from the coincidence of the Lead Glass and hodoscopes in region 4 and combining it with the Radiation Veto, Holey vetos and Charge particle vetos to form the TAG.

$$TAG = H4.1 \cdot H4.2 \cdot LG \cdot \overline{RV} \cdot \overline{HOVs} \cdot \overline{S2+V2}$$

The TAG-INT was then formed by the coincidence of the TAG and the End-Cap counter.

$$TAG\text{-}INT = TAG \cdot EC$$

Finally, to form the INteraction Trigger (INT) other fast calibration and monitor triggers were added to the Tag-Int.

$$INT = TAG\text{-}INT + Monitors$$

5.2.2 - The Hadron Guillotine Trigger

The second stage of the Trigger (Fig. 5.2) was designed to separate potential hadrons from the dominant e^+e^- pair production. This was done by making use of the two Omega Hodoscopes H1 and H4 as guillotine hodoscopes (described in Chapter 4). In order to make the Hadron GuiLlotine trigger (HGL) the outputs from the discriminators for each hodoscope slat were passed through CHESTER's (2×16 channel strobed coincidence registers followed by a first-in-first-out memory read out system: Ref. 5-1). In the first part of the CHESTER's the signals were strobed with the interaction trigger (dead time gated) to select only hits corresponding to good photons. These signals were then 'ORed' to provide 4 signals corresponding to hits in $H1_t$, $H1_b$, $H4_t$, and $H4_b$. A switching matrix then selected the required combination of the 4 signals using control levels. Normal data taking used the so-called 'Doubles' trigger.

$$\text{'Doubles'} = H1_t \cdot H4_t + H1_b \cdot H4_b$$

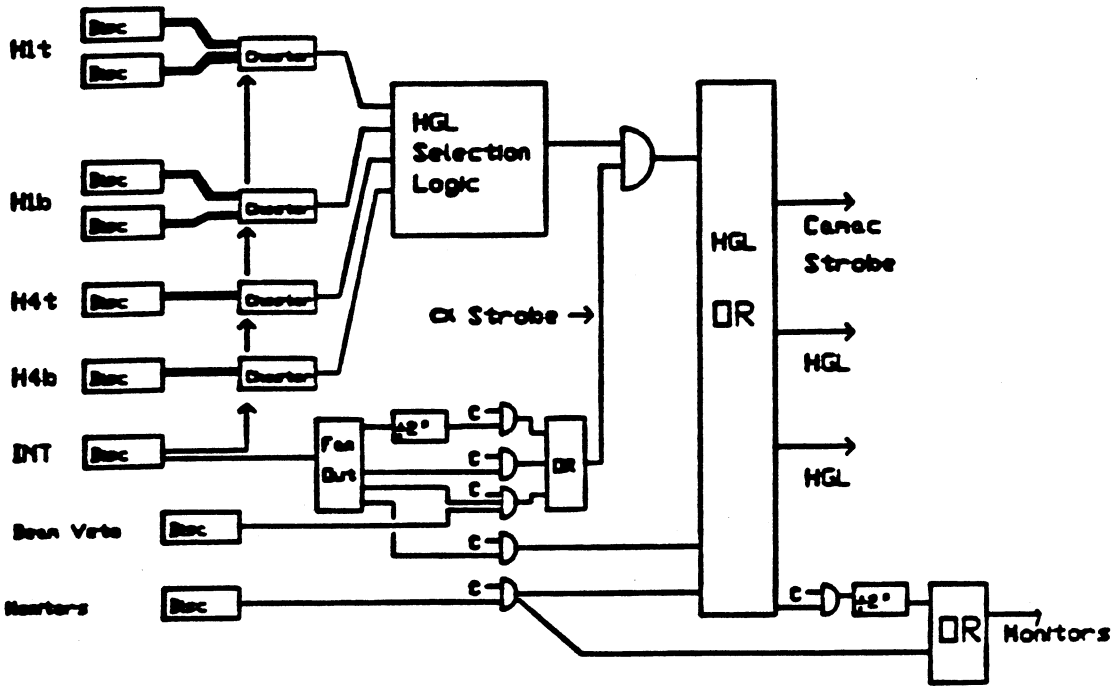

Fig. 5.2 The Hadron Guillotine Trigger

At the same time as the switching matrix was taking place the α strobe was formed. It was formed from the interaction trigger gated with the signal from the Beam Veto, to eliminate events with a second hard photon from double bremsstrahlung. The output from the switching matrix was then combined with the α strobe to create a precisely timed (HGL) trigger. The rest of the HGL logic was used to pass the monitor channels through the HGL trigger with or without the requirement of guillotines and to monitor the beam veto performance. As in the interaction trigger selection of the required trigger was done using control levels generated in the trigger control program TRIGGER running on the DAC.

5.2.3 - The Good Event Trigger

The final stage of the trigger (Fig. 5.3), the GEV (Good Event Trigger) was designed to suppress any residual electromagnetic pairs and provide the possibility of preferential selection of certain types of hadronic physics. A number of different techniques were used to perform this operation. There were four main catogories of final trigger of which any combination could be selected.

i, The Matrix Coincidence between the slats of H1 and H4 was used to reduce the random noise and soft photon noise in the hodoscope guillotines. This was constructed using Bit Assigners and Arithmetic & Logic units (Ref. 5-1). The matrix coincidence was set up such that it only allowed the coincidence of slats in H1 with H4 corresponding to reasonable tracks from Omega. It could be asked to select one track in either the top or bottom or both parts of the guillotine.

ii, The M4 Guillotine provided an extension of the matrix coincidence by asking for a track (top or bottom) as found by matrix coincidence and a corresponding hit in the M4 chamber. This trigger would select forward tracks and be less susceptible to low energy photons since they were less likely to reach and convert in the M4 chamber. Again, as with the matrix coincidence, combinations of top, bottom and both could be selected.

iii, The MY Multiplicity Trigger required more than three hits in at least two out of the four planes of the MY drift chambers just outside the Omega field. A value of three was chosen so that the trigger would not fire on pairs with two hits in each chamber, but would fire for hadronic events with at least three forward tracks. The two out of four requirement meant that random hits and

inefficiencies in single planes would be suppressed. Such a trigger would bias strongly against elastic ρ, ω and ϕ photoproduction since they are dominated by two charged prongs in the final state ($\pi^+\pi^-(n\pi^0)$ and k^+k^- respectively). The MY multiplicity could also be used to select only high multiplicity events by requiring a number greater than three in each chamber. This would preferentially select hard jet like events.

iv, The A6 Multiplicity Trigger required at least three hits in the second from last MWPC inside Omega (the A6 chamber). This trigger would have a similar effect to the MY multiplicity trigger. It had the problem that it was slow compared with the other three final triggers and suffered from inefficiencies around the medium plane due to support wires.

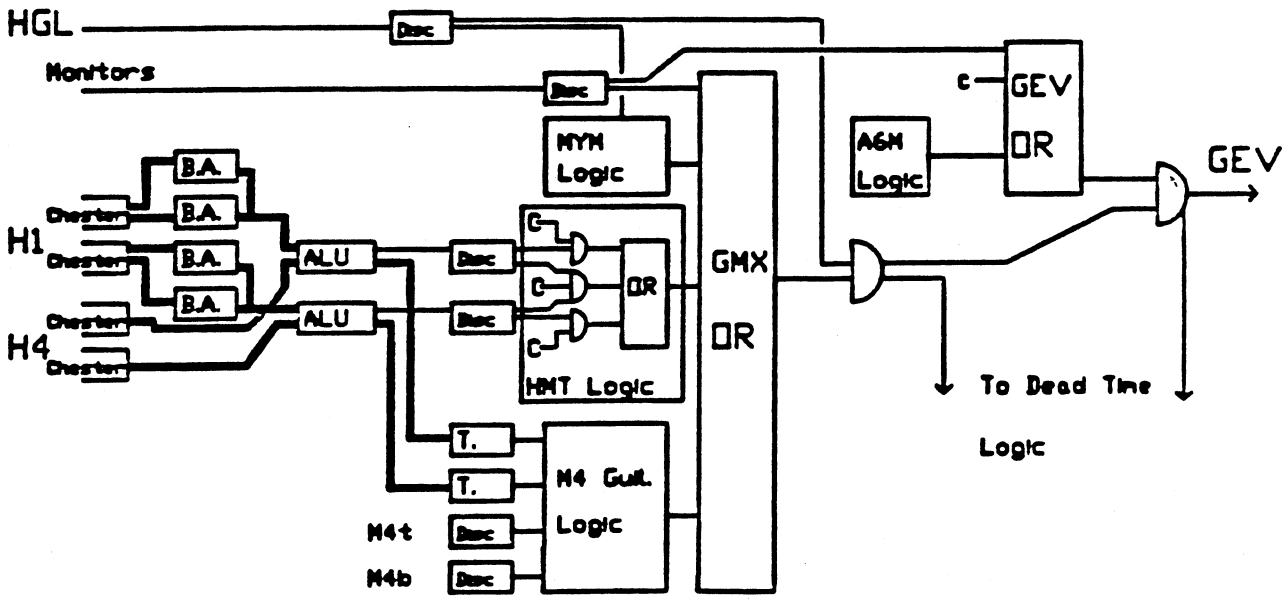

Fig. 5.3 The Good Event Trigger

Since the first three final triggers were fast compared to the last they were combined in the required combination to form the intermediate GMX trigger. At this stage, the monitor triggers were re-combined with the trigger. The GMX trigger was then combined with the HMT trigger and the A6M trigger (if required) to form the final GEV trigger. For the data taking in December 1983 the only GEV trigger element in use was the HMT with the requirement of a track in either top or bottom of the guillotine.

5.2.4 - The Dead Time Gating

The dead time logic (Fig. 5.4) provided the control of the various elements of the trigger. It prevented another event coming along while the later levels of the trigger were still processing the previous event.

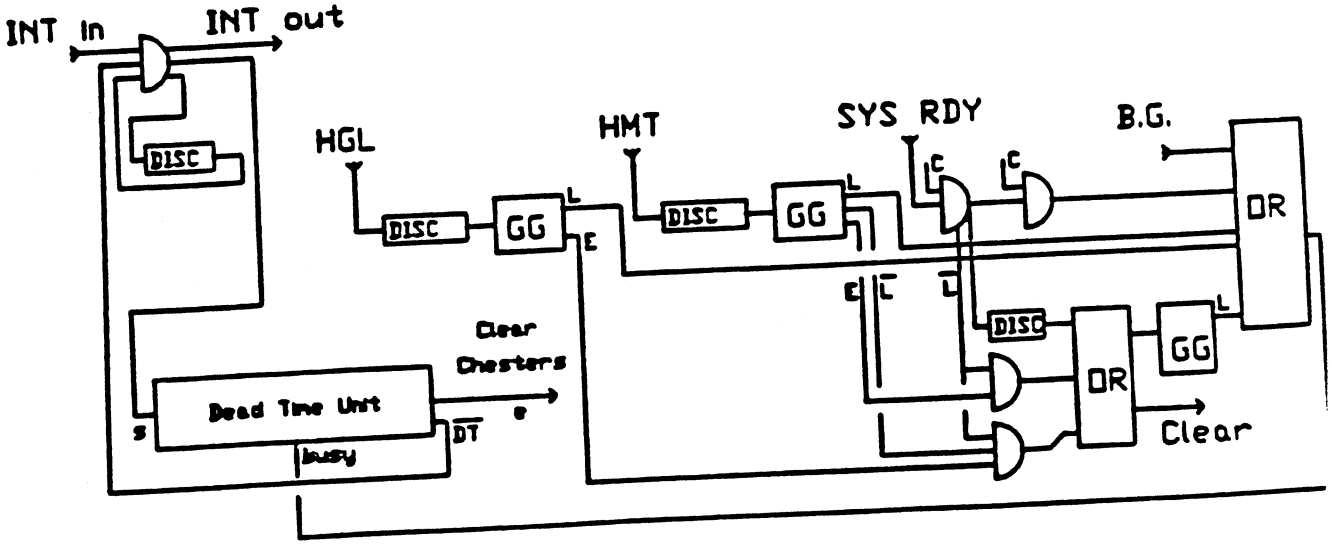

Fig. 5.4 The Dead Time Logic

At the first level of the trigger, the interaction trigger, no dead-time control was introduced. This was because at this stage no signals were latched and so no dead time was needed while the latches were cleared. At the HGL the signals from the guillotine hodoscopes were latched into the CHESTER's. Hence, following an event no subsequent events could be allowed through until the CHESTER's had been cleared regardless of whether or not the event was accepted. Following an HGL trigger the data from the whole event was latched into CAMAC read out modules. Again, as with the CHESTER's, the dead time logic had to prevent subsequent events before the read out modules had been cleared.

To control events reaching the second state of the trigger the interaction trigger was gated with the inverted dead time signal ($\overline{DT}$). Assuming the dead-time was OFF an interaction trigger could pass through to the HGL trigger logic and prevent subsequent events. This signal also started the dead-time cycle. After a time delay of 500 ns the dead-time unit would time out, clear the CHESTER's and open the dead-time gate; unless the dead-time unit was held ON by the event satisfying the HGL trigger. Following an HGL trigger the dead-time was held on a further 300 ns while the HMT formed. If after this delay, no HMT was formed the read out system was cleared then 2·8 μs later, allowing time for the read out ADC's to settle, the CHESTER's and HPC were cleared and the dead-time gate opened. If the HMT was satisfied the dead-time was held on a further 2 μs to allow the GEV to be formed. If after the 2 μs delay no GEV was formed the whole system was cleared as before, otherwise the GEV trigger was sent to interrupt the DAC. If the DAC

received and accepted the GEV interrupt it responded by removing the SYS-READY signal until the reading of the event into the DAC was complete. Following the re-assertion of SYS-READY (or if SYS-READY was never removed) the dead-time system cleared the read out modules, the CHESTERS and HPC in the usual way and finally opened the dead-time gate for the next event.

An effective spill gate was added to the dead-time system to prevent triggering the system outside the effective beam burst. At the beginning and end of the effective beam burst interrupts were sent to the DAC signalling start-of-burst and end-of-burst (SOB and EOB). The real beam burst was extended for a few milliseconds after the real end-of-burst to allow calibration events to be recorded outside the real beam spill.

5.3 - The Data Acquisition System

The data acquisition system was built around a VAX 11/780 computer. The primary use of this computer was to read in the data from each event and write it on to 6250 bpi magnetic tape. A secondary use was to run programs to monitor and control the experiment.

The link between the VAX and the experiment was via a CAMAC system (Ref. 5-4). The CAMAC system (Fig. 5.5) consisted of a system CAMAC crate connected directly to the VAX with a Fisher system crate interface (Ref. 5-3). Branch Couplers located in the system crate were used to drive branches of user CAMAC crates. These user CAMAC crates contained CAMAC modules to monitor and control the experiment. Computer links to the CERN central computer centre (via CERNET) and the EA div. Nord were also installed in the user CAMAC. In order to speed up and simplify the read out of the data for each event a special CAMAC system Romulus and Remus (Ref. 5-4) was used. In this system the crate controller of each special CAMAC crate was set up to sequentially read and clear all the read out modules in its crate. These crates were linked together to form a tree structure driven from a Branch Driver located in the system CAMAC crate. In conventional CAMAC each module has to be separately addressed and read in, where as with the Romulus/Remus system only the Branch Driver at the base of the tree has to be addressed and the whole event read in.

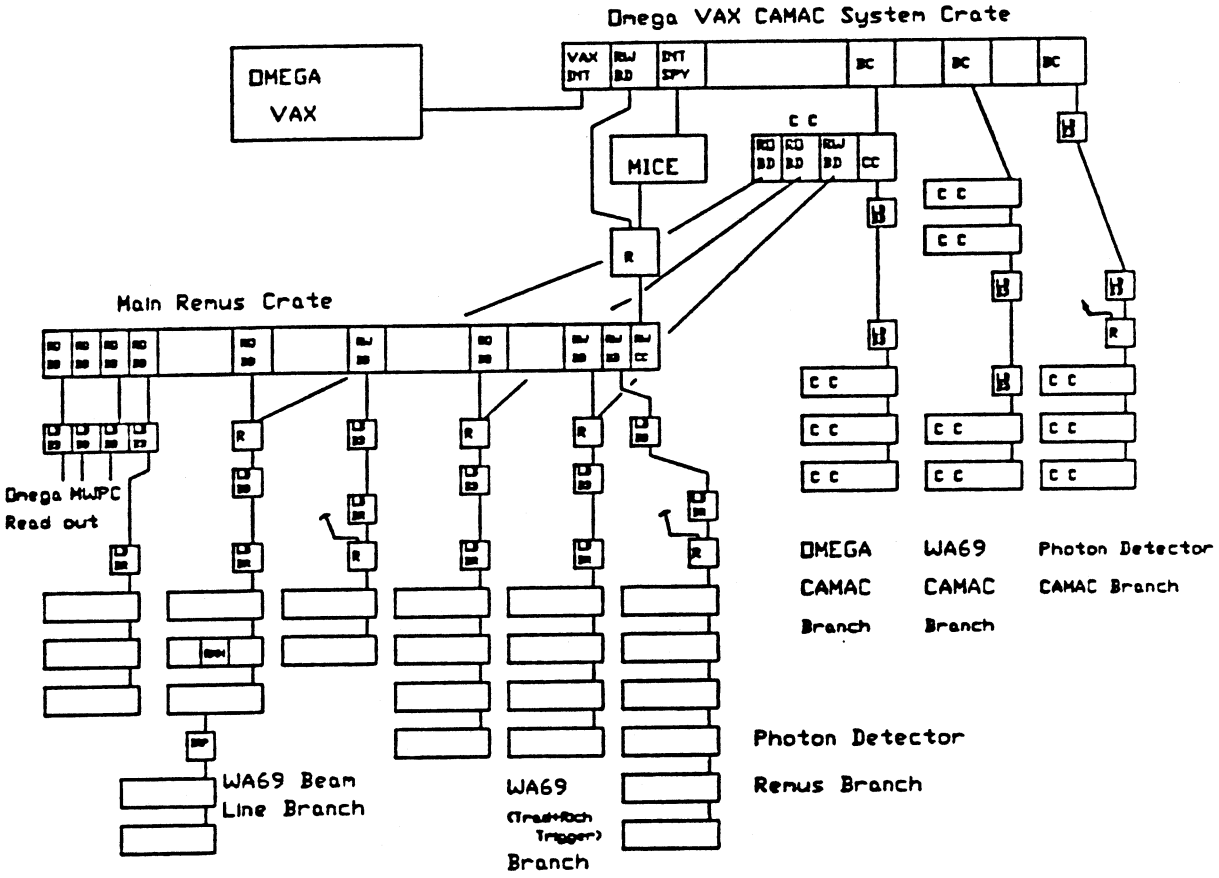

Fig. 5.5 The Camac and Data Acquisition System

After a GEV trigger an 'event' interrupt was sent to the VAX. Following the event interrupt the VAX had to stop whatever program it was executing, perform some checks on the type of interrupt, set up and execute the DMA transfer from the Romulus/Remus system. The time taken for the VAX to respond to the event interrupt was quite considerable ($\approx$ 1500 μs). This time together with the read out time ($\approx$ 1·5 μs/word) plus the inherent dead time of the trigger system ($\approx$ 5 μs) constituted the dead time of the data acquisition system. To reduce the dead time caused by the interrupt response time

of the VAX a MICE computer (Ref. 5-4) was used. Using the MICE, the main branch of the Romulus/Remus system was diverted from the Branch Driver in the system crate to the MICE (Fig. 5.6), and the event interrupt sent to the MICE. Following an event interrupt the MICE responded and read in the event. The response time of the MICE was much shorter than the VAX ($\approx$ 40 μs). The MICE buffered events and transferred them to the VAX as super events (containing more than one real event) in its own time without adding to the data acquisition dead time.

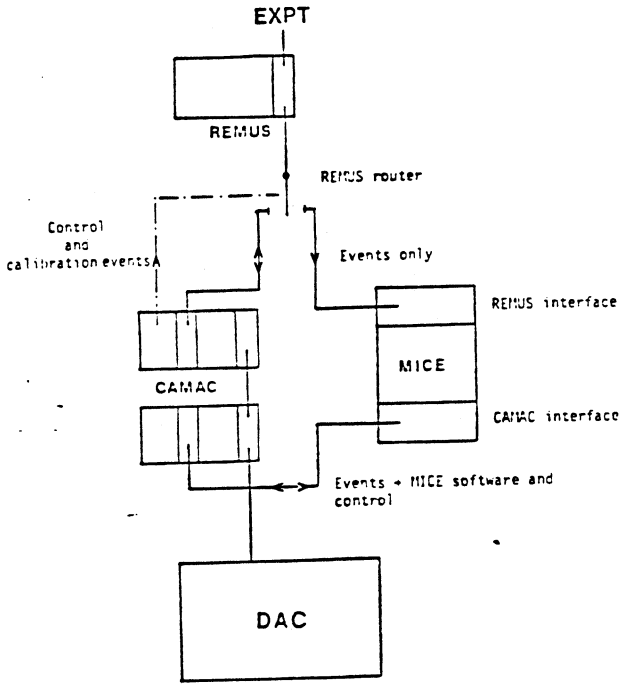

Fig. 5.6 The MICE

During the data taking the trigger and control logic sent two other interrupts to the VAX (bypassing the MICE). These corresponded to the start and end of the effective burst (SOB and EOB). Following the SOB interrupt the VAX recorded calibration data and set-up data on to the tape, and following the EOB interrupt the end of burst scalers were read in. The end of burst scalers were used to monitor

the rates in the different parts of the trigger and for normalisation of cross-sections in the final data analysis.

The data acquisition function inside the VAX was carried out by the process DAQP and the CAMAC driver (Ref. 5-5). The CAMAC driver was loaded with a set of instructions (the CAMAC list) describing how to read in the data from the event. This list contained three separate parts to be executed on the three different types of interrupt (EOB, SOB, and 'event'), the event part had to be able to handle events directly from the Romulus/Remus system and super events from the MICE. After the CAMAC driver had read in the data it passed control over to the DAQP process. The DAQP process controlled the buffering of the data and controlled the writing of the data out to magnetic tape. DAQP also performed the necessary book-keeping operations for events, such as the recording of the time, date, run, and event numbers on to the tape for each event.

5.4 - Online Monitoring and Control

The VAX as mentioned earlier was also used to run monitoring and control programs. These programs were run from a program PILOT (Ref. 5-5). PILOT provided a menu of all available monitoring and control programs and controlled the scheduling of the these programs. Having selected one program from the PILOT menu, communication with the program was via a system of menu's. This made monitoring programs quick and easy to use. Within a monitoring program the user had the ability to access the CAMAC system, to control the data taking by communication with DAQP, and request events from the DAQP buffers.

The most important control programs used were :-

RUN CONTROL which was used to set up and control the data taking and the tape writing in the DAQP process.

TRIGGER in which the required trigger combination and required minority triggers were set up and loaded into CAMAC registers to set the control levels in the trigger logic.

EHT controlled the voltage on most of the photomultiplier tubes in the experiment. It allowed the user to set the voltages on particular slats of a detector without having to know just where the EHT power supply was located and how to drive it.

Monitoring programs, which select events and process them fell into two categories. Some selected events one by one and displayed them in pictorial form. The others sampled events continuously producing histograms integrated over many events (A histogram Presenter was also provided running under PILOT, Ref. 5-6). Some of the more important monitor programs were:-

DACMON which sampled individual events and gave a numerical dump for part (or all) of the event record. This was useful in the testing and setting up the read out system.

PLUTO provided monitoring of the beam line and tagging system. It filled histograms of the hit distributions in the MWPC's and hodoscopes. It also produced phase space plots for the three regions in the beam line and calculated efficiencies for the wires and slats in the beam MWPC's and hodoscopes. Pluto also provided monitoring of the Tag and HGL counters.

ABCMAP69 provided hit distributions in the Omega wire chambers and drift chambers as well as the M4 chamber in front of the Photon Detector.

EVDI69 provided pictures of the hits in various detectors for single events. This gave a good representation of the appearance of the events in space and was also useful for estimation of the efficiency of the trigger by counting different classes of events.

SCALERS used the end-of-burst scalers accumulated over a few bursts to measure rates in the various parts of the trigger.

Other monitors were available and under development to monitor the RICH, the photon detector, the TRAD, the vetos and many other aspects of the experiment.

5.5 - Trigger Performance

For most of the data taken and presented in this report, the trigger used was the 'Doubles' at the HGL level and matrix coincidence in the top or bottom of the guillotines at the GEV level. Some data was taken with the other combinations of triggers to assess their performance at suppressing pairs and selection of particular physics channels.

Short non tape-writing runs were made with all combinations of tagging system vetos and the different tagging target thicknesses. During these runs the end-of-burst scalers were accumulated. Figure 5.7 shows the rates at various stages in the trigger as a function of tagging target thickness (in % radiation lengths) with various

combinations of vetos. Only a few combinations with thick tagging targets and a few vetos had to be omitted due to rate limitations in the DAC. As seen in chapter 2 the Quick Tag rate and Tag rate were proportional to the tagging target thickness with residual 5% and 3% of a radiation length in the tagging target region respectively. The hard photon content of the tag signal is born out in the Tag.BV rate which is ≈ 80% of the Tag rate and constant with tagging target thickness. The Interaction rate (Fig. 5.7a) shows that the inclusion of the veto S2V2 has more effect on the rate than it does in the Tag rate (Fig. 2.10). There is also some evidence for double bremsstrahlung since the interaction rate with the 15% target is greater than would be expected by linear extrapolation of the other three points. The lines on the rate plots are linear fits to the data. The HGL rate (Fig. 5.7b) shows that the effects of double bremsstrahlung have been removed by the beam veto and that the veto S2V2 has a yet more significant effect. The effect of S2V2 becomes more dramatic in the GEV (= HMT) rate plot (Fig. 5.7c). This dramatic effect on the rates in the higher parts of the trigger can be attributed to soft beam halo firing all the trigger counters. The radiation veto, holey vetos, and the beam veto do not fire because they require a significant amount of energy to be deposited but the veto S2V2 will fire and remove such events from the trigger.

Taking into account the false firings of the Quick Tag, Tag and Interaction triggers which show as residual material in the tagging region, the ratio of interaction triggers to tags was found to be about 0·06 (cf the radiation length of the liquid hydrogen target is 0.067). The ratio of 'hadronic events' (GEV) to interaction triggers was ≈ 0·017, which is about 3 times greater than the

ratio of the hadronic cross section to electromagnetic cross section (≈ 0·006). From this we conclude that 2/3's of the data written to tape will be electromagnetic pairs and not hadronic.

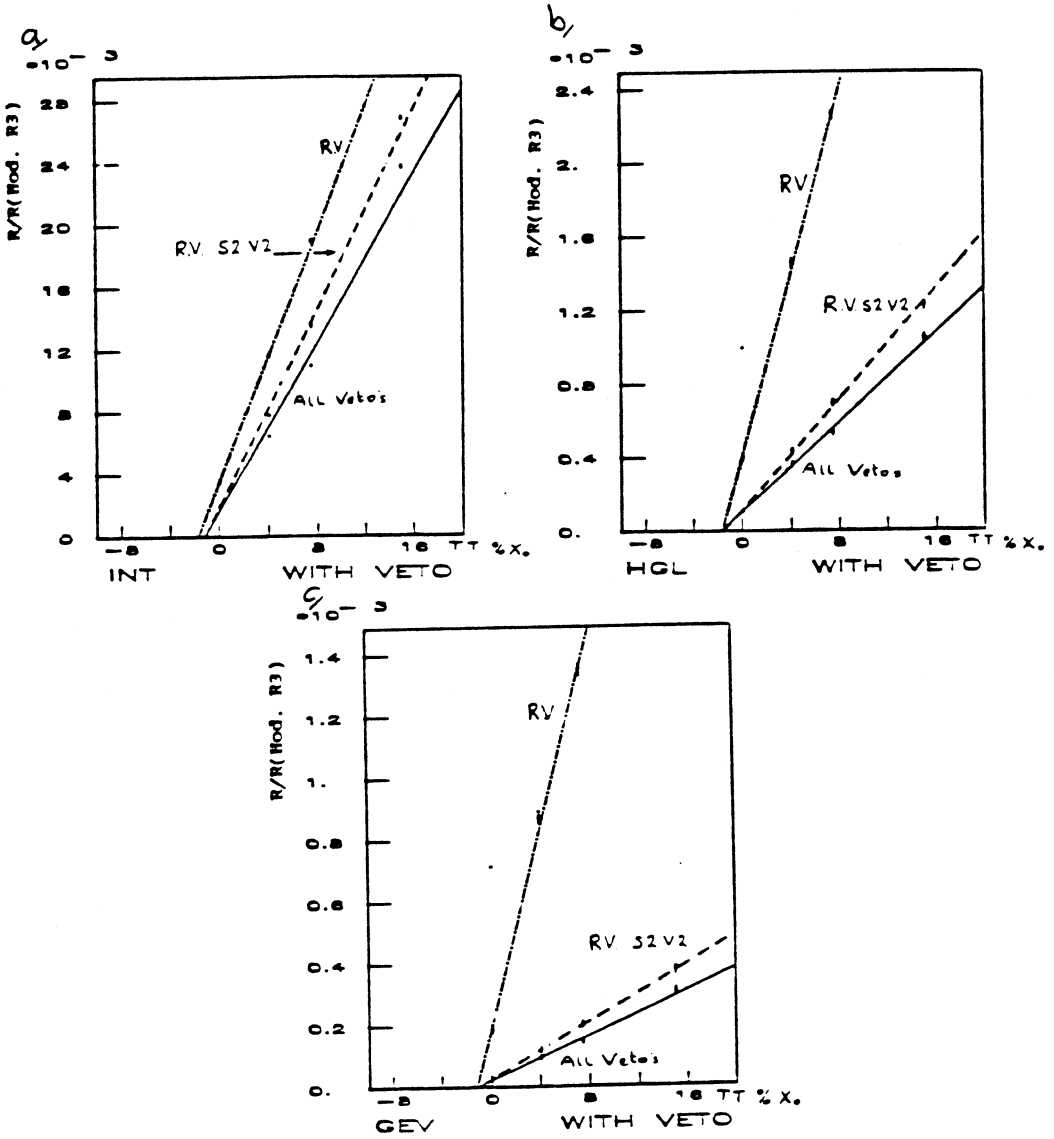

Fig. 5.7 Trigger Rates against Tagging Target Thickness

The plot of fractional live time against trigger rate (Fig. 5.8) shows the fraction decreasing with increased rate. The curve is

consistent with figures in section 5.2.4 with a typical event length of ≈ 1200 words of data per event.

Fig. 5.8 Fractional Live Time against Trigger Rate

5.6 - References

5-1 MBNIN User Guide

F. Bourgeois CERN EF Aug 1980, Edition 1

5-2 CAMAC A Modular Instrumentation System

for Data Handling

Euratom Report EUR4100e (March 1969)

5-3 A Guide to Romulus/Remus Data Acquisition Systems

P. J. Poting CERN EP-Electronics Note 80-01 Feb. 1980

5-4 Future Event Buffering, On-line Filtering

and Data Acquisition for Omega

F. Bourgeois CERN OM/SPS/81-12 Nov 1981

5-5 UA2 VAX On-line Data Acquisition Manual

CERN DD

5-7 PRESENTER Histogram Presenter for VAX

J. P. Dufey CERN DD/EE/82-1 Sept 1982 Version 5.00

5.7 - Figure Captions

5.1 Block Diagram of the Trigger

5.2 The Hadron Guillotine Trigger

5.3 The Good Event Trigger

5.4 The Dead Time Logic

5.5 The Camac and Data Acquisition System

5.6 The MICE

5.7 Trigger Rates against Tagging Target Thickness

5.8 Fractional Live Time against Trigger Rate

CHAPTER VI

DATA PROCESSING

Chapter VI

6 - Data Processing

6.1 - Introduction

In the preliminary data taking period in December 1983, the experiment WA69 recorded 24 raw data tapes containing about 1,000,000 events. This data was taken under 'standard' conditions, that is with a 4·2% X_0 tagging target, the liquid hydrogen target full, Omega magnetic field on, and with a 'doubles' and matrix trigger. A further 10 tapes were written containing data under 'non-standard' conditions. This data was taken to test and calibrate the experiment's hardware and software. These 'non-standard' runs included a low energy, low rate proton beam run to test the RICH; runs with the Omega field off were made to determine the chamber alignment coefficients; runs with different tagging target thicknesses and different triggers were also taken to assess the problems associated with double bremsstrahlung and trigger efficiency.

Off-line monitor programs were run on the raw data, to complement their on-line counter-parts by making more detailed calculations on the data to determine chamber efficiencies accurately. They were designed study sections of the experiment as a whole rather than just individual planes in detectors. The off-line monitors also provided higher statistics than the on-line monitors since they were run on large samples of data from the data tapes.

The data processing stage was preceded by a series of standard data reduction programs. These programs converted the raw data in the form of chamber hits, ADC pulse heights and TDC times into particle tracks with 4-vector momenta and mass assignments, together with topographical information and vertex locations for each event. The production analysis DST's (Data Summary Tapes) were then written containing only the data necessary for final analysis. Physics analysis programs were then run on the DST's to extract 'physics' from the data.

6.2 - Off-line Monitoring

Off-line monitor programs were written for the four main areas of the experiment: the beam line and trigger, the Omega chambers, the RICH and the photon detector.

GDLCHECK (Ref. 6-1) provided the off-line monitoring for the beam line and trigger. It provided hit and multiplicity distributions for the beam and tagging system chambers and scintillation counter hodoscopes, monitoring of the tagging system and trigger counters together with the rates and correlations in the trigger logic and monitoring of the veto counter ADC pulse height spectrums. A curtain amount of checking was also performed on the end-of-burst scalers.

HPJCHECK (Ref. 6-2) provided the off-line monitoring for the Omega chambers. This included hit, multiplicity and drift time (in the case of the drift chambers) for the Omega chambers and the M4 chamber in front of the Photon Detector. This monitor also performed checks on the romulus system to make sure every crate was read out every event and to monitor the numbers of words read out per crate.

Off-line monitors for the RICH and the Photon Detector will not be discussed further as the detectors were still under development and data from them is not used in the analysis presented here.

6.3 - Data Processing

Before the final analysis of the data could take place two standard data reduction programs had to be run and DST's produced. The first of these programs, TRIDENT (Ref. 6-3) used the information from the Omega chambers on the raw data tapes to find the tracks due to charged particles and measure their momenta. Using the trajectories of these charged tracks TRIDENT then found the event topology and calculated the vertex locations. The results from the TRIDENT analysis were then written to the TRIDENT output tapes. The second data reduction program, PEDRO (Ref. 6-4) used the data from the beam line and tagging system detectors to calculate the energy of the incident photon. PEDRO was run within a program which could read TRIDENT output tapes and produce DST's. This same program was used to read back the DST's and perform analysis on the data.

In the production analysis of the bulk of the Eγ data it is intended to run PEDRO within TRIDENT at the track finding stage. The TRIDENT vertex finding routines will then be able to make use of the projected photon beam to improve the precision of the main vertex. TRIDENT will then produce track banks, topology banks, and the unused raw data on the output tapes. The program PHOENIX (Ref. 6-5) will then read the TRIDENT output tapes and pass the data on to the RICH, TRAD, and Photon Detector packages. The RICH package will extrapolate

the tracks found by TRIDENT through the RICH to predict the centres of possible rings. Using the momenta of the tracks given by TRIDENT and their possible mass assignments (e, μ, π, K, and P) the radii of potential rings can be predicted. From the numbers of hits found within given annuli about these rings a statistical probability for a given mass assignment to each track is made. Similarly, in the TRAD package, TRIDENT tracks are extrapolated through the TRAD. From the hit distribution and energy deposition in the TRAD MWPC's in the area of the projected tracks, the particle identification is made. The Photon Detector package first locates the position and energy deposition of the tracks entering it from the pulse height and the time-of-flight information. Hits due to charged tracks (e and hadrons) are masked off using the M4 MWPC in front of the photon detector and extrapolated TRIDENT tracks. The 4-vector momenta of the remaining photons are then calculated using the energy deposition, the hit position in the photon detector and the main vertex location in Omega. Combinations of photons pairs are then made to look for decay of π^0's and η's. PHOENIX then collects the data from each package and packs it into a form for writing DST's containing track vectors and particle mass assignments, possible decay topologies, vertex locations and beam information.

6.3.1 - TRIDENT

TRIDENT (TRack IDENTification in Omega) provided the pattern recognition for charged tracks in Omega. TRIDENT used the data from the Drift Chambers and the 3 sets of MWPC's in Omega from the raw data or simulated chamber digitisings produced by the Monte-Carlo program GEANT (Ref. 6-6). For each track the relevant digitisings

were located and from them, the momentum and trajectory calculated. After the track finding TRIDENT traced the tracks back into the hydrogen target to locate the primary and any secondary vertices (V^0's).

The track finding part of TRIDENT first considered the two Drift Chambers at the back of Omega. Hits in these chambers were joined to find tracks compatible with them having originated from the target. The potential tracks were then projected back into the Omega MWPC's using a cubic spline fit in the XY projection and a straight line in the XZ projection. As the extrapolation worked back digitisings were associated with the track if they were within a given error distance from it. The new hits as they were found were used to improve the extrapolation accuracy. The remaining digitisings were used to reconstruct the lower energy track (which do not reach the Drift Chambers) in a similar way. The momentum and trajectory of each track was then calculated from the associated hits and the full Omega field map using a quintic spline fit. Trident calculated the inverse momentum ($1/P \times SIGN(charge)$), dip angle (λ), and azimuthal angle (φ), together with a full error matrix at both the first and last measured point on each track.

Following the track finding, TRIDENT determined the interaction vertex and secondary vertices (V^0). This was done by taking pairs of tracks in turn and extrapolating them back from the first measured point as a helix. Pairs which intersected (within errors) were clustered into 2-prong vertices. The 2-prong vertices were then merged together with any remaining un-clustered tracks if they coincided within errors due to the track fit and extrapolation. The

resultant vertex was then fitted using the track parameters of the clustered tracks at the first measured point and the full magnetic field map. If the resultant χ^2 was too large, the worst fitting tracks were removed one by one and the vertex refitted until the χ^2 was satisfactory. The remaining 2-prong vertices were checked to be consistent with K^0, $\bar{K}^0$, Λ^0, $\bar{\Lambda}^0$, or γ ($\rightarrow e^+e^-$) and a V^0 fitted using the extrapolated track as the main vertex. For each track originating from the main vertex (and similarly for V^0) TRIDENT recalculated the track parameters and error matrix at the vertex. If there was an ambiguous solution to the vertex finding TRIDENT output two alternative 'topologies' for the event. The first topology represented the case where most tracks were in the main vertex, and the second with fewer tracks in the main vertex and more V^0's. Any remaining track not fitted to either the main vertex or a V^0 were output as 'extra tracks'.

A selection filter was added to TRIDENT to reduce the electromagnetic pairs contamination. This filter required more than 52 hits in the Omega 'A' chambers for an event to be acceptable. The maximum number of hits a 2-prong event could produce was 42, so the filter had the effect of cutting out not only pairs but also elastic ρ, ω and ϕ photoproduction which decay to $\pi^+\pi^-(n\pi^0)$. An upper limit of 400 hits in the 'A' chambers was also imposed to remove events with large showers in Omega.

6.3.2 - PEDRO

PEDRO (Photon Energy and Direction from Reconstructed Orbits) provided the beam line fitting, recoil electron fitting and calculation of the photon entering Omega. PEDRO read in data from the beam line and tagging system from either the raw data, the TRIDENT output data, or in its own simulation mode, Monte-Carlo generated data.

The beam line part of PEDRO used the hodoscopes to draw 'roads' through the 8 planes of MWPC's in each region. Only MWPC hits within these roads were selected so reducing the chance of 'seeing' other beam tracks close in time to the real track. In cases when a hodoscope plane had no hits, rescue routines were used to identify compatible hits in the MWPC's using check-sums performed between combinations of hits in the region. Before a fit was made, checks on the number of hits found were performed to make sure the data was suitable to be fitted. These checks required at least two hits in non-parallel planes together with one more hit in each region and at least one more hit in the whole beam line. A quintic least squares fit was made to the selected MWPC hits to calculate Y, Y', Z, Z', and P at the tagging target, using the transport matrices for the magnets between the three regions. If a fit could not be performed, nominal values for the beam momentum and trajectory at the tagging target were used with correspondingly larger errors.

In region 4 the hits in the tag hodoscopes H4.1, H4.2, and the lead glass were combined to form a 'road' in region 4 and from the position of the road an estimate of the recoil electron momentum was

made. Hits in the five MWPC's were selected if they lay within the road. A least squares fit using the magnetic field map of the tagging magnets and the position of the beam track in the tagging target was used to calculate P and Y' of the recoil electron.

Finally, PEDRO combined the beam line fit and the recoil electron fit to calculate the momentum of the tagged photon. The projection of the photon into the Omega target was calculated in Omega co-ordinates.

6.3.3 - The Simulation and MAP

There were two simulation programs that could be used to simulate different aspects of the experiment. GEANT (Ref. 6.6) could be used to produce simulated raw data to be processed by TRIDENT and the other analysis programs as if it was real data, or MAP (Manchester Acceptance Program; Ref. 6-7) could also be used to determine just trigger acceptances.

The full simulation using GEANT takes interactions generated with an event generator such as SAGE (Ref. 6-8) or LUND (Ref. 6-9), and tracks the particles from the hydrogen target through the Omega chambers and the downstream detectors. GEANT handles decay of long lived particles (K and Λ), pair production by photons, electromagnetic showering and the multiple scattering of the particles in the material of the detectors. Where the particles pass through detectors hits were generated taking into account efficiencies and clustering. Finally, the simulated hits are written out in a raw data format to be processed by TRIDENT. This sort of

simulation not only takes into account the geometric acceptances and efficiencies of the detectors but also the reconstruction and pattern recognition efficiences in the analysis programs. The main disadvantages was that a full GEANT simulation would take about 1 s per event and would be difficult to set up for a new detector configuration. Thus, for the simulations presented here GEANT was not used but instead the program MAP was used.

MAP started with simulated interactions in the same way as GEANT. The particles were tracked only through the detectors used in both the hardware and software triggers. From the intersections of the tracks and trigger detectors MAP generated a list of hits taking into account the chamber geometries and efficiencies. For each element in the trigger MAP calculated whether the trigger condition would be satisfied. Finally, MAP determined whether or not the event generated would have satisfied the full trigger condition. At the end of the simulation MAP produced a summary list of the acceptances for each of the trigger elements and the global acceptance.

The following trigger elements were set up in MAP;

i End-Cap - required at least one track to pass through it.

ii 'A' chamber multiplicity - required more than 52 and less than 400 hits in the Omega 'A' chambers to simulate the electromagnetic pairs filter used in TRIDENT. This trigger element took into account the medium plane inefficiencies in the Y planes and the clustering size due to the wire spacing.

iii H1 - required at least one hit somewhere in the detector.

iv H4 - as H1 required at least one hit.

v HMT - first simulated the hardware HGL logic using the hits in H1 and H4 found in the previous trigger sections. This part required the 'Doubles' condition, at least one hit in $H1_t$ and $H4_t$ or at least one hit in $H1_b$ and $H4_b$. The second part simulated the matrix coincidence logic used in the hardware HMT. A requirement that the matrix was satisfied in either top or bottom was imposed.

Following the acceptance of an event by MAP a certain amount of smearing was sometimes applied to each track to take into account reconstruction errors in TRIDENT. The removal of low energy, low P_t tracks could also be made, as in reality these tracks would never leave the hydrogen target.

6.3.4 - DST Writing, Reading and Analysis

A program was written to provide a framework within which analysis routines could be run. The program (Fig. 6.1) could read either TRIDENT output tapes, its own DST's or generate Monte-Carlo data using the SAGE routines. The data then passed through selection routines to select events on global features such as multiplicity, momentum balance or beam energy. The selected events then passed through an electromagnetic filter to reduce double pairs contamination in the 4-prong events. Following the filter the data either passed on to routines to plot histograms showing general features of the data, specific physics analysis routines or could be written on to DST's.

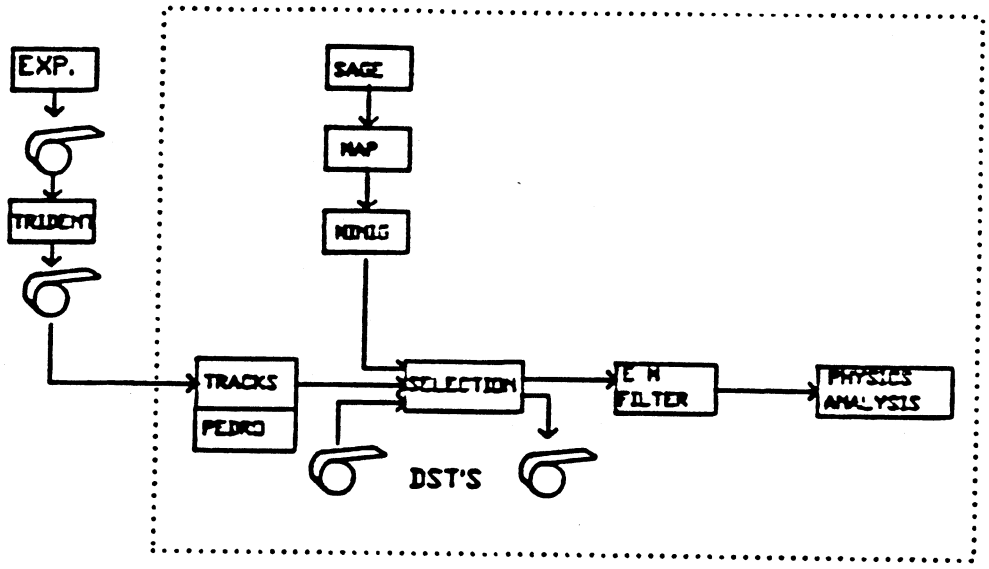

Fig. 6.1 Diagram of the Data Analysis Program

When running on TRIDENT output tapes directly to look at global features of the data a conversion routine was used to convert the TRIDENT geometry banks into a more useful format of both physics analysis and DST handling. A simple routine was used to estimate the beam energy (similar to the routine in PEDRO to calculate the region 4 roads). This routine used the residual raw data bank in the TRIDENT output.

When the program was used to write the DST's containing only data relevant for physics analysis the simple beam energy finding routine was replaced by PEDRO. No attempt was made to use the RICH or TRAD data for charged track identification because the detectors were

still in a development stage and their analysis programs were still being written. All tracks were assumed to be pions because of this restriction (with the possible exception of recoil protons identified kinematically). Since the Photon Detector analysis programs were still being developed, the DST's contained no photon or reconstructed π^0 data. For DST production the event selection and electromagnetic filter routines were turned off. At the end of each run (as defined by the data acquisition at data taking) an end-of-run block was written to tape. This block contained a summary of all the end-of-burst scalers accumulated over the run and also a summary of the numbers of events read in and processed. The end-of-burst scalers were preserved in this form on the DST's for normalisation purposes.

When the program was run, for either DST writing or data analysis, at the end of every run (as defined by the DAC) a summary table was written out. This table contained a summary of the numbers of events processed and some of the accumulated end-of-burst scalers. This summary was produced so that normalisation could take account of any slight changes in the data taking conditions from run to run.

To run a Monte-Carlo simulation the events were generated by SAGE routines rather than read in from tape. The events then passed through MAP to assess whether the trigger conditions would be satisfied (including the 'A' chamber multiplicity cut in TRIDENT). The events were then converted from the simulation bank format into the DST bank format and passed through the same sequence as the real data, selection on general features, electromagnetic double pairs reduction and physics analysis routines.

6.4 - General Features of the Data

The distribution of the numbers of charged tracks found by TRIDENT (Fig. 6.2a), showed, an abnormally large number of 4-prong events. This was probably due to double e^+e^- pairs from double bremsstrahlung in the tagging target. Data in the low multiplicity region has been reduced by the TRIDENT pairs filter and the effect of the trigger. At the upper end of the distribution the cut off was caused by an upper limit of 15 charged tracks in TRIDENT. The 'extra track' multiplicity plot (Fig. 6.2b) showed that TRIDENT failed to fit on average 2·9 tracks to any vertex. This leaves only 12% of the events completely reconstructed (ie with no extra tracks). The number of extra tracks was a measure of the TRIDENT vertex finding efficiency, because most of the extra tracks should have been fitted to a vertex. Some extra tracks came from TRIDENT fitting tracks through noise points and some from stray tracks due to the interaction of other beam particles. The distributions of numbers of vertices (Fig 6.2c and 6.2d) showed a mean of ·27 V^0's in the first topology and 1·02 V^0's in the second topology. About 13% of the events had an ambiguous geometry with two TRIDENT topology banks produced.

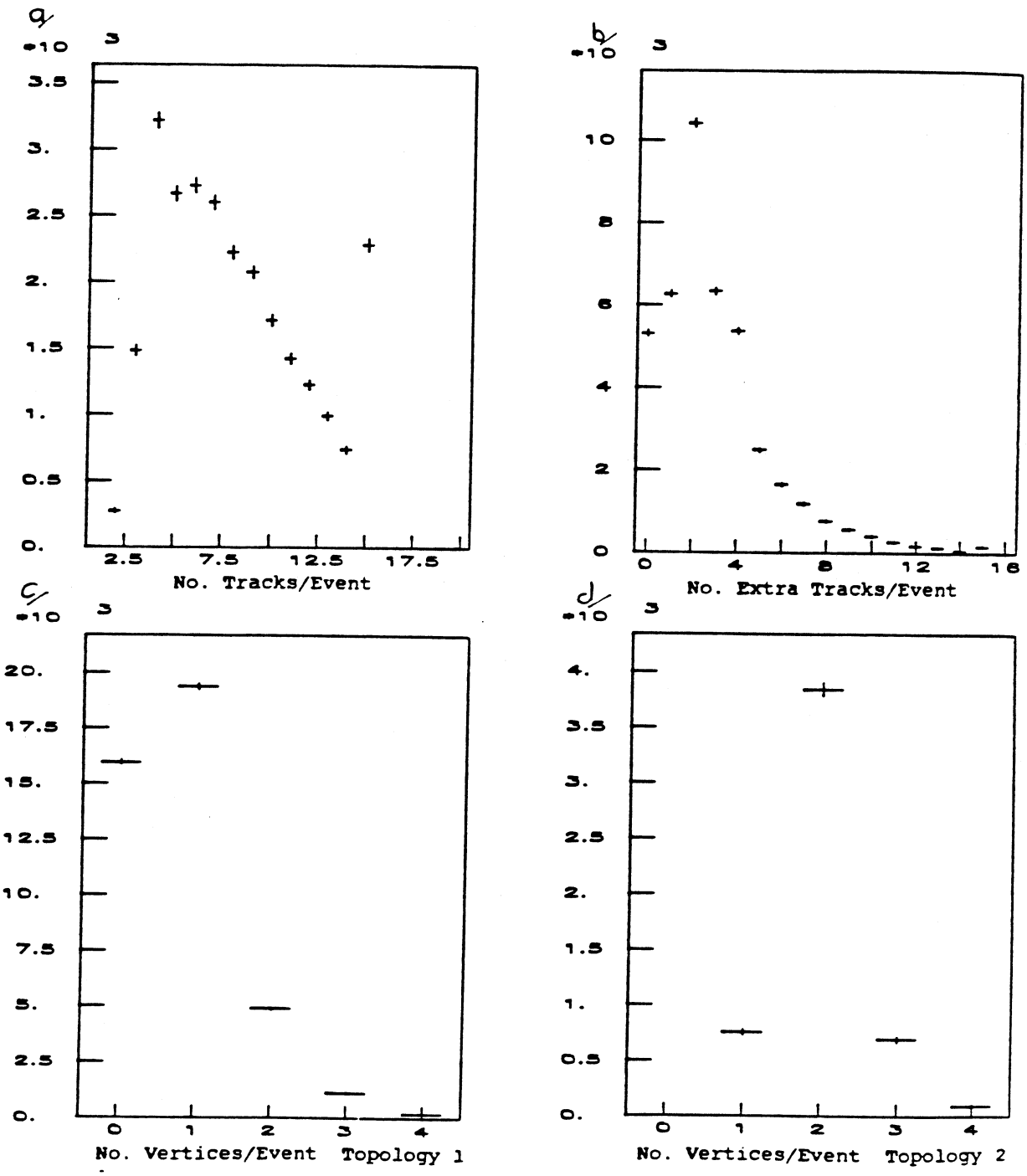

Fig. 6.2 Multiplicity Distributions and Numbers of Verticies

The main vertex location for events with no extra tracks (Fig. 6.3) showed that the bulk of the events came from interactions in the hydrogen target. The transverse plots show that there were some events where the incident photon interacted in the wall of the hydrogen target. The fraction of events with a well measured main vertex (and no extra tracks) was 10·7%

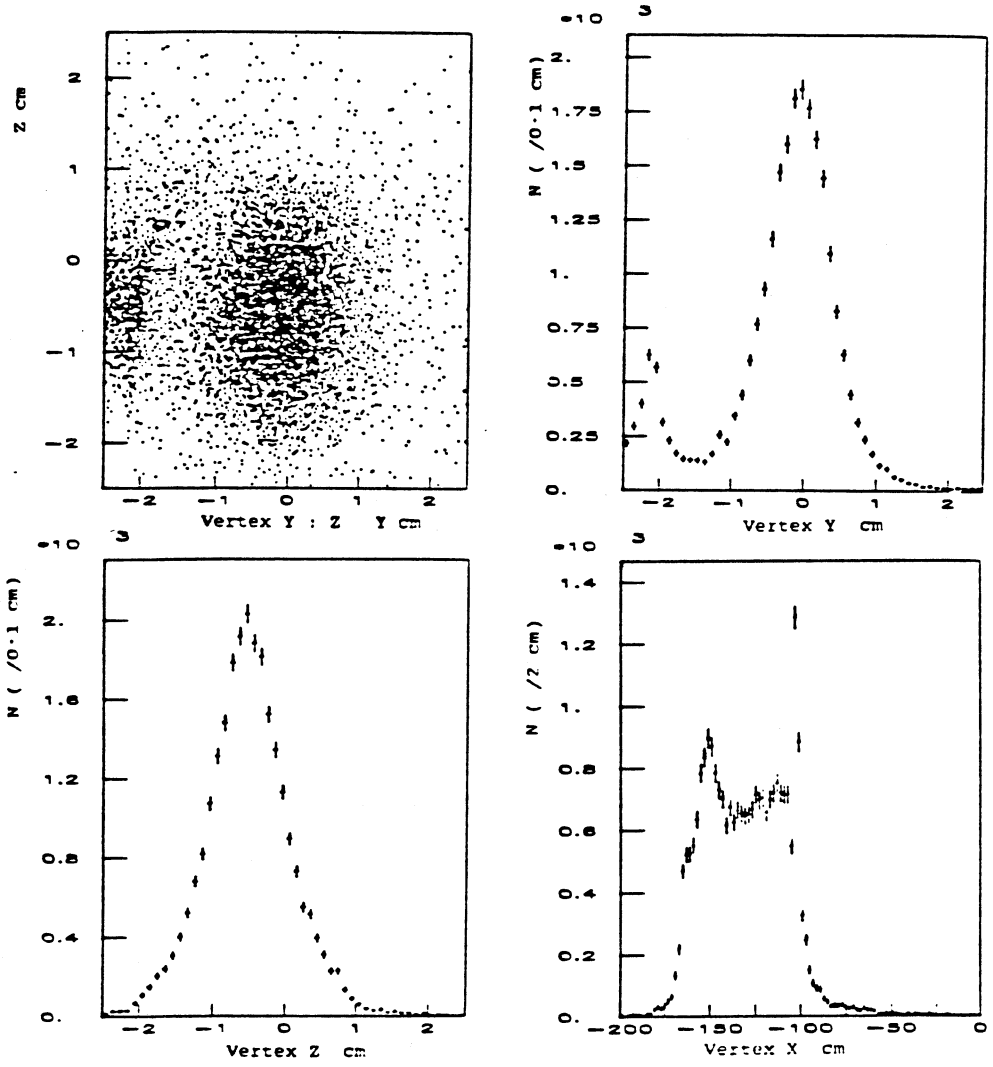

Fig. 6.3 Main Vertex Location

The momentum distributions (Fig. 6.4) showed a reasonable behaviour but the Dip Distribution (Dip = P_z/P_x) for the tracks (Fig. 6.5) showed a large narrow peak at zero on top of a broad distribution. This peak was found to be due to 4-prong events and is

consistent with being caused by double pair production. To remove this contamination in the 4-prong events the electromagnetic filter required these events to have at least two tracks with dip greater than 3 mr and two independent track pairs to have a dip difference greater than 5 mr. Following the double pairs filter the multiplicity and dip distributions (Fig. 6.6) looked more reasonable. This cut will bias the 4-prong hadronic events. When a corresponding cut is applied to the events with multiplicity 5 or more only a small fraction fail the cut. The biases due to the cut will have to be estimated by Monte-Carlo simulation.

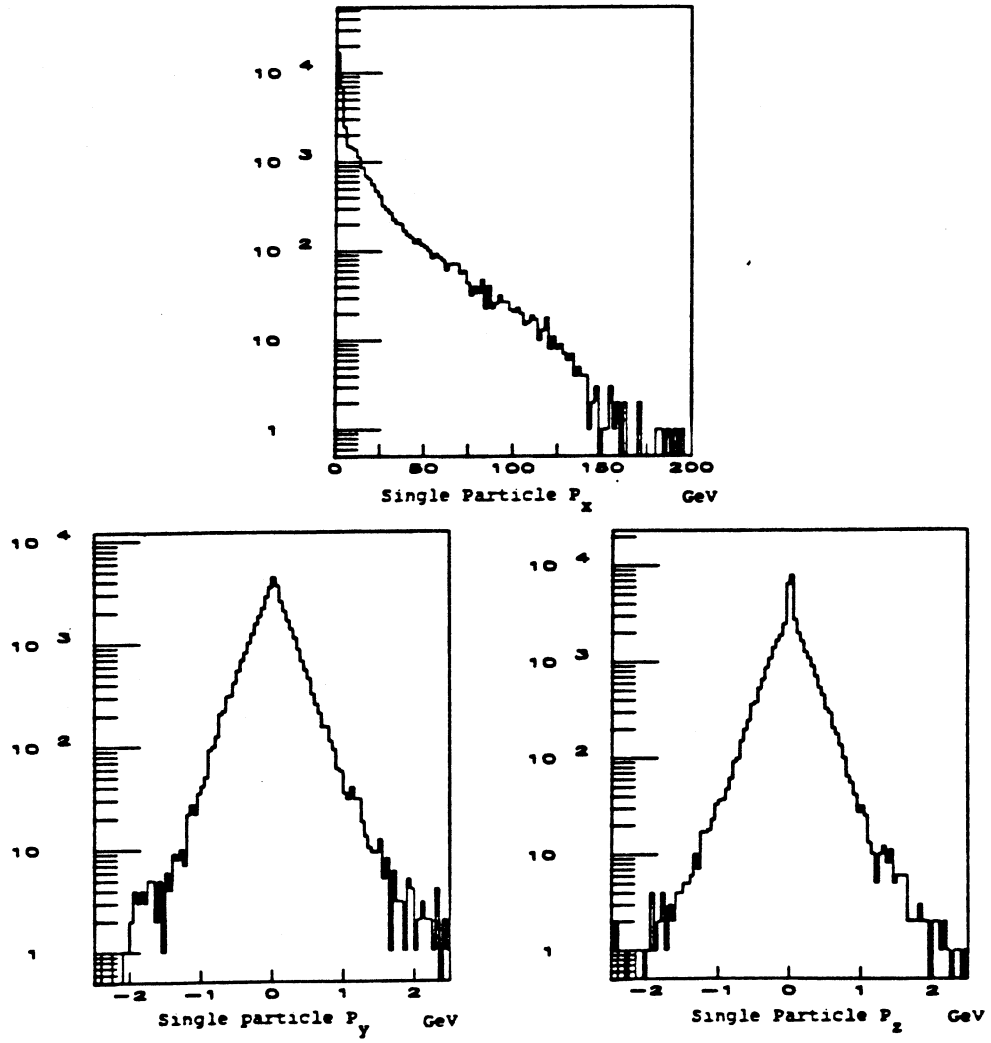

Fig. 6.4 Single particle Momentum Distributions

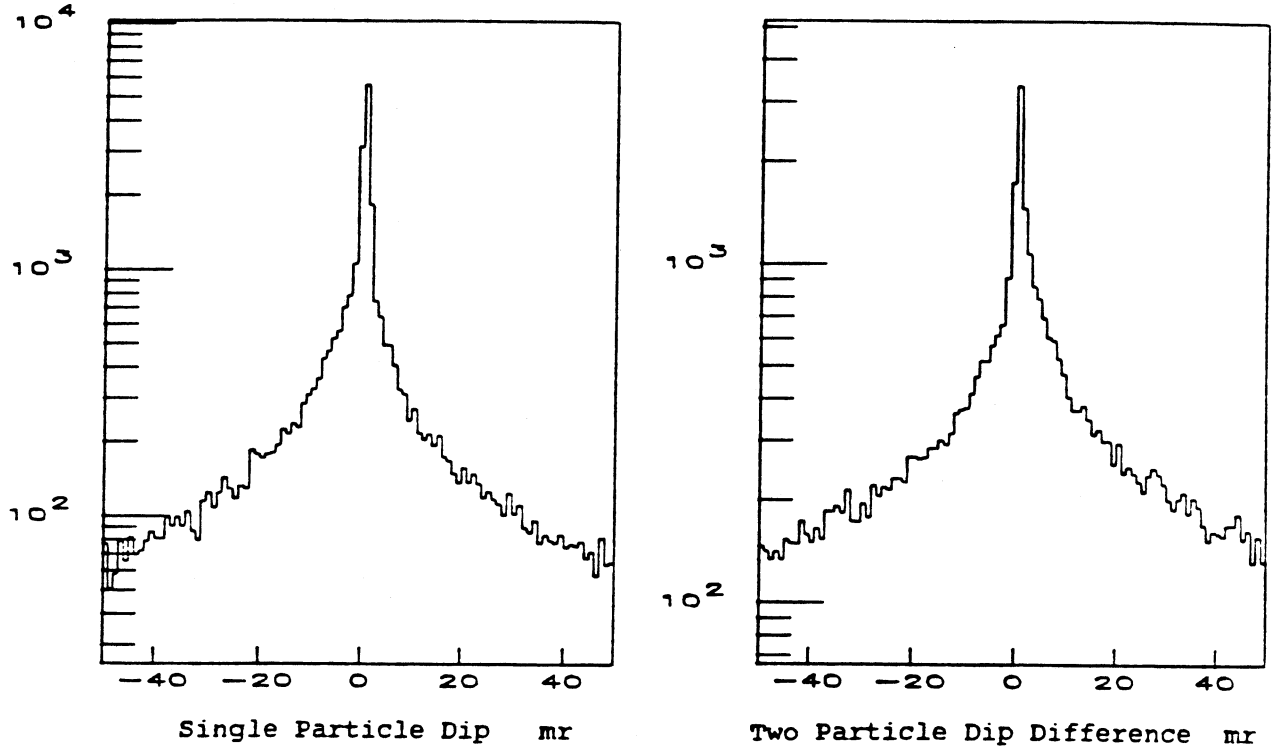

Fig. 6.5 Dip Distributions

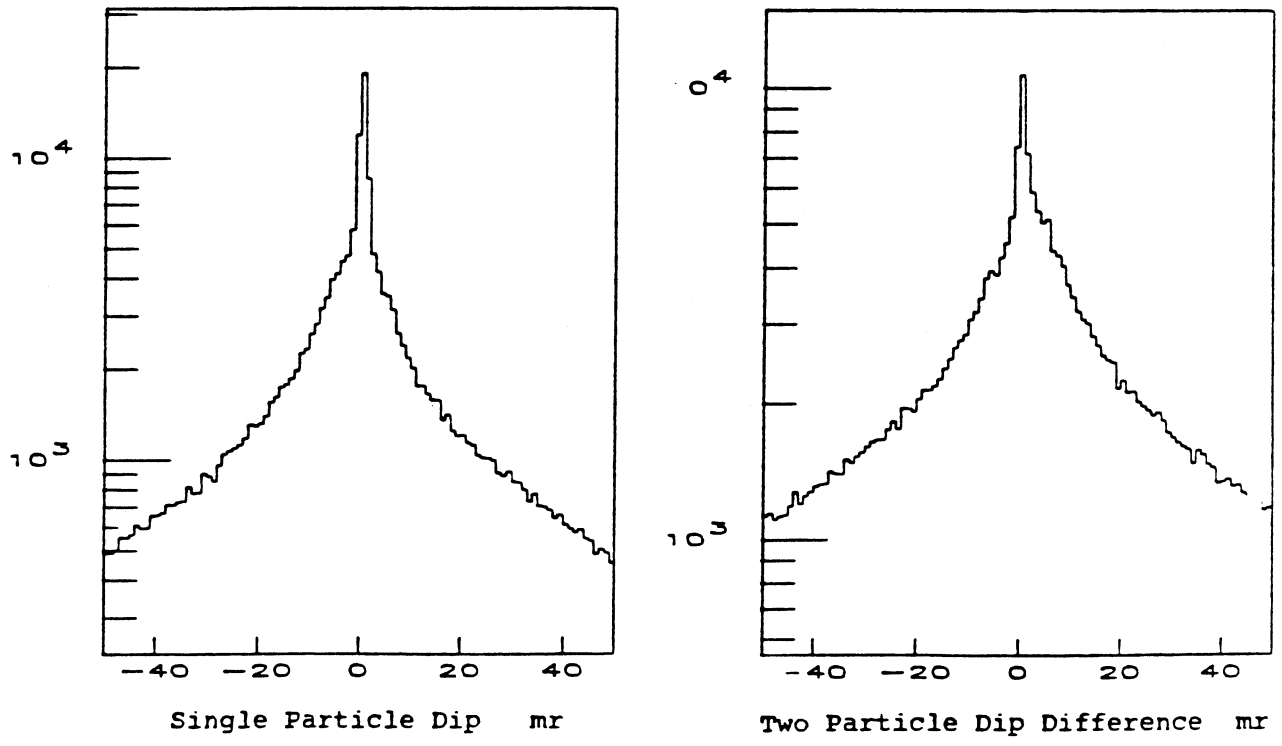

Fig. 6.6 Dip Distributions after EM Filter

The results from the beam fitting in PEDRO (Fig. 6.7) showed an Eγ spectrum similar to that found in the on-line monitor program PLUTO. The transverse beam location calculated at the centre of the target showed that the beam passes into the target with little hitting the walls or going outside the target. PEDRO calculated the beam energy with a mean error of about 0·31 GeV and mean errors of 0·68 mm and 0·34 mm on the y and z positions at the centre of the target.

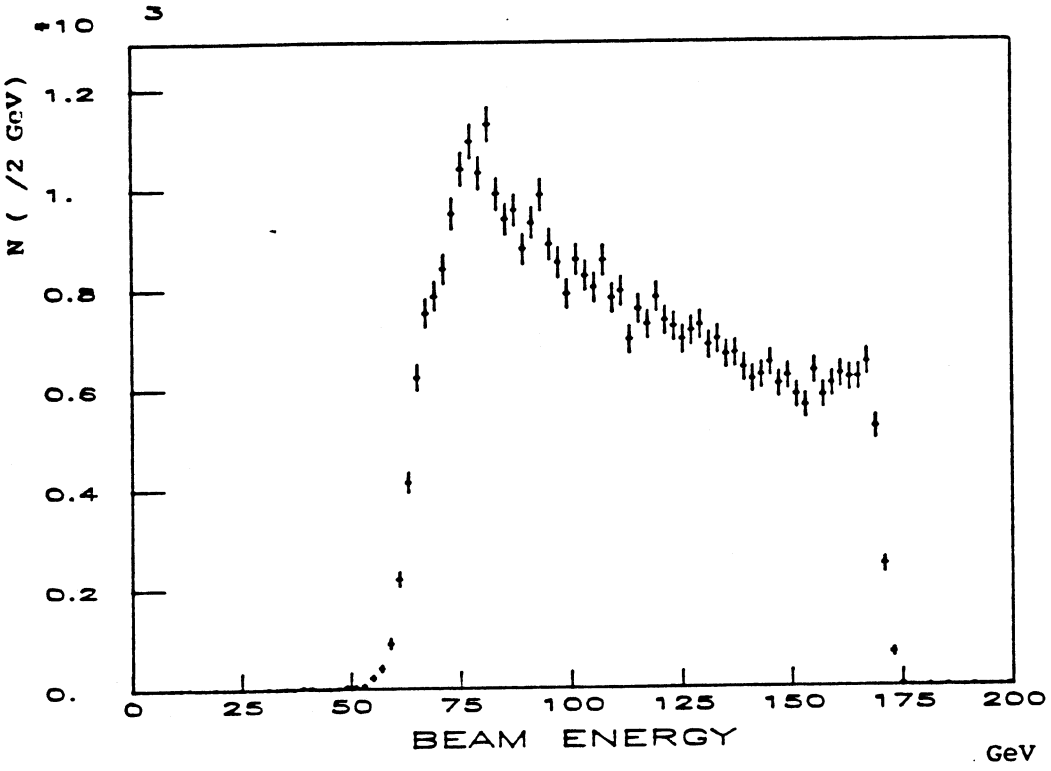

Fig. 6.7 The Photon Beam Energy Spectrum

Comparison of the PEDRO and TRIDENT results showed a good corrrelation between the position of the vertex as calculated by both programs (for the no-extra track events: not shown). The longitudinal momentum balance (PXDIFF = $P_x$beam - $\sum P_x$seen) for vertex tracks (Fig. 6.8) showed a narrow spike at zero with a broad distribution on the positive side. The spike was due to events where all the tracks were charged and seen (with the possible exception of low energy tracks from target fragmentation). The tail was due to events with neutral and possible unseen charged tracks. When the extra tracks were included in the PxDiff plot (Fig. 6.9) the spike got larger and broader and the tail slightly smaller. This showed that a large fraction of the extra tracks were good tracks which TRIDENT had failed to fit to a vertex. A similar effect occured with the transverse momentum differences where one observes a narrow spike sat upon a broad symmetrical distribution centred on zero.

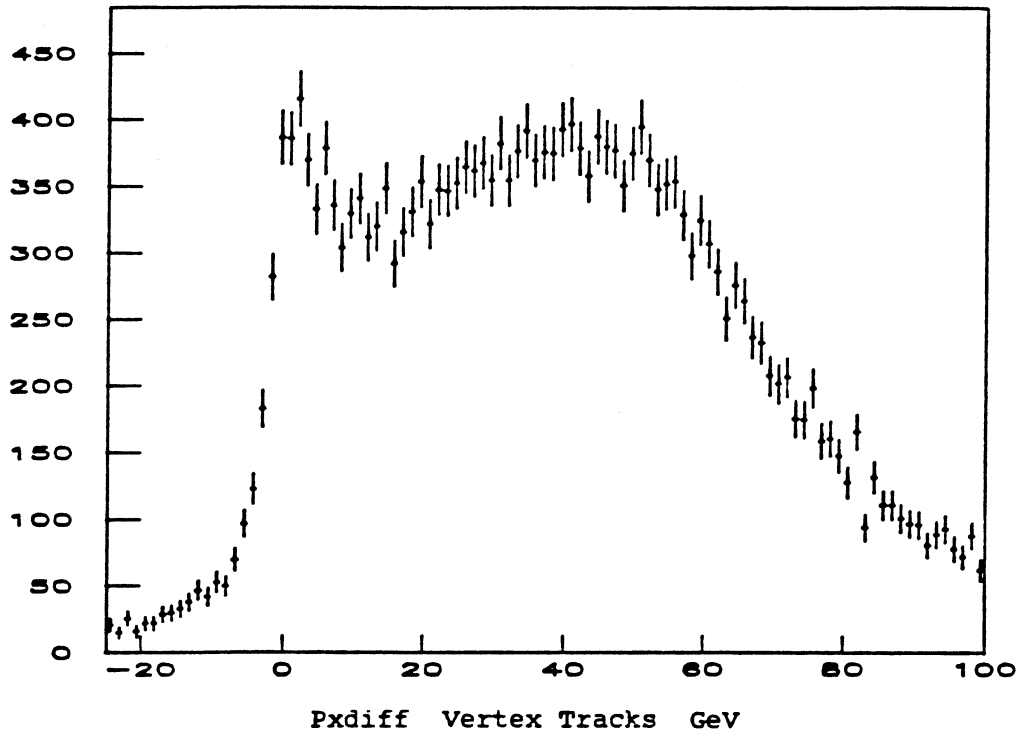

Fig. 6.8 Longitudinal Momentum Balance Excluding Extra Tracks

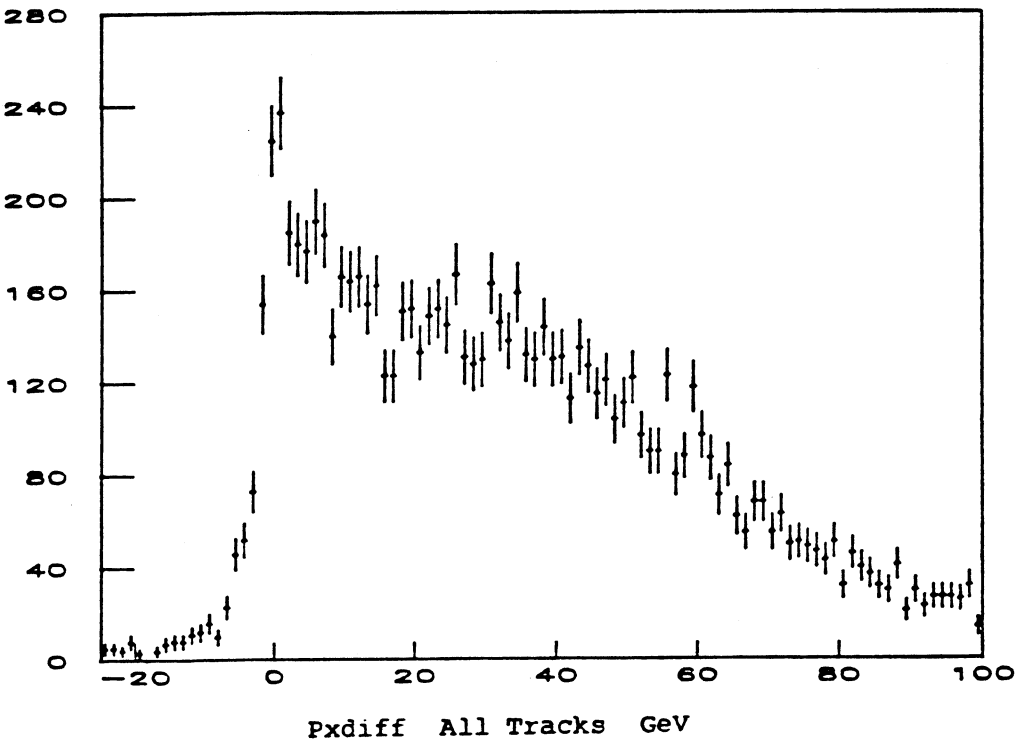

Fig. 6.9 Longitudinal Momentum Balance Including Extra Tracks

6.5 - References

6-1 GDLCHECK

Private communication with G. D. Lafferty

6-2 HPJCHECK

Private communication with G. D. Lafferty

6-3 TRIDENT Track and Vertex Identification Program f

for the Omega Particle Detector System

J-C. Lassalle et al CERN DD/EE/79-2 June 1983 (Revised version)

6-4 PEDRO Photon Energy and Direction from Reconstructed Orbits

D. Barberis Eγ Internal Writeup April 84

6-5 PHEONIX

Private communication with J. A. G. Morris

6-6 GEANT User Guide and Reference Manual

R. Brun et al CERN DD/US/86, May 1983 (Revised version)

6-7 MAP User Guide

P. J. Flynn Eγ Internal Writeup Dec 1982

6-8 SAGE Reference Manual

J. Friedman SLAC Computational Group Technical Memo 145 (1979)

6-9 The Lund Monte Carlo for Jet Fragmentation

T. Sjostrand Comput. Phys. Common. 27 (1982) 243-284

6.6 - Figure Captions

6.1 Diagram of the Data Analysis Program

6.2 Multiplicity Distributions and Numbers of Verticies

6.3 Main Vertex Location

6.4 Single Particle Momentum Dirstibutions

6.5 Dip Distributions

6.6 Dip Distributions after EM Filter

6.7 The Photon Beam Energy Spectrum

6.8 Longitudinal Momentum Balance Excluding Extra Tracks

6.9 Longitudinal Momentum Balance Including Extra Tracks

CHAPTER VII

PHYSICS ANALYSIS

Chapter VII

7 - Physics Analysis

7.1 - Introduction

Three aspects of photoproduction in the photon energy range 70 - 200 GeV have been investigated using the data taken by the WA69 experiment in December 1983. All three aspects involved the photoproduction of charged particles only. In most cases all the charged particles produced were assumed to be pions. This was because the Photon Detector and Ring Image Čerenkov Detector were still being set up and tested ready for the main data taking in the summer of 1984.

The first channel studied was inclusive photoproduction of single charged particles (assumed to be pions). The single particle distributions obtained have been compared with single particle inclusive distributions obtained in other non-diffractive hadron-hadron interactions. The charge-multiplicity distributions have also been analysed in terms of KNO scaling and compared with theoretical predictions for non-diffractive hadron-hadron interactions. Finally, in the forward photon fragmentation region deviations from pure KNO scaling were investigated.

The second channel studied was the inclusive photoproduction of the $\rho(770)$ meson through its decay to $\pi^+\pi^-$. As described in Chapter 1 there are two processes by which the ρ can be produced; in the forward direction they can be produced by double diffractive dissociation and in the central region by quark fusion. The data

obtained in this experiment is compared with theoretical predictions and photoproduction data at lower energies. The differences in the production characteristics of the ρ's in the two regions have been investigated.

The final channel analysed was elastic four charged pion photoproduction with emphasis on looking for the $\rho'(1600)$ resonance. The $\rho'(1600)$ is believed to be the first excited state of the vector meson $\rho(770)$. It has been seen in photoproduction at lower energies (Ref. 7-1) and in e^+e^- annihilation experiments (Ref. 7-2). Since the cross-section for the elastic $\rho'(1600)$ is expected to be $\approx 0{\cdot}41\ \mu b$ (by extrapolation of the photoproduction cross-section found in previous experiments in the energy range 25 - 70 GeV), with approximately $0{\cdot}7\times10^9$ tagged photons on a 60 cm liquid hydrogen target only about 700 events including a $\rho'(1600)$ are estimated to be produced.

7.2 - Data Selection

All the data used in the physics analysis passed through a double pairs filter. As mentioned in Chapter 6, the double pairs filter removed electromagnetic contamination from the four-prong events. The filter required the 4-prong events to have two tracks with a dip greater than 3 mr and two independent pairs of tracks with a dip difference greater than 5 mr. All events were required to have a good beam track with a well measured photon energy.

The remaining data should contain all the hadronic events with a forward charged-multiplicity greater than three. The 'A' chamber

multiplicity cut in TRIDENT meant that the data sample contained very little diffractive (elastic) ρ, ω and ϕ production because these states decay to low charge-multiplicity states. The trigger will also have biased the low multiplicity forward production events because it was possible for all the charged tracks in an event to go through the gap in the middle of the hodoscope guillotines.

For the purpose of data analysis two sub-sets of the data were considered. The first set contained all the events where TRIDENT completely reconstructed the charged tracks and fitted them all to vertices (or Good Events). This selection was made by requiring the main vertex to be inside the hydrogen target and no extra tracks. The second set of events contained all events (or full event sample). In this set extra tracks were considered to be 'good' tracks if they had more than four space points in the Omega chambers and momenta within kinematic limits imposed by the maximum possible beam energy. All remaining extra tracks were ignored. Where possible the 'good' extra tracks were extrapolated back from the last measured point to the main vertex as a helix in order to estimate their momenta at this vertex. No requirement for the main vertex to be in the hydrogen target was imposed on this second set of events because tracks in an event not fitted to the vertex would cause TRIDENT to calculate a wrong vertex position. This problem with extra tracks also meant that the momenta of particles in an event with extra tracks were less accurately measured.

The number of tagged photons entering the hydrogen target (N_γ) during the December 1983 data taking period was estimated to be $0{\cdot}736 \pm 0{\cdot}037 \times 10^9$. For the 60 cm liquid hydrogen

target the number of target protons (N_p) was calculated to be $2{\cdot}54 \times 10^{24}$ cm^{-2}, giving a sensitivity, S of

$$S = N_\gamma N_p = 1{\cdot}87 \pm 0{\cdot}06 \text{ events/nb.}$$

The trigger efficiency was estimated to be $0{\cdot}9 \pm 0{\cdot}1$. This efficiency was included to account for the trigger counter efficiencies and the loss of events with a second double bremsstrahlung photon which fired the beam veto. The full data sample contained 172490 hadronic events (after the double pairs filter) of which 18199 were completely reconstructed. Thus, the cross-section for photoproduction of hadronic states with a forward charge-multiplicity greater than 2 in the energy range 70 and 200 GeV was estimated to be

$$\sigma_{Nfc>2}(\gamma P) = 100 \pm 10 \ \mu b.$$

The dominant errors in this cross-section are systematic errors in the trigger efficiencies. Acceptance corrections for the loss of hadronic events due to geometric trigger acceptance, the TRIDENT 'A' chamber multiplicity cut and electromagnetic double pairs filter have not been made, but for events with more than 2 forward charged tracks these effect are thought to be small compared with the errors quoted above. There may also be some residual electromagnetic contamination but this is also expected to be small. The cross-section quoted above corresponds to the total photoproduction cross-section without contributions from the elastic production of ρ, ω and ϕ which decay by the single diffractive dissociation process and low charge multiplicity inelastic scattering. This is because these events do not satisfy the TRIDENT 'A' chamber multiplicity cut. The elastic processes would add about 12 μb to the cross-section quoted above.

7.3 - Charged Particle Photoproduction and KNO Scaling

Data from both the fully reconstructed events and complete event samples were used for the inclusive single particle study. No other selection requirements were used other than those mentioned in the data selection section. Figure 7.1 shows the single π^+ and single π^- rapidity (Y) distributions, where

$$Y = \frac{1}{2} \text{ LOG } \left[\frac{E + P_l}{E - P_l} \right].$$

For the fully reconstructed events the rapidity distribution shows the characteristic flat top in the central region followed by a small rise before the rapid fall-off at high rapidity. In the backward region, many of the particles produced from fragmentation of the target proton were absorbed in the liquid hydrogen target. This meant that the acceptance of particles with rapidity less than about -2 was expected to be almost zero. Between rapidity -2·0 and 0· there is an excess of positive particles over negative particles due to the positive charge of the target proton. Most of this excess may in fact, be due to protons which have been assigned the pion mass.

The corresponding distributions for the events with extra tracks (the complete events sample), figure 7.2, show some similar features. The major difference is the increased number of tracks in the central region between $X_f = -0{\cdot}1$ and $X_f = 0{\cdot}0$. This was found to be due to the extra tracks produced by TRIDENT being mainly low momentum tracks. Most of these tracks are hadronic but some may be due to electron-positron pairs produced by conversion of soft photons from

the beam halo or low energy double bremsstrahlung photons from the tagging target.

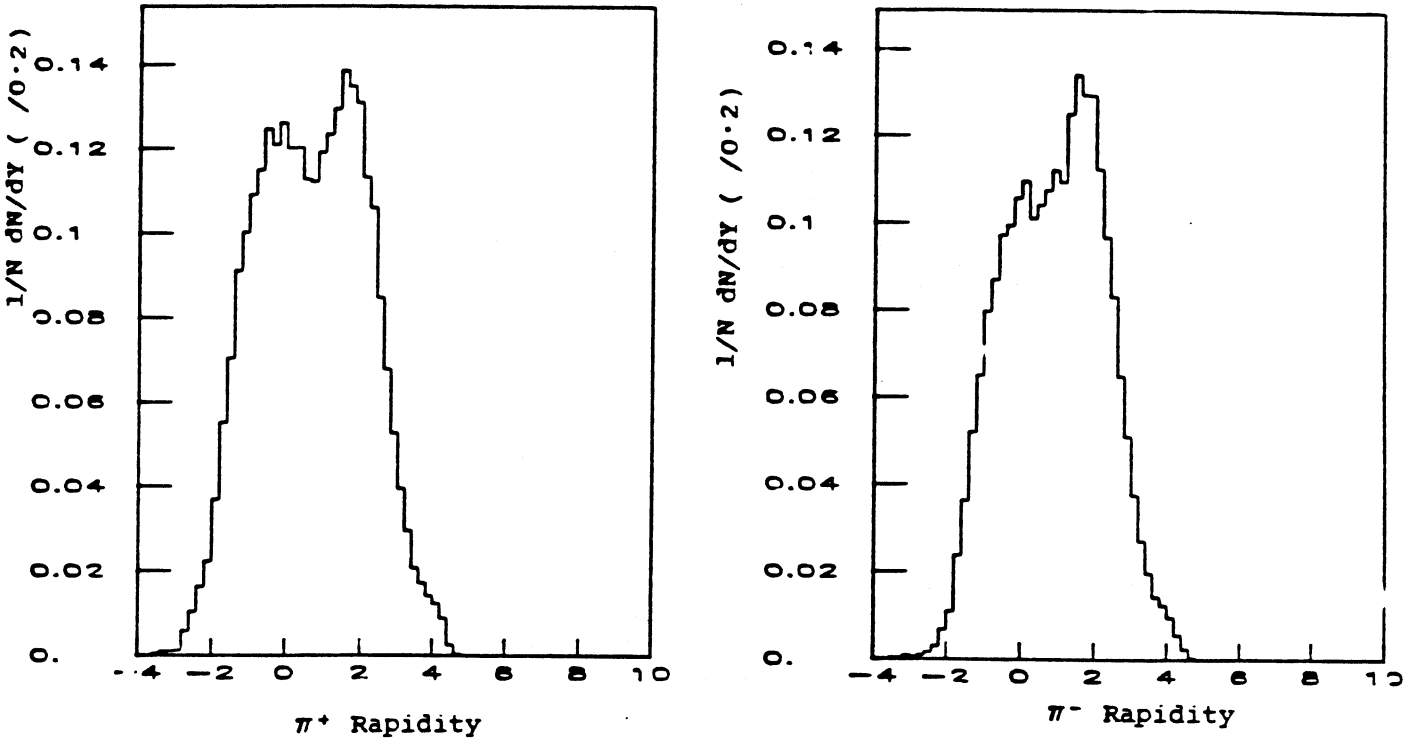

Fig. 7.1 Rapidity (Good Events)

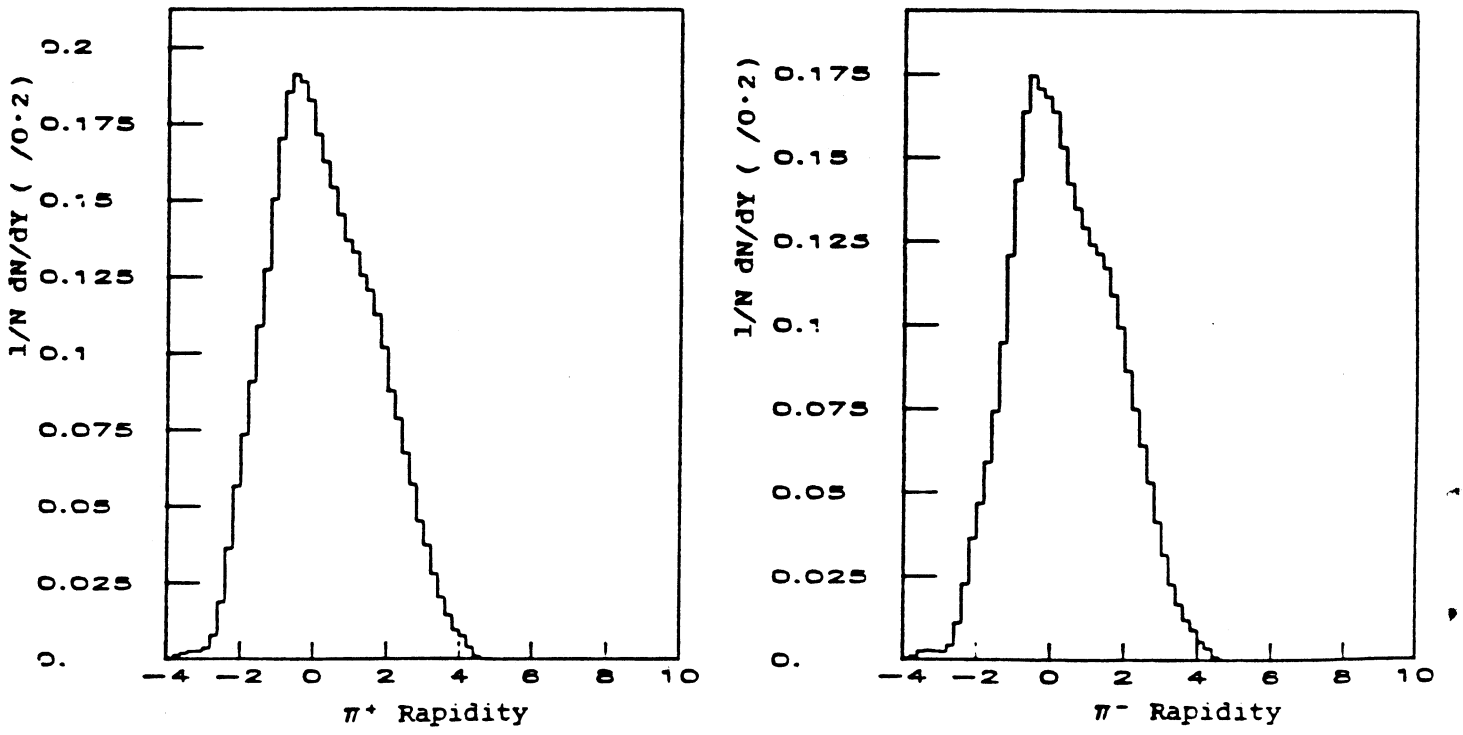

Fig. 7.2 Rapidity (all events)

The charge-multiplicity (Fig. 7.3) has a mean value of 5·19 for the fully reconstructed events and a mean value of 6·44 for the full event sample. The mean in the full event sample is made up of a mean of 4·54 tracks fitted to a vertex and 1·90 'good' extra tracks, with 0·95 extra tracks ignored.

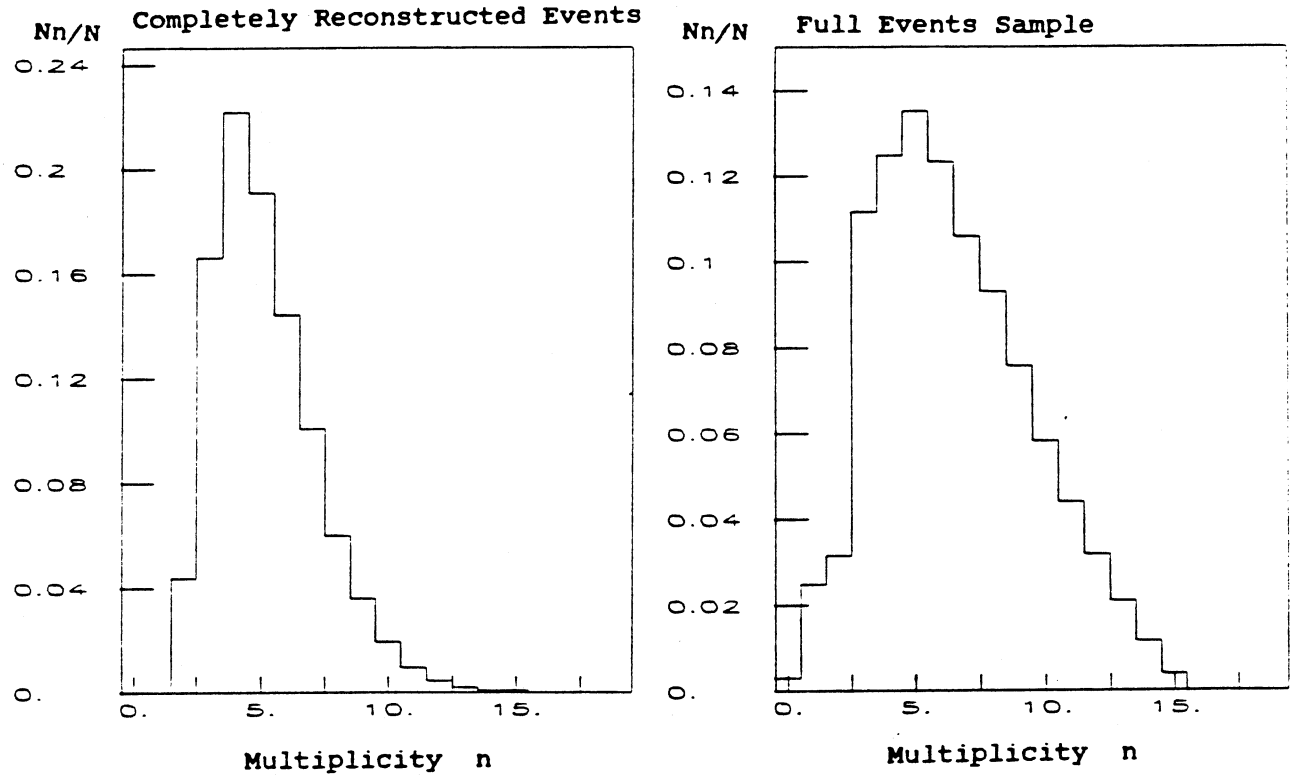

Fig. 7.3 Charge-Multiplicity Distributions

The normalised invariant-X_f distributions (or Feynman function $F(X_f)$) and P_t^2 distributions were plotted for all charged tracks (not acceptance corrected) for both the fully reconstructed events (Fig. 7.4). and the full event sample (Fig. 7.5). In the inclusive invariant-X_f distributions the peak due to extra tracks (seen in the rapidity distributions) shows itself as a peak near zero in the full event sample distribution. There is also a slight excess of forward tracks in the full event sample plot which are also probably due to extra tracks. The P_t^2 distributions are similar for both data samples, with a possible excess of high transverse momentum tracks in the full event sample, again probably due to extra tracks being included. The P_t^2 distributions were fitted to an exponential of the form $A \cdot e^{-\alpha P_t^2}$. The coefficients α were found to be 6·2 for the good events and 7·5 for the full event sample. The P_t^2 distributions for the π^+ and π^- were also fitted to this function and were found to have no significant differences. The proportion of hard events (high P_t^2) in this data is higher than that found in lower energy photoproduction experiments (Fig. 7.6, Ref. 7-3).

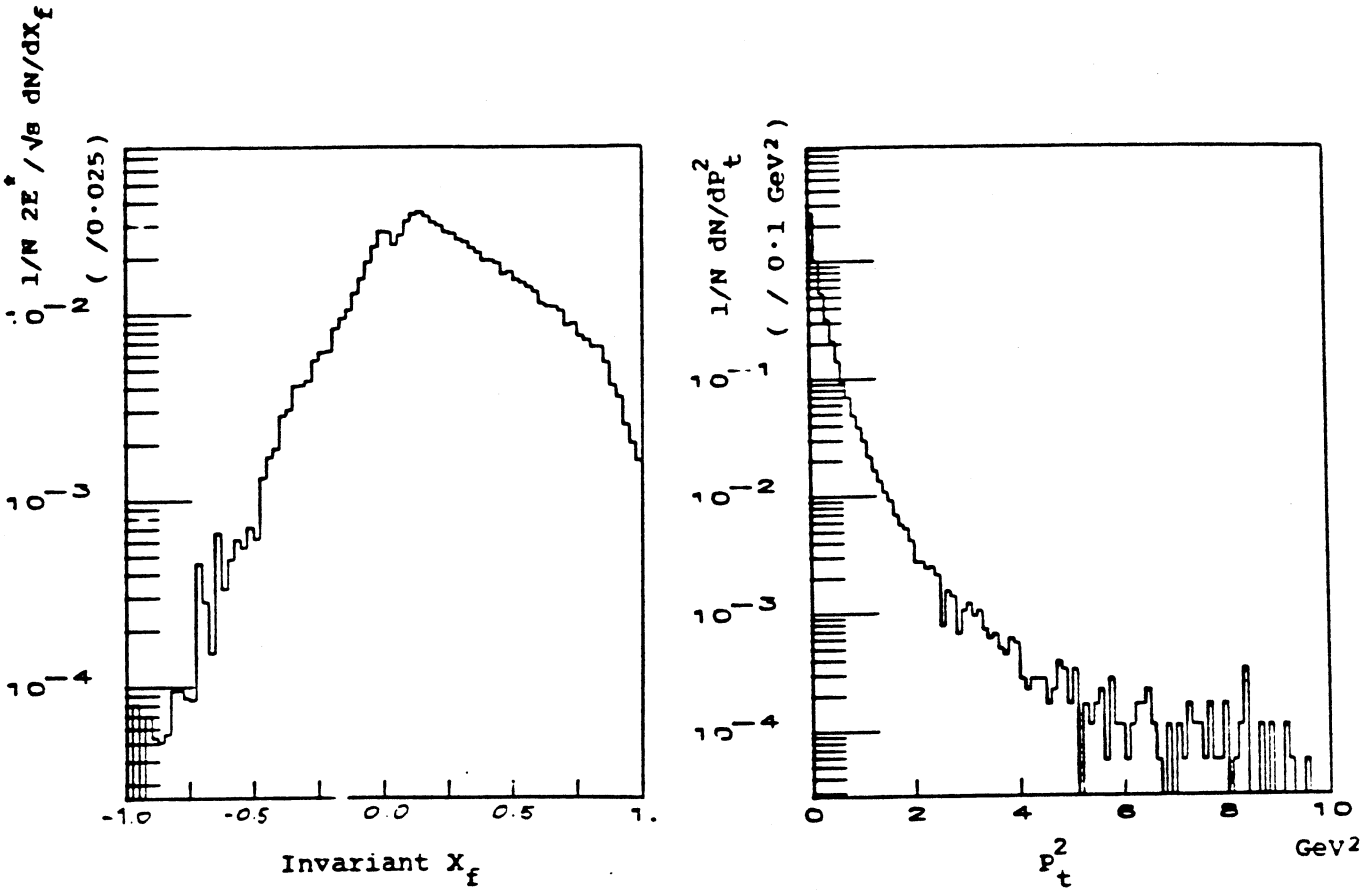

Fig. 7.4 Invariant-Xf and Pt2 Distributions (Good Events)

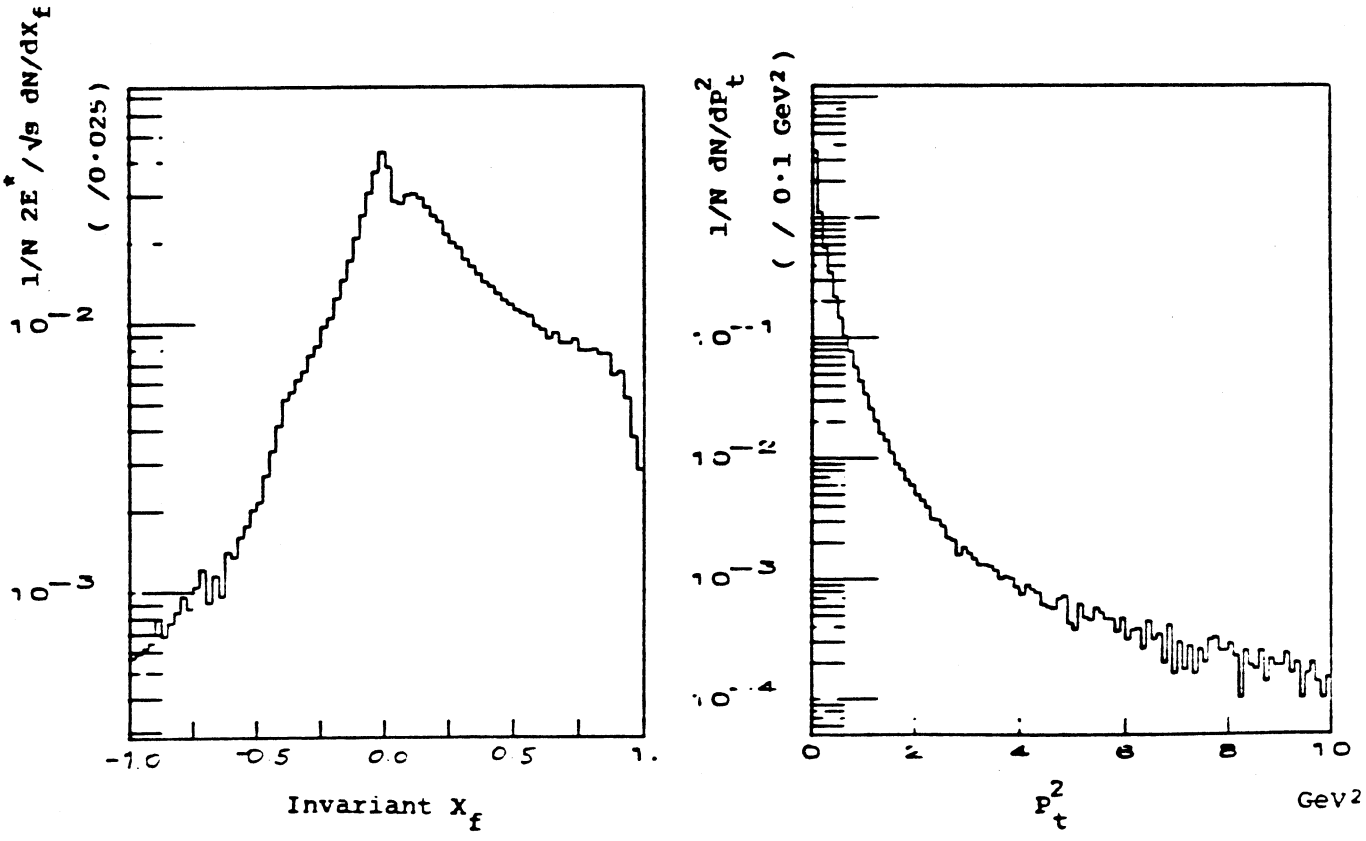

Fig. 7.5 Invariant-Xf and Pt2 Distributions (all events)

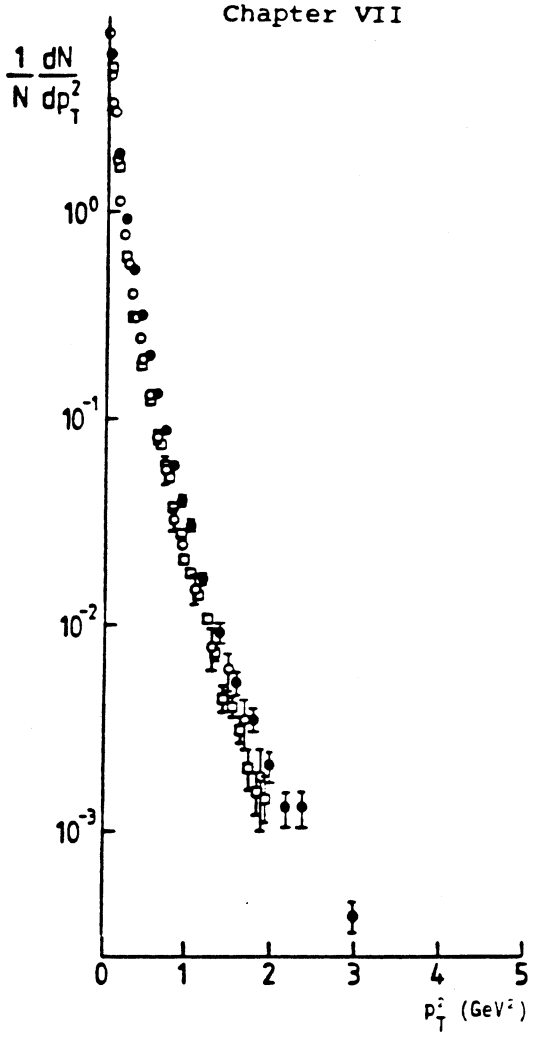

Fig. 7.6 Pt2 Distribution in Photoproduction at 50-70 GeV

In order to investigate the scaling properties of inclusive single charged particle production the data was divided up into six bands of beam energy. Each band was chosen with an equal logarithmic width so that each contained roughly the same number of events. Figure 7.7 shows the number of events against the logarithm of the photon beam energy and shows the six bands considered. The number of events in each energy band reflects the distribution of energies of the tagged photon convoluted with the total inelastic cross-section as a function of energy (which is almost flat over this energy range) and any beam energy dependent components of the acceptance. The invariant Feynman X and P_t^2 distributions were plotted for each

energy band (not shown) and showed no significant variation with beam energy. The mean charge-multiplicity was then calculated in each band (Fig. 7.8). These plots suggest a linear dependence between the mean multiplicity and the $Log(E_\gamma)$ (or equivalently, log(s)). By fitting the distributions to

$$\langle n_c \rangle = a\ Ln(E_\gamma/100) + b$$

the parameters a and b were found to be

$$a = 0{\cdot}81 \pm 0{\cdot}05, \quad b = 5{\cdot}15 \pm 0{\cdot}02, \quad \text{with } \chi^2 = 3{\cdot}6 \text{ for 4 dof}$$

for the fully reconstructed events and

$$a = 0{\cdot}83 \pm 0{\cdot}04, \quad b = 6{\cdot}39 \pm 0{\cdot}01, \quad \text{with } \chi^2 = 4{\cdot}3 \text{ for 4 dof}$$

for the complete event sample.

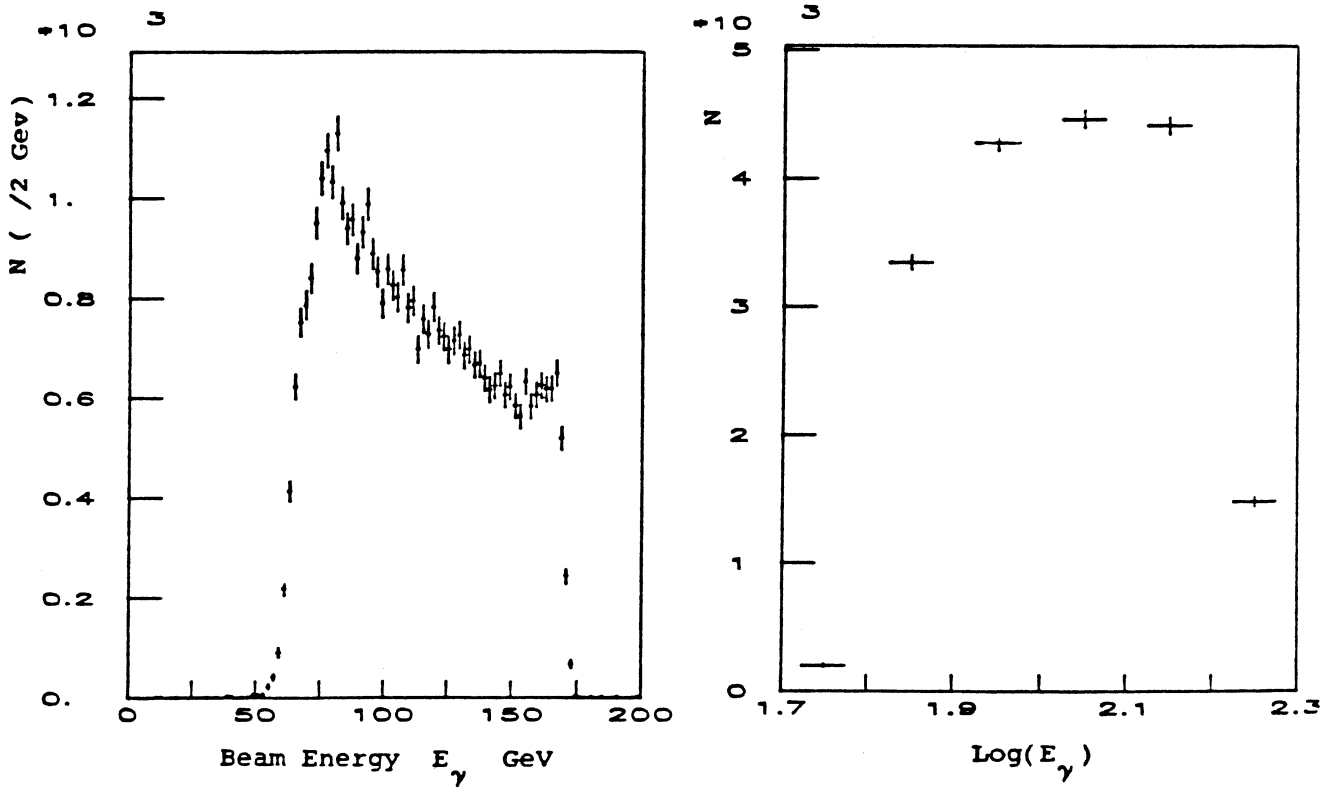

Fig. 7.7 Number of Events against Beam Energy

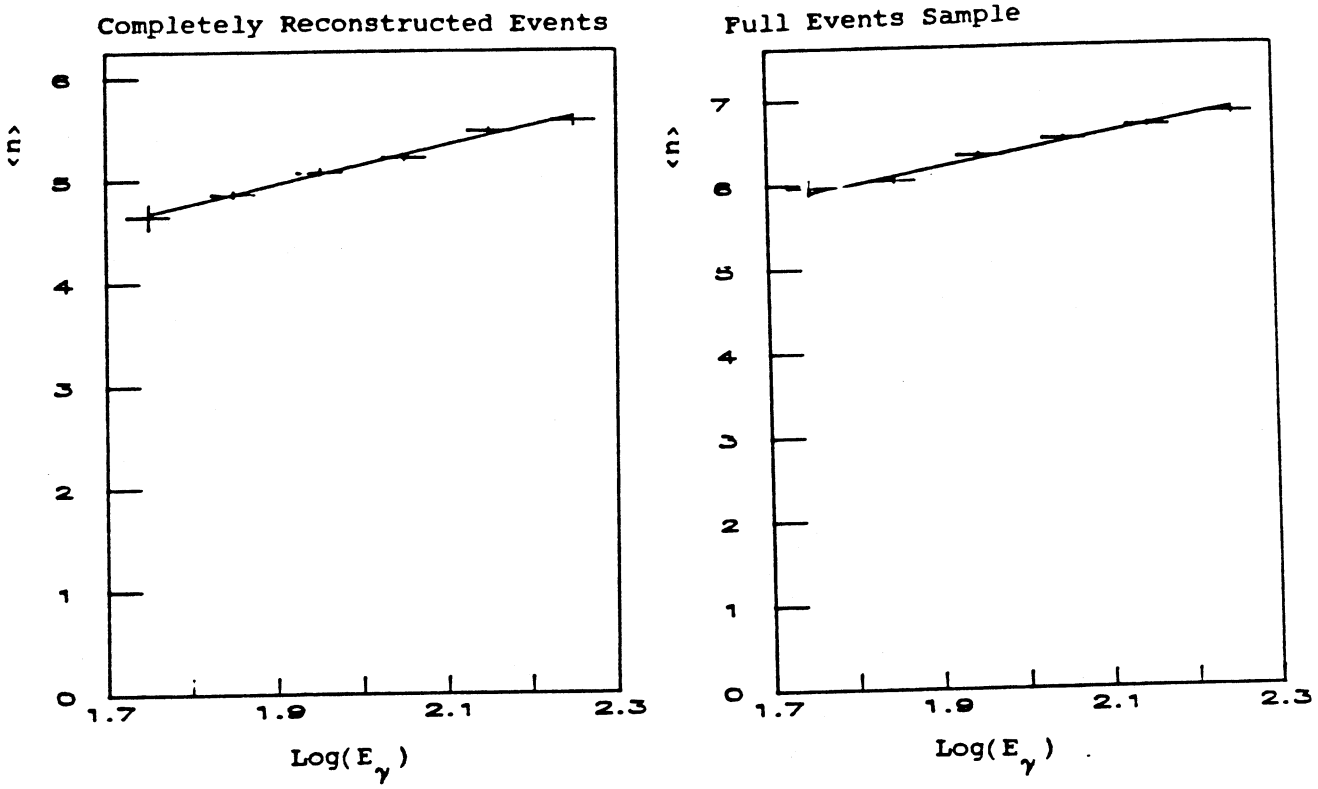

Fig. 7.8 Mean Charge Multiplicity

Within each energy band the multiplicity distribution was recalculated in terms of the KNO scaling function $\psi(z)$ and compared with the theoretical distribution for hadron-hadron interactions (Fig. 7.9). For the completely reconstructed events the agreement between the data and the theoretical curve is good (with χ^2 between 12 and 77 for 17 dof) but for the full event sample the agreement is not so good. In the full event sample there are more high multiplicity events and less mid-range multiplicity events than in the completely reconstructed events and as predicted by the model described in Chapter 1. This suggests that some of the extra tracks are not associated with the main event even though they may improve the Px difference as seen in Chapter 6. A second low energy double bremsstrahlung photon interacting inside Omega would have this

effect.

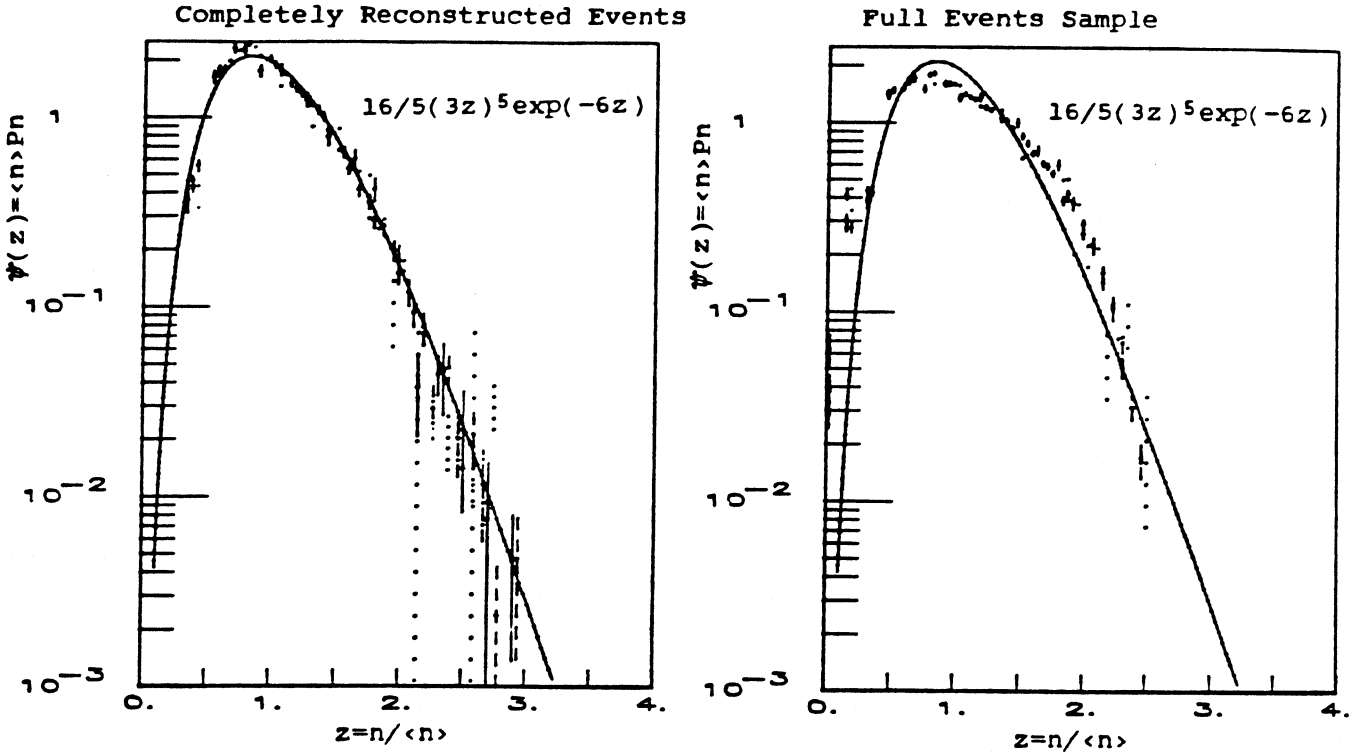

Fig. 7.9 KNO Scaling Distributions for Photoproduction

To avoid the problem with acceptances in the backward hemisphere the track produced in the forward hemisphere ($X_f > 0{\cdot}0$) and tracks produced in the backward hemisphere ($X_f < 0{\cdot}0$) were considered separately. The single particle acceptance in the forward hemisphere is expected to be 100% whereas the acceptance in the backward hemisphere is known to be very low at low X_f and should rise to nearly 1·0 in the central region near $X_f \approx 0{\cdot}0$. The arguments in Chapter 1 leading to KNO scaling (section 1.4) will hold in both regions separately because the Feynman functions are still being integrated between energy scale independent limits (Ref. 7-4). At an intuitive level it is expected that the forward hemisphere is due to the fragmentation of the beam photon and the backward hemisphere is due to the fragmentation of the target proton. This division enables the backward hemisphere to be compared with hadron

induced proton fragmentation seen in liquid hydrogen bubble chamber experiments. Similarly, the photon fragmentation can be compared with forward fragmentation in $\pi^{\pm}$, $k^{\pm}$, PP and $\bar{P}P$ experiments.

7.3.1 - The Proton Fragmentation Region

As mentioned above, in the backward hemisphere, the proton fragmentation region is acceptance limited by the loss of low energy tracks in the liquid hydrogen target. To assess this loss, this photon data was compared with liquid hydrogen bubble chamber data for inelastic scattering of pions and kaons at similar energies (Ref. 7-5). Figure 7.10 shows the normalised invariant cross-section as a function of Feynman X (or Feynman function $F(X_f)$) for the photon data (not acceptance corrected) and the bubble chamber data. The mean backward charge-multiplicity (Fig. 7.11) shows a slight increase in multiplicity with photon energy, but it is difficult to say whether this is due to the acceptance changing as the photon energy increases or the multiplicity itself rising. The mean charge-multiplicity in this region over the full energy range was found to be $1{\cdot}6 \pm 0{\cdot}2$ for the fully reconstructed events and $2{\cdot}9 \pm 0{\cdot}2$ for the complete event sample. By comparing the invariant X_f distributions for the photon data and the k^-P bubble chamber data above, the average acceptance loss was estimated to be $\approx 50\% \pm 15\%$. Thus, the corrected backward charge-multiplicity would be about $3{\cdot}2 \pm 0{\cdot}6$ for the good event sample and $5{\cdot}8 \pm 1{\cdot}0$ for the complete event sample. The mean multiplicity in non-single PP scattering at the ISR and in π^-P scattering in the 30" hydrogen bubble chamber at NAL (Ref. 7-6) has been found to

be about 7 at similar centre of mass energies ($\sqrt{s}$ = 14 GeV). Hence, in a single hemisphere a mean of about 3.5 would be expected. This is in agreement with the corrected estimate for the completely reconstructed events and supports the theory that the low energy extra tracks are not associated with the main event.

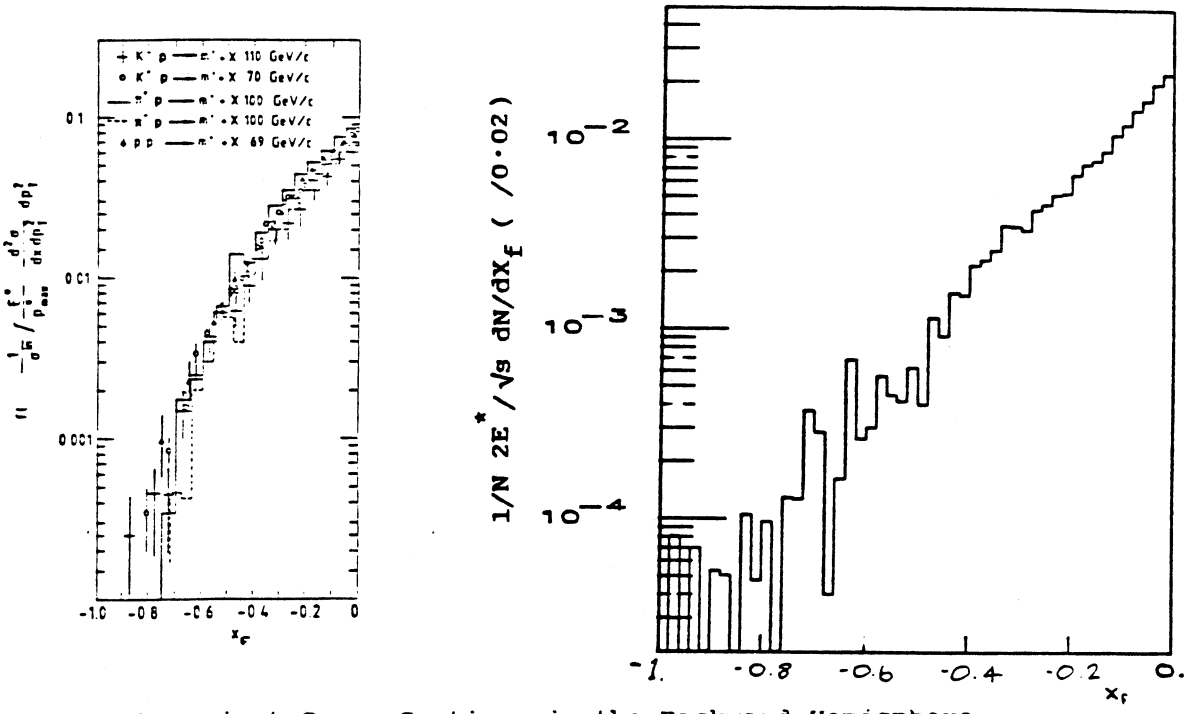

Fig. 7.10 Invariant Cross-Sections in the Backward Hemisphere

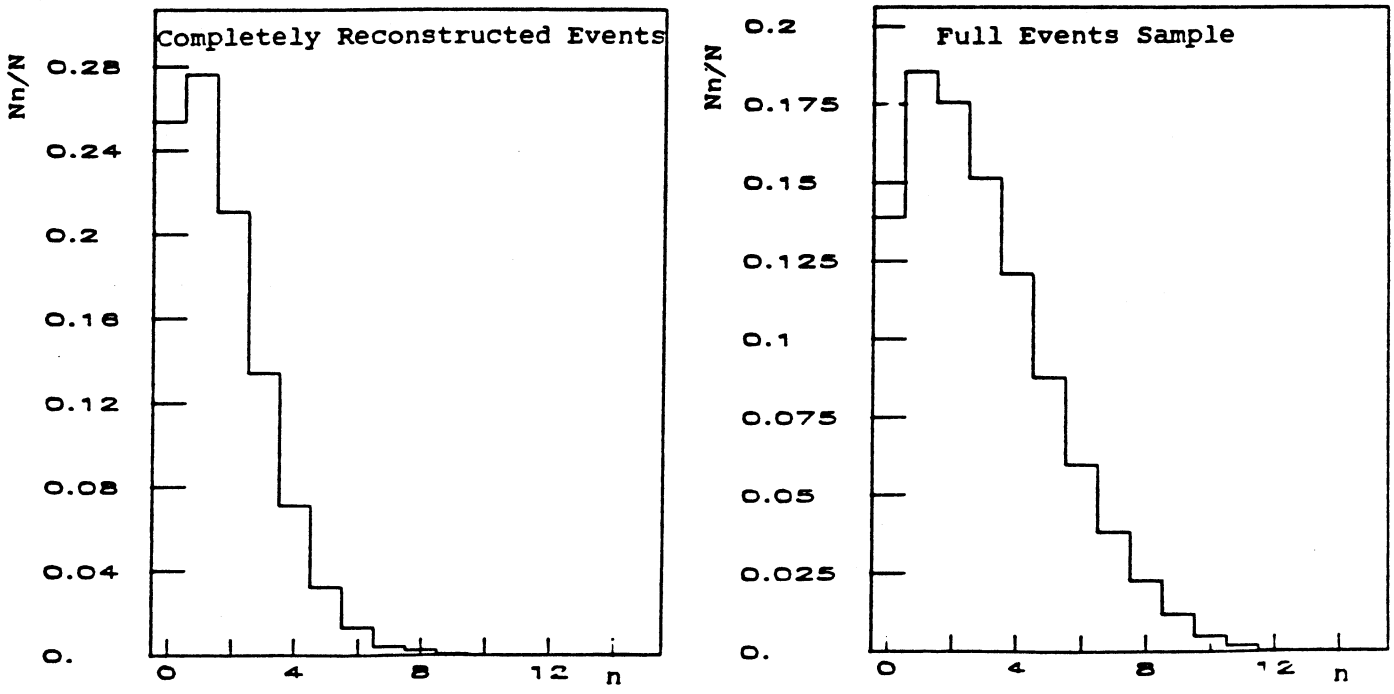

Fig. 7.11 Backward Charge-Multiplicity

7.3.2 - The Photon Fragmentation Region

The forward X_f and P_t^2 distributions for the fully reconstructed events and full event sample are shown in figure 7.12.

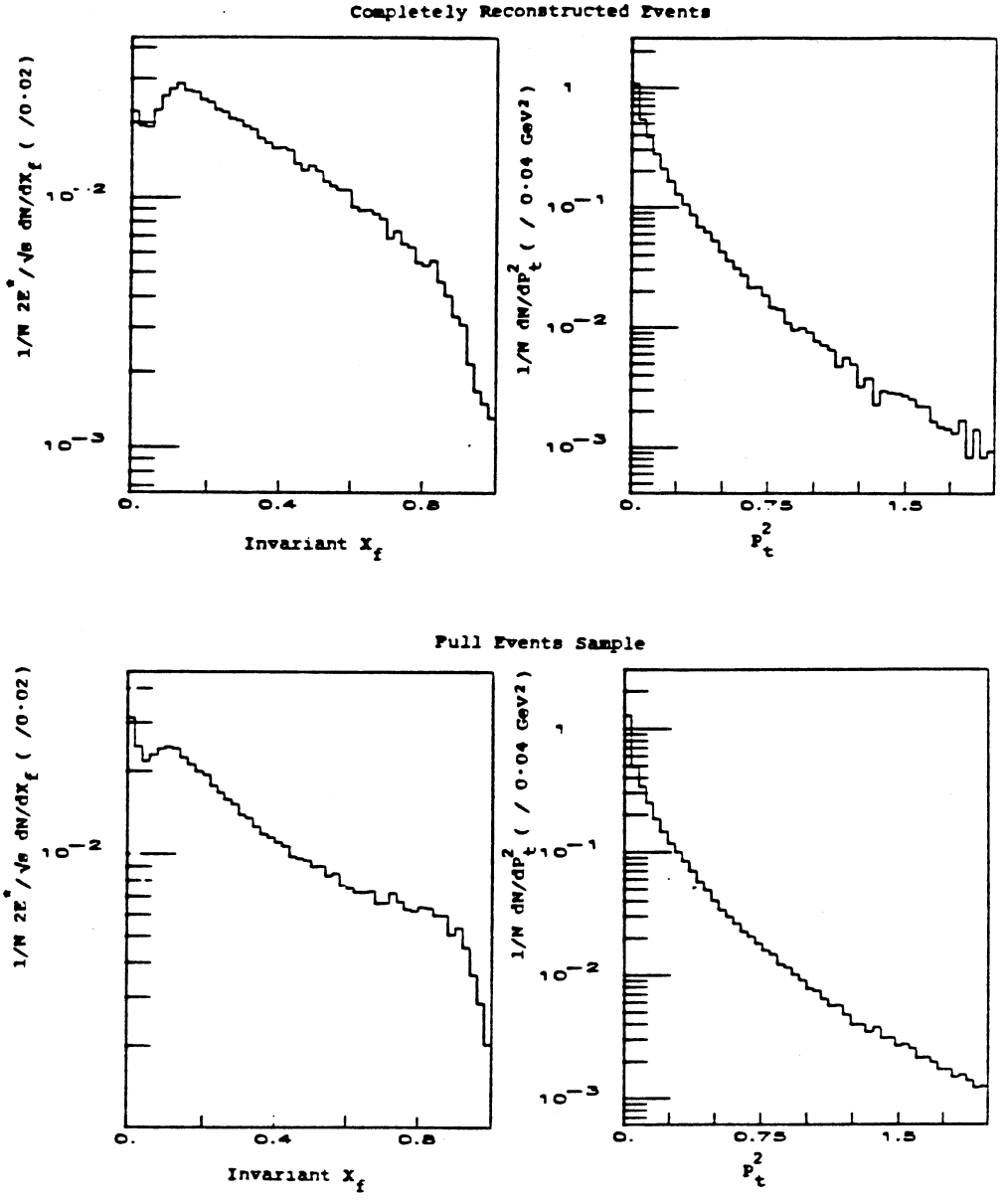

Fig. 7.12 Forward Single Particle Xf and Pt2 Distributions

The mean charge-multiplicity in the forward direction was then calculated in the six beam energy bands (Fig. 7.13). The forward mean

multiplicity was fitted with a linear dependence on $Ln(E_\gamma)$ as for the full range data. For the good events the coefficients in the fit to

$$\langle n_f \rangle = a\ Ln(E_\gamma/100) + b$$

were found to be

$$a = 0{\cdot}41 \pm 0{\cdot}04, \quad b = 3{\cdot}49 \pm 0{\cdot}01, \text{ with } \chi^2 = 15{\cdot}3 \text{ for 4 dof.}$$

For the full events sample the coefficients were found to be

$$a = 0{\cdot}24 \pm 0{\cdot}02, \ b = 3{\cdot}52 \pm 0{\cdot}01, \quad \text{with } \chi^2 = 19{\cdot}5 \text{ for 4 dof.}$$

It can be seen from these two data samples that the complete events have on average the same number of charged forward tracks with a small beam energy dependence. Using the mean multiplicity in each energy band the KNO scaling function $\Psi(z)$ was calculated and compared with the theoretical hadron-hadron model (see section 1.4) (Fig. 7.14). The χ^2 obtained by comparing the theoretical curve and the data in each energy band ranged from 13·6 to 82 (for 17 degrees of freedom) for the completely reconstructed events. Again systematic deviations from the predicted curve were observed in the full data sample. From this it can be seen that the completely reconstructed data sample is in good agreement with the theoretical KNO scaling predictions, but the complete event sample shows systematic deviations from the predicted curve similar to those in the full range full event sample distribution.

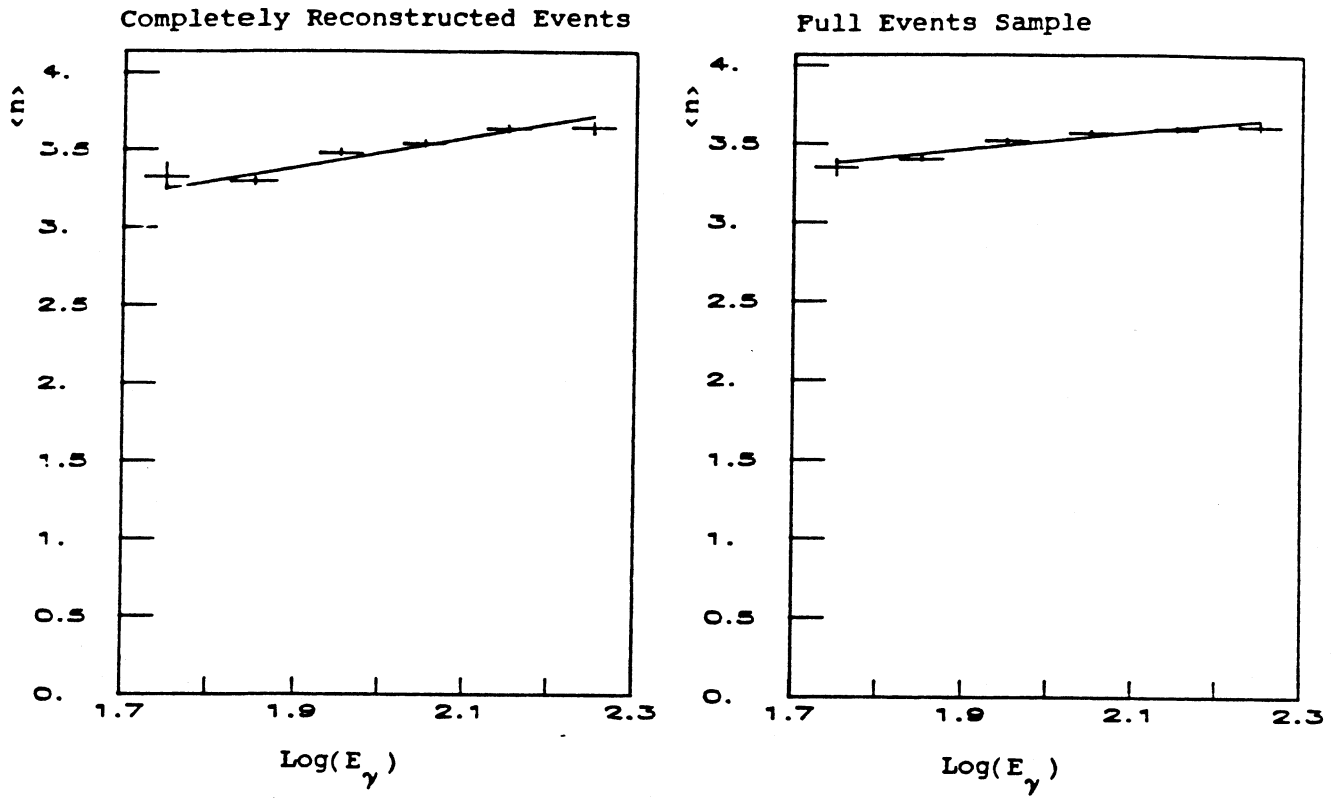

Fig. 7.13 Mean Forward Charge Multiplicity

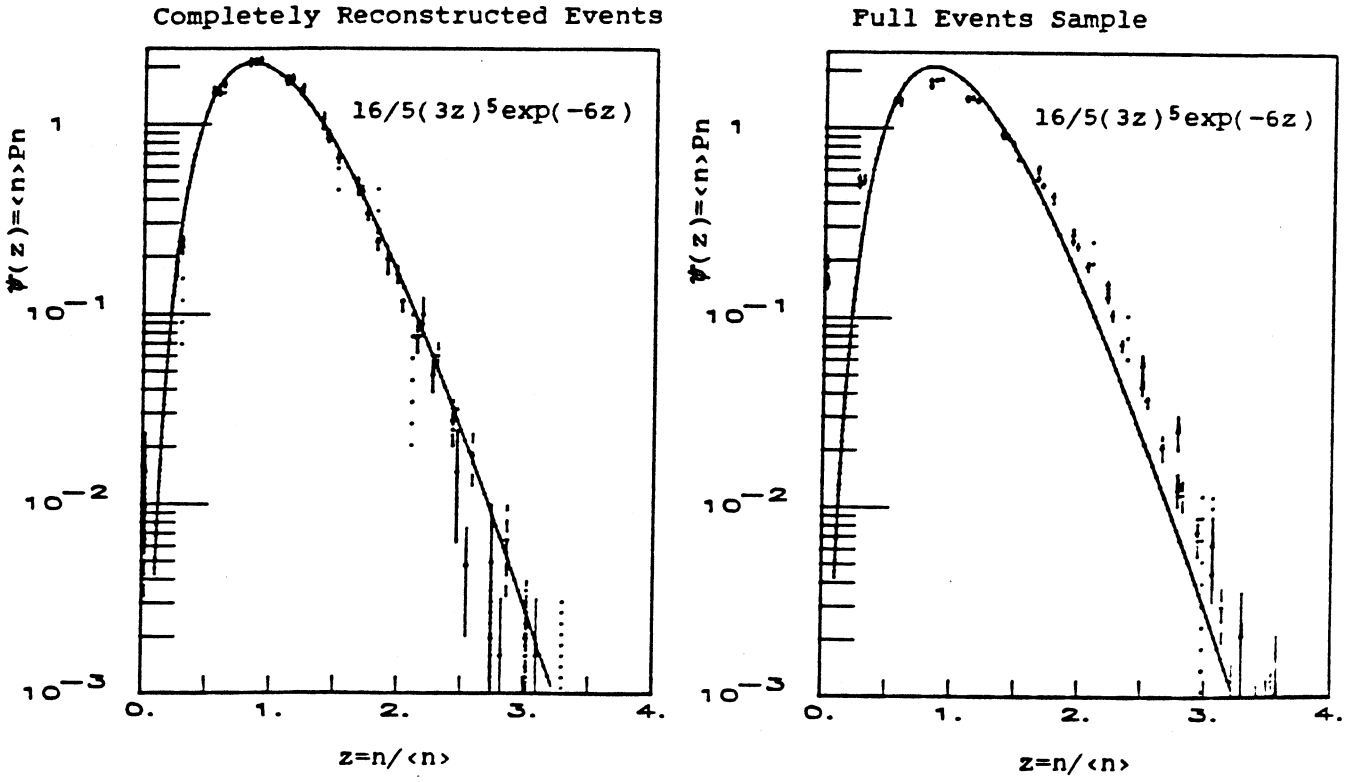

Fig. 7.14 KNO Scaling Function in the Forward Hemisphere

In order to investigate deviations from the KNO scaling in the photon decay hemisphere moments of the charge-multiplicity were calculated in the six beam energy bands. The simplest moment, the mean multiplicity ($\langle n \rangle$) where

$$\langle n \rangle = \Sigma_n \, nP_n(s)$$

has already been discussed. The next highest moment, the dispersion moment D_2, where

$$D_2 = \langle (n - \langle n \rangle)^2 \rangle^{\frac{1}{2}}$$

and the related two particle correlation function f_2, where

$$f_2 = D_2^2 - \langle n \rangle$$

were calculated. The moments $c_2 - c_5$ used in the KNO scaling theory (Section 1.4) where

$$c_k = \frac{\langle n^k \rangle}{\langle n \rangle^k} = \int z^k \psi(z) \, dz$$

were also calculated. Figure 7.15 shows these moments $c_2 - c_5$ plotted against beam energy. The lower moments show no significant dependence on the beam energy, but in the higher moments there may be a slight variation with beam energy. For pure KNO scaling the dispersion moment is predicted to be proportional to the mean multiplicity. Figure 7.16 shows the dispersion moment D_2 plotted against the mean multiplicity (from Fig. 7.14) for each energy band. By using a linear least squares to fit this data to the function

$$D_2 = a\langle n \rangle + b$$

the parameters a and b were found to be:

$$a = 0{\cdot}78 \pm 0{\cdot}09 \qquad b = -0{\cdot}77 \pm 0{\cdot}3$$

for the completely reconstructed events and

$$a = 1{\cdot}16 \pm 0{\cdot}13 \qquad b = -1{\cdot}6 \pm 0{\cdot}4$$

for the full event sample. The fact that in both cases the intercept (b) is non-zero shows that there are slight deviations form pure KNO scaling.

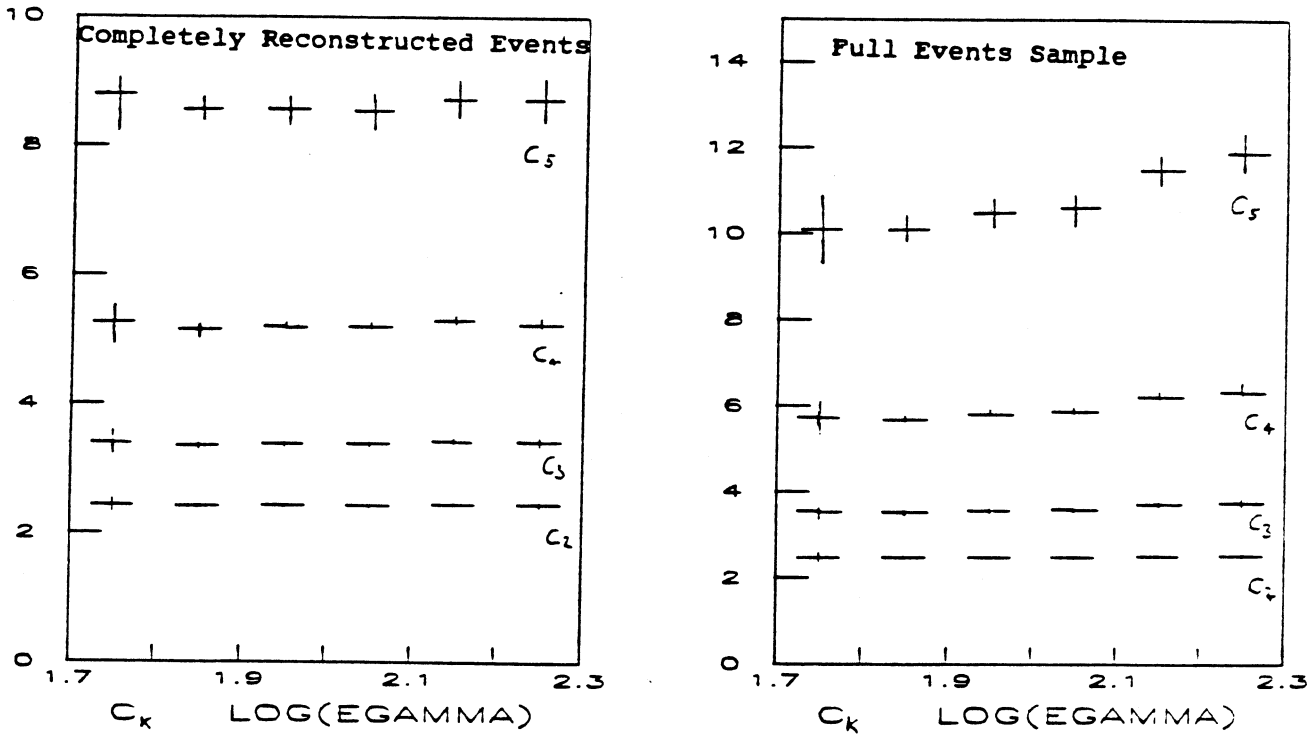

Fig. 7.15 Photon Fragmentation Charge Multiplicity Moments

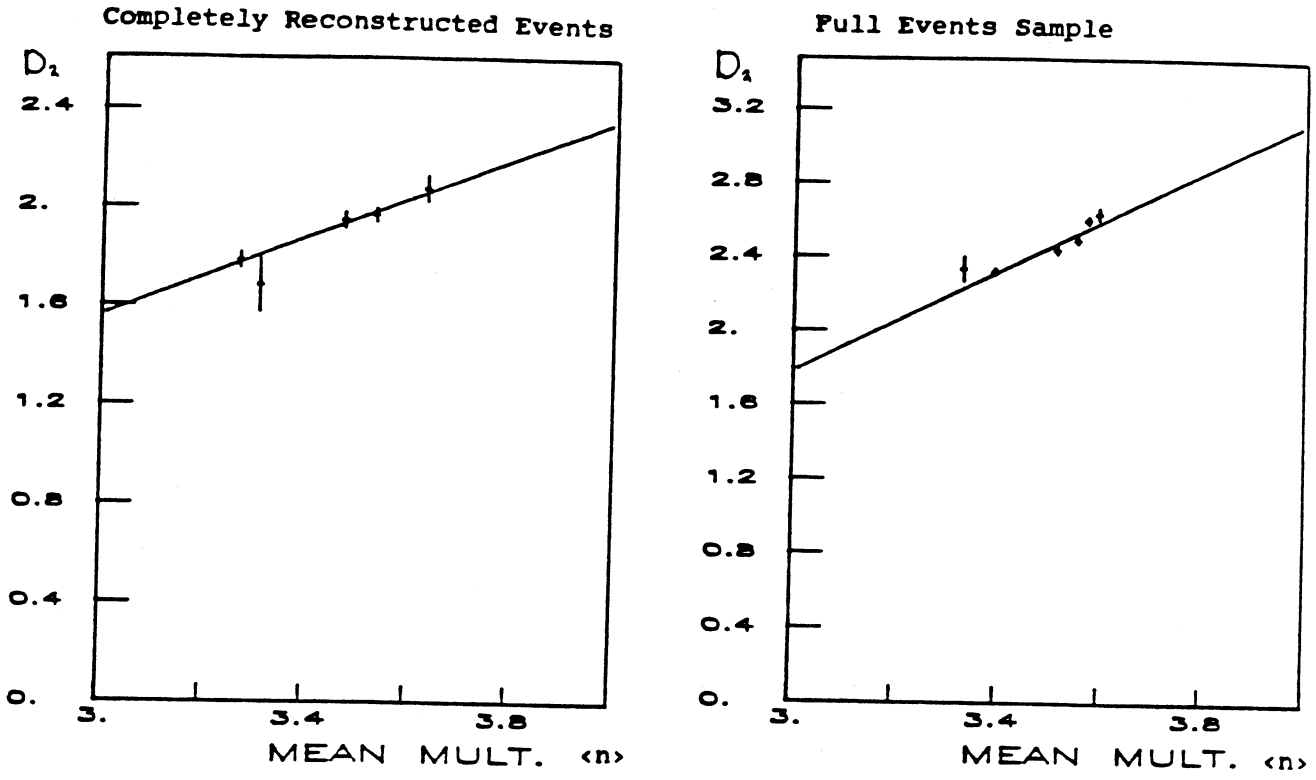

Fig. 7.16 Photon Fragmentation Charge Multiplicity Dispersion

The two particle correlation function f_2, which can also be expressed in the form

$$f_2 = \int \left[\frac{1}{\sigma_{tot}} \frac{d^6\sigma}{dp_1^3 dp_2^3} - \frac{1}{\sigma_{tot}} \frac{d^3\sigma}{dp_1^3} \frac{1}{\sigma_{tot}} \frac{d^3\sigma}{dp_2^3} \right] dp_1^3 dp_2^3$$

has also been plotted (Fig. 7.17) as a function of mean multiplicity in each energy band. In order to compare this with measurements of f_2 from PP (ISR, CERN) data (Ref. 7-7) and other data (Ref. 7-8) the values obtained in the forward hemisphere were scaled up to simulate the full rapidity range (inclusive inelastic $\gamma\gamma \longrightarrow X$!). In this scaling both the multiplicity ($\langle n_{fc} \rangle$) and the dispersion (D_2) were assumed to double in value. Figure 7.18 shows the values of f_2 obtained by this procedure plotted together with the PP data from the ISR, Data from other hadron

scattering experiments at lower energy is also shown along-side. The photon data shows the same trend of increasing f_2 with mean multiplicity (Ln(s)) and about the same magnitude as the data from the other experiments.

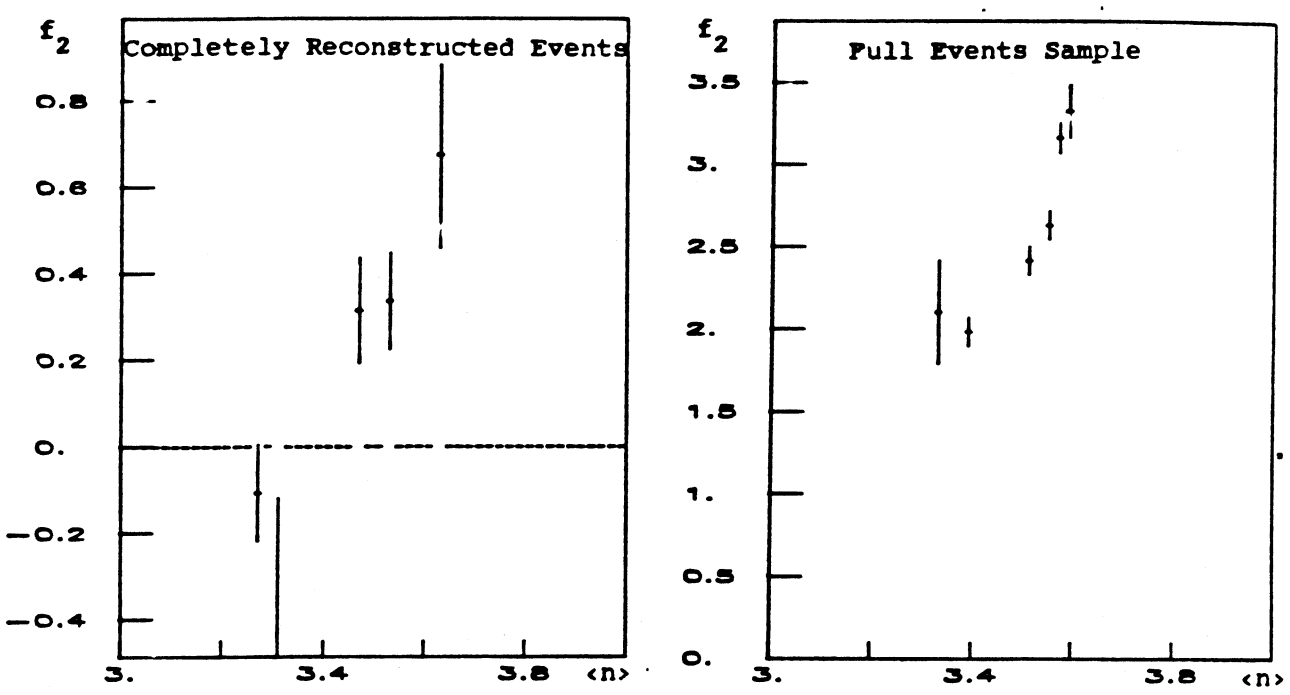

Fig. 7.17 Two Particle Correlation Function f2

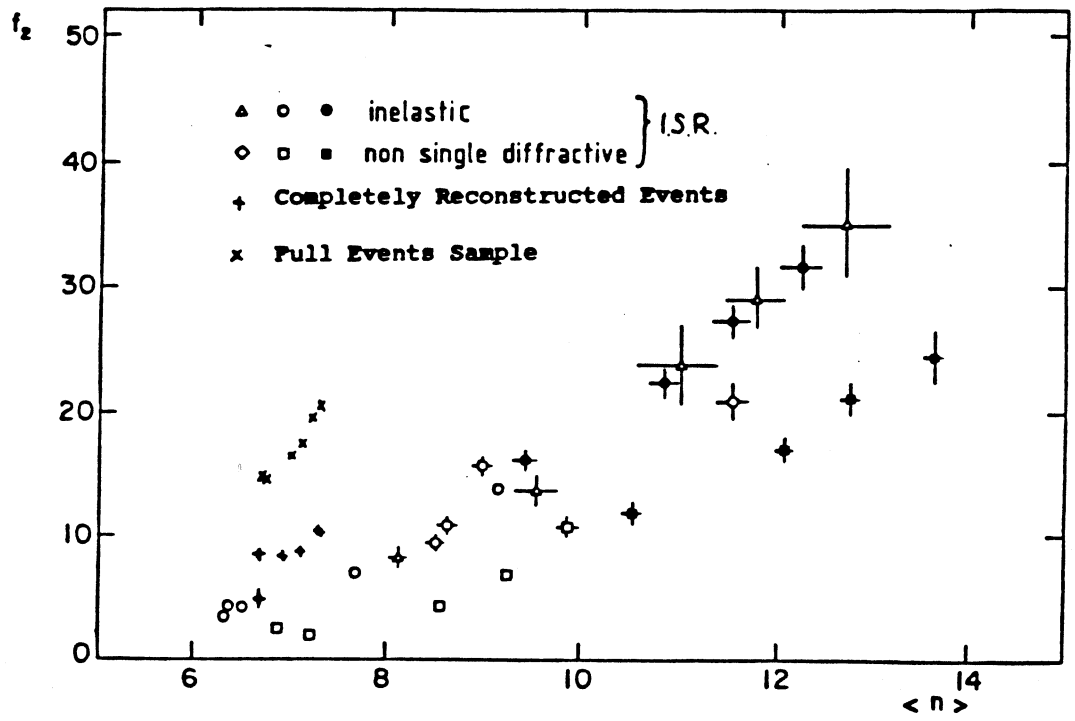

Fig. 7.18 f2 for Photoproduction, PP and Hadron Scattering

7.4 - Inclusive Rho(770) Photoproduction

Data from the completely reconstructed event sample was used for the inclusive $\rho(770)$ investigation. Following the data selection all the $\pi^+\pi^-$ combinations within each event were formed. Combinations were accepted if they had a dip difference greater than 5 mr. This selection was imposed to reduce low mass combinatorial background and reduce the contamination due to soft photons converting to e^+e^- pairs. The two pions inclusive invariant mass spectrum (Fig. 7.19) shows a clear peak at the ρ mass (0·770 GeV) sat upon a falling combinatorial background. By fitting this spectrum (using the HBOOK fitting routines, Ref. 7-9) to a Breit-Wigner (BW) of the form

$$BW(M) = \frac{M\, M_r\, \Gamma_r}{\left[(M^2 - M_r^2)^2 + M_r^2\Gamma_r^2 \right]},$$

with the resonant mass (M_r) and width (Γ_r) constrained to that of the $\rho(770)$ together with a background (BG) of the form

$$BG(M) = (M - M_t)^{\alpha} \cdot e^{-(\beta M + \gamma M^2)},$$

where M_t is the 2 pion threshold mass and parameters α, β and γ were determined by the fit. The fit was made between the masses 0·30 GeV and 1·50 GeV to avoid bias from the long combinatorial tail and steep rise near threshold. A better fit was obtained with the rho mass set at 0·75 GeV, which suggests that there was a systematic error in the momentum calculation for each track. This could be due to the magnitude of the Omega magnetic field being slightly different from that in the reconstruction program TRIDENT.

Events with double ρ production were counted twice by this procedure but the effect was thought to be small. The number of $\rho(770)$ was found to be $0{\cdot}265 \pm 0{\cdot}020$ per event. If we assume that this ratio holds for all events and not just the completely reconstructed events, then using the total inelastic cross-section calculated in section 7.2 the inclusive inelastic cross-section was estimated to be

$$\sigma_{inc,inel}(rho) = 27{\cdot}2 \pm 2{\cdot}1 \pm 6{\cdot}1 \ \mu b.$$

The first error quoted is the statistical error obtained from the fit and the second is the estimated systematic error. The main systematic error comes from the assumption about the ρ content of the events which were not fully reconstructed by TRIDENT (assumed to be 20%). This error together with the uncertainty in the trigger efficiency was combined to give the quoted systematic error. This cross-section only really applies to forward and central production of rho mesons because the acceptance for backward tracks ($X_f < -{\cdot}3$) falls off rapidly. The value obtained is in agreement with that obtained in photoproduction in the energy range 20 - 70 GeV (Ref. 7-10)

$$\sigma_{inc,inel}(rho) = 21{\cdot}6 \pm 1{\cdot}0 \pm 2{\cdot}7 \ \mu b.$$

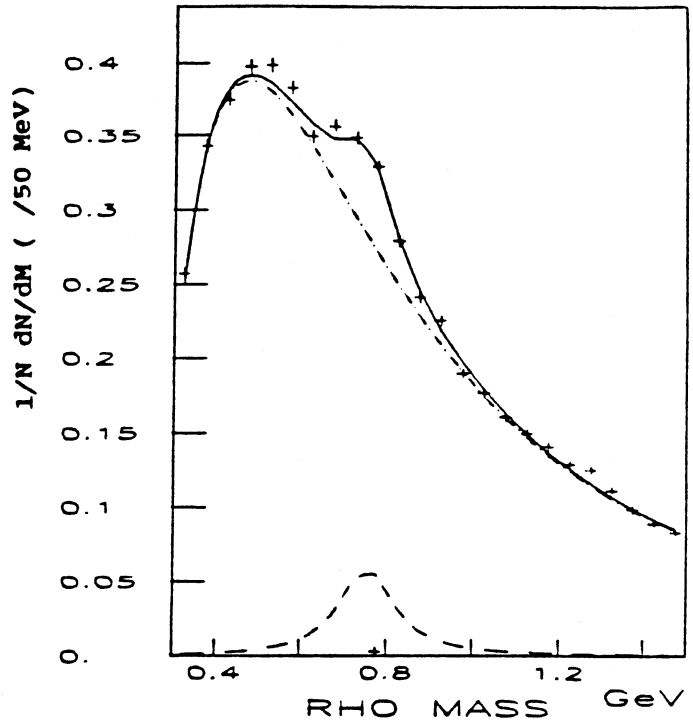

Fig. 7.19 2 Pion Invariant Mass Spectrum

In order to investigate the ρ production as a function of Feynman-X, Pt^2 and multiplicity the peak-wings technique was used. For this the peak was considered to be in the two pion mass range 0·670 to 0·870 GeV and the wings a further 0·1 GeV on either side of the peak. By this method the number of ρ's extracted was $\approx$ 0·055 ± 0·002 per event, which is approximately half the expected number taking into account the fact that the choice of the peak-wings regions would leave $\approx$ 43% of the expected signal. The discrepancy may be due to the concave nature of the background in the region of the ρ. Using the peak-wings extraction the invariant X_f and P_t^2 distributions were plotted (Fig. 7.20). The invariant X_f distribution (or Feynman function) shows a central production region and a forward production region with a dip between the regions at about $X_f = 0{\cdot}7$. There is little data at $X_f < -{\cdot}3$ because

the acceptance of slow tracks was poor. The acceptance in the forward direction is expected to be flat, the only constraint being a forward track to fire the hardware trigger and two more tracks seen in the Omega chambers to satisfy the 'A' chamber cut in TRIDENT.

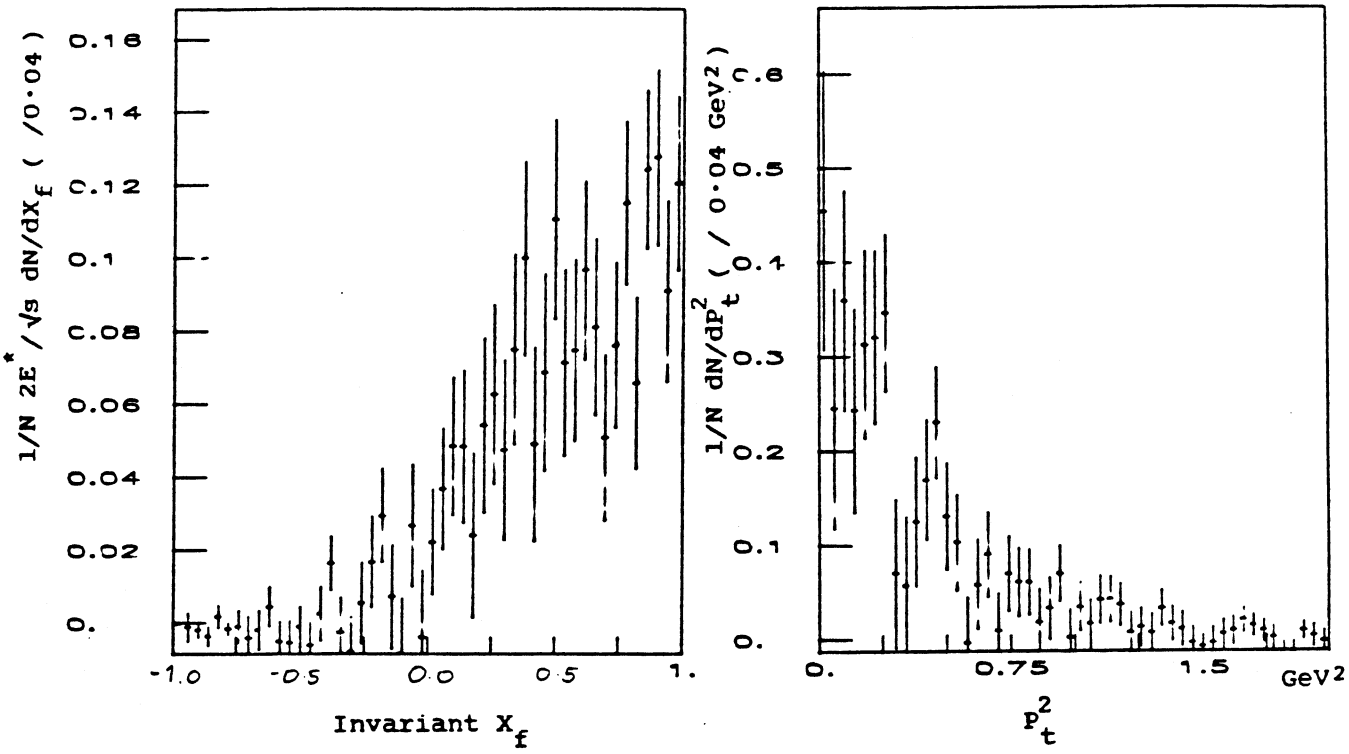

Fig. 7.20 Rho Invariant Xf and Pt2 Distributions

In order to calculate the invariant X_f distribution of the ρ's more accurately the two pion invariant mass was plotted against X_f. Then, in slices of X_f the partial mass spectrum was fitted in the same way as the full mass spectrum (with the rho mass fixed at 0·750 GeV). Figure 7.21 shows the partial mass spectra with the fitted curves superimposed. The signal and background have also been superimposed as dot-dash lines and dash-dash lines respectively. The invariant X_f distribution calculated from the fits in each slice (Fig. 7.22a) shows the same trends as the distribution calculated by the peak-wings technique. The rho inclusive invariant X_f distribution obtained is similar to that obtained in earlier photoproduction experiments between 25 - 70 GeV (Fig. 7.22b). The ρ's produced in the most forward region can be attributed to the double diffractive dissociation process (discussed in section 1.5), where the photon as a rho vector meson scatters off the target proton leaving it in an 'excited' state followed by the rho meson decaying to two pions in the forward hemisphere and the 'excited' target decaying in the backward hemisphere. The distribution of forward rho mesons is consistent with the predictions of the triple Regge model and the photoproduction data at lower energies (Fig. 1.6). The centrally produced rho mesons can be attributed to quark fusion (also discussed in section 1.5), where a quark 'in' the photon fuses with a quark in the proton. The data in this region is consistent with the predictions and lower energy photoproduction data presented in Figure 1.7.

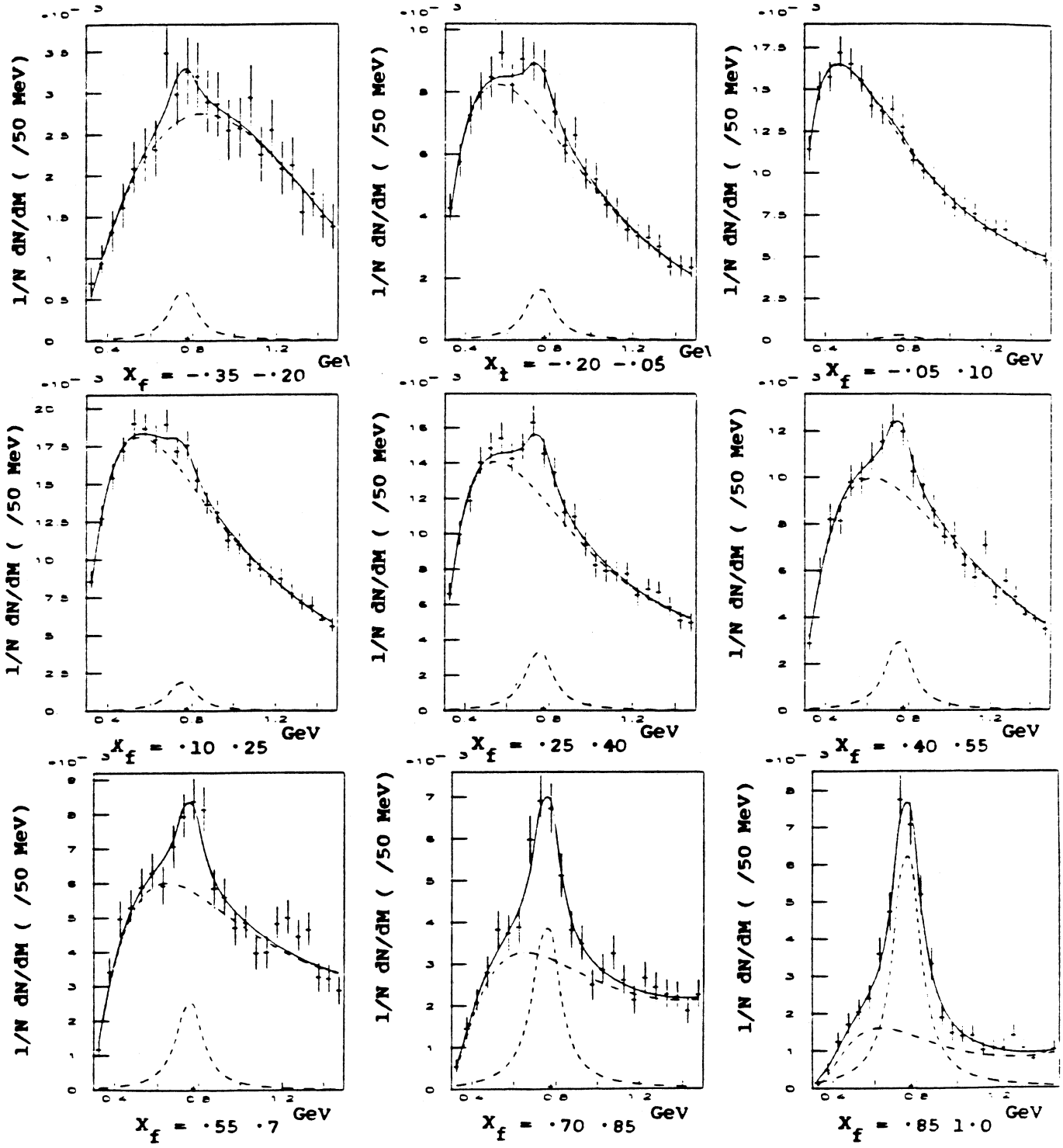

Fig. 7.21 Mass Spectrum in Slices of Xf

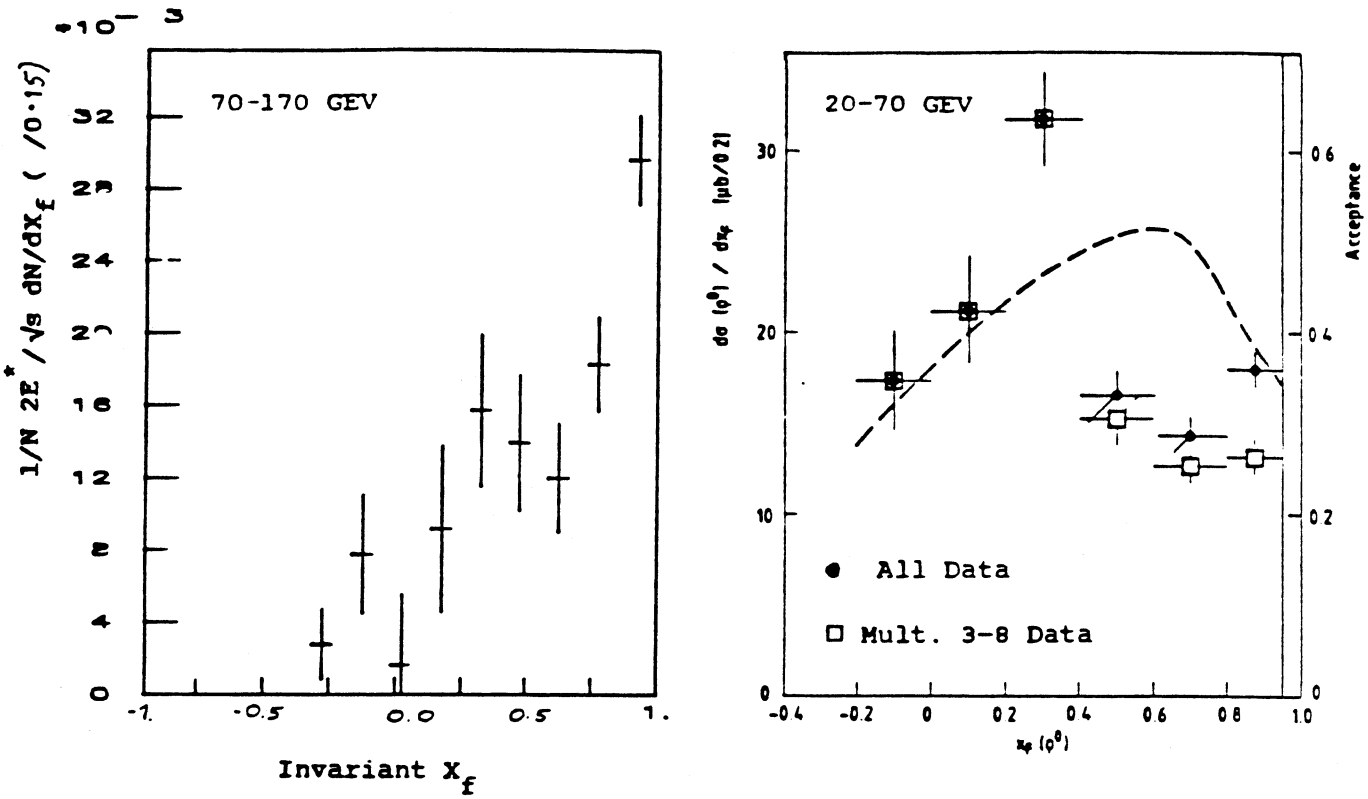

Fig. 7.22 Rho Invariant Xf Distribution from the Partial Mass Fits

In order to investigate the production characteristics of the ρ further in both the forward double diffractive dissociation region ($X_f > 0{\cdot}7$) and the central region ($0{\cdot}0 < X_f < 0{\cdot}7$) the transverse momentum P_t^2 and forward hemisphere charge-multiplicity were plotted. The selection on the ρ signal was done using the same peak-wings selection as for the inclusive X_f distributions. The P_t^2 distributions (Fig. 7.23) show that forward produced rho's have on average less P_t^2 than the centrally produced ones. The charge multiplicity in the forward hemisphere ($X_f > 0{\cdot}0$)) associated with a forward rho and a centrally produced rho (Fig. 7.24) show that forward rho events have predominantly two charged tracks in the forward direction whereas the events with centrally produced rhos have more charged tracks. There is of course, a significant amount of contamination between the forward and central regions.

forward and central regions.

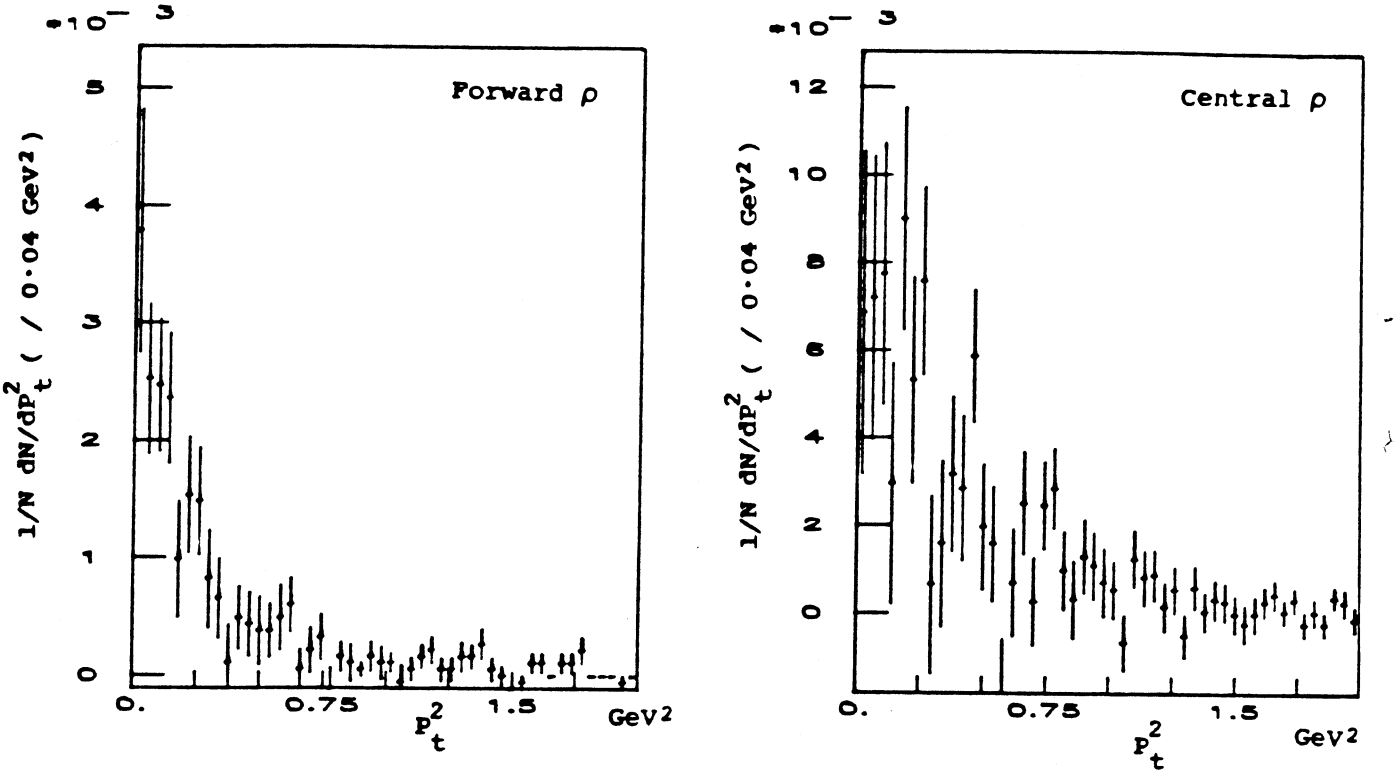

Fig. 7.23 Transverse Momentum Distributions for the Rho's

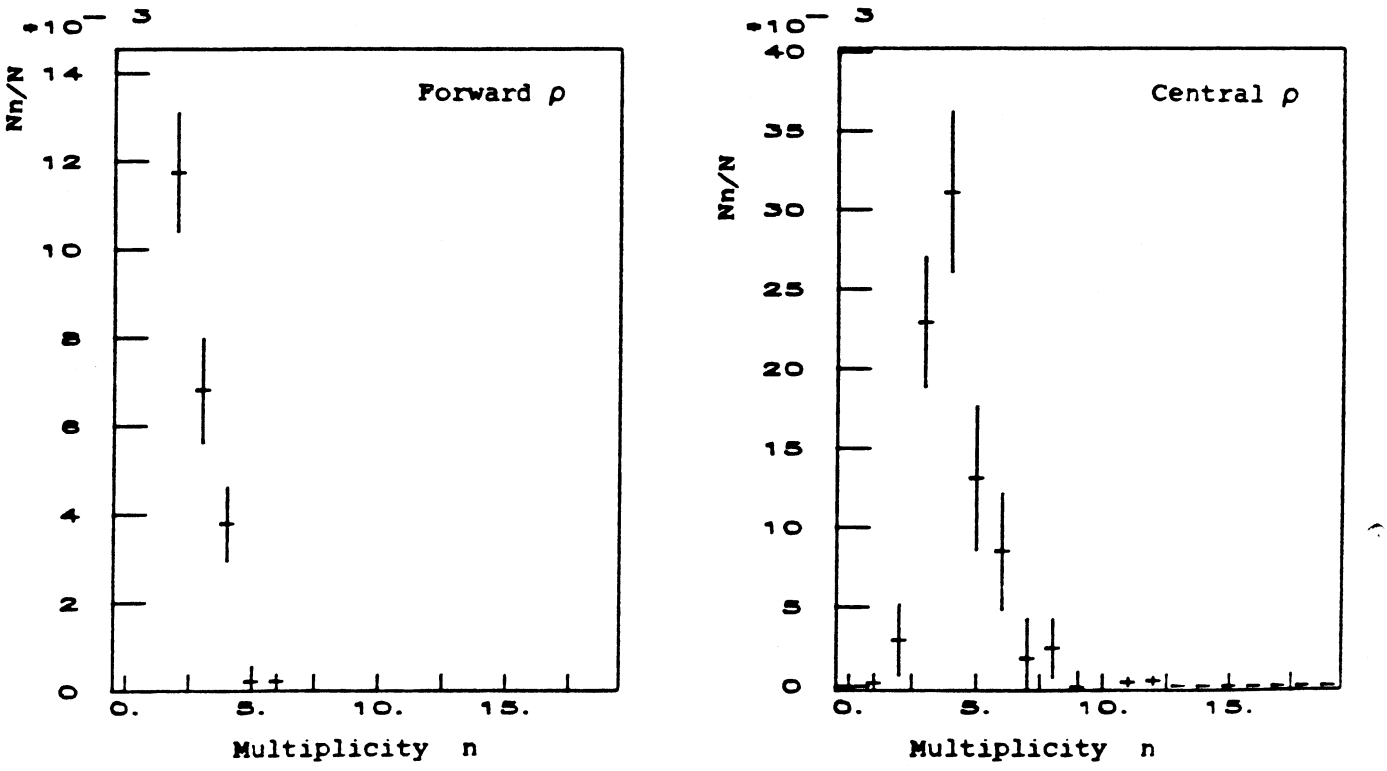

Fig. 7.24 Forward Charge-Multiplicity Distributions for Rho events

These distributions are consistent with the idea of double diffractive dissociation and quark fusion in the two regions.

The angular distribution of the π^+ from the ρ was also considered to investigate the spin alignment in each region. $\rho(770)$ was selected by peak-wings as usual and the π^+ angular distributions plotted in the helicity frame (angle between the π^+ and the ρ direction in the ρ rest frame) and the Gottfried-Jackson frame (angle between the π^+ and the beam direction in the ρ rest frame). The angular distributions in both frames (fig. 7.25) and (Fig. 7.26) for the rho's produced in the forward and central regions show that the centrally produced rho's have less alignment than the forward produced rho's. This is consistent with the fact that diffractive processes are s-channel helicity conserving (SCHC), giving rise to a $\sin^2\Theta$ distribution in the helicity frame and a distorted $\sin^2\Theta$ distribution in the Gottfried-Jackson frame. In the quark fusion model the spin of the rho is unrelated to that of the incident photon and so gives rise to flatter angular distributions in both frames. The four angular distribution presented are not acceptance corrected and because of the low statistics and problems with TRIDENT it was decided not to acceptance correct the distributions or do a full spin-parity analysis on the data.

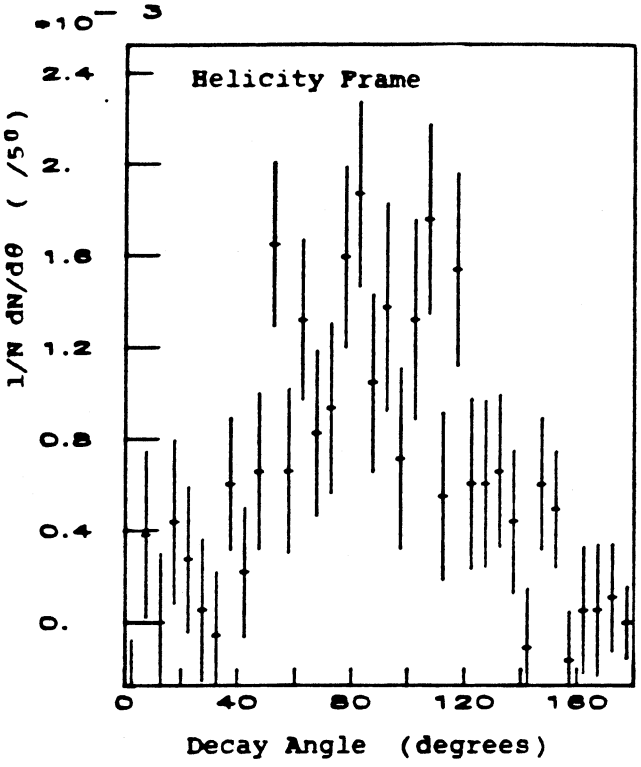

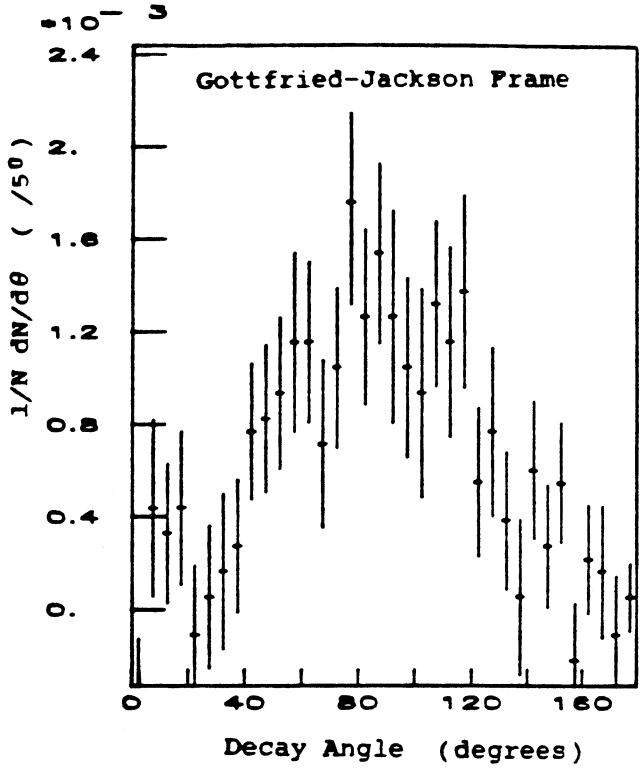

Fig. 7.25 Angular Distributions for Forward Rho mesons

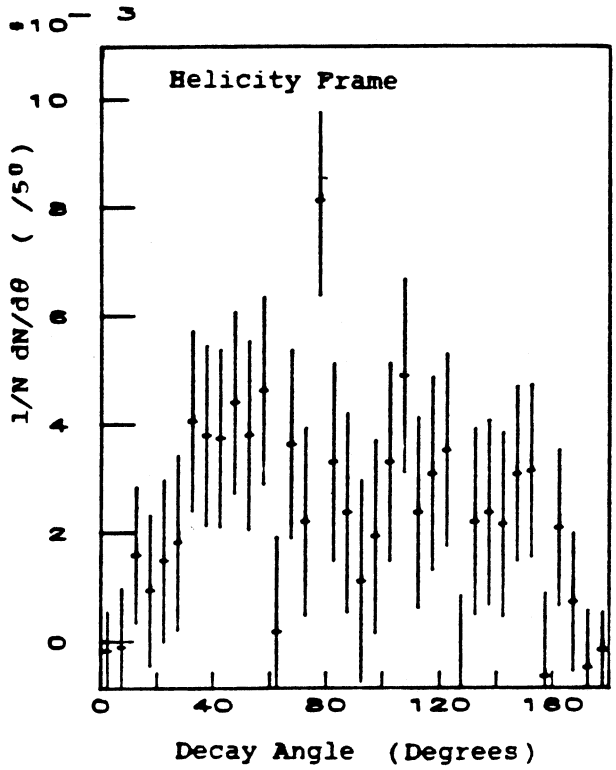

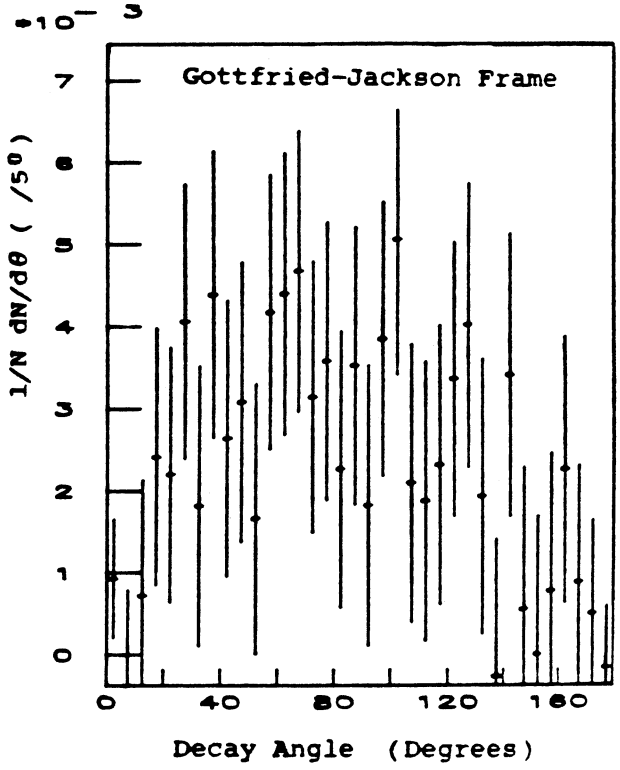

Fig. 7.26 Angular Distributions for Central Rho Mesons

7.5 - Elastic Rho(1600) Photoproduction

Data from both the fully reconstructed events and the full data sample were considered for the $\rho(1600)$ investigation. On top of the selection of either the fully reconstructed events or the full data sample the requirements of a good beam track and only 4 or 5 charged tracks were required for each event. A crude selection of elastic events was also made by requiring the longitudinal momentum difference (Pxdiff) to be less than 20 GeV. This was imposed to cut down the numbers of events for the next level of selection. Following this primary event selection and the recalculation of the track momentum vectors in the overall centre of mass frame a second set of cuts was applied to the data. All events were required to have 4 or 5 tracks with net charge balance 0 or +1 respectively. In the case of the 5 track events the slowest positive track was taken to be a proton and the event accepted if the 'proton' was in the backward hemisphere ($X_f < 0{\cdot}0$) and had transverse momentum $p_t^2 < 1{\cdot}0$ GeV^2. After the identification of candidate protons the energy balance (Ediff)

$$\text{Ediff} = E_\gamma + E_{P_t} - \sum E_\pi \; (- E_{P_r})$$

was calculated and required to be consistent with zero (|Ediff| < 4 GeV) to ensure the selection of elastic $4\pi(P)$ events only. Figure 7.27 shows the Ediff spectrum (for the completely reconstructed events only) with the selection cuts marked. Data from both the fully reconstructed events and the full event sample was considered in this analysis but it was found that the momentum accuracy of the full event sample was poor because of the inclusion

of the extra tracks. Table 7.28 shows the numbers of events at each stage of the event selection. The cross-section for the photoproduction of the elastic four charged pion channel calculated from the number of selected events and the sensitivity (calculated in the previous section) was found to be

$$\sigma(\gamma p \longrightarrow 4\pi^{\pm}(p)) = 1{\cdot}8 \pm 0{\cdot}3\ \mu b, \quad E_{\gamma} = 70 - 200\ GeV.$$

This cross-section is not acceptance corrected and may still contain a contribution from contaminant double pair production. These corrections are thought to be within the errors calculated in the cross-section. Of this data sample the summary table shows that 0·25 of the events are fully reconstructed.

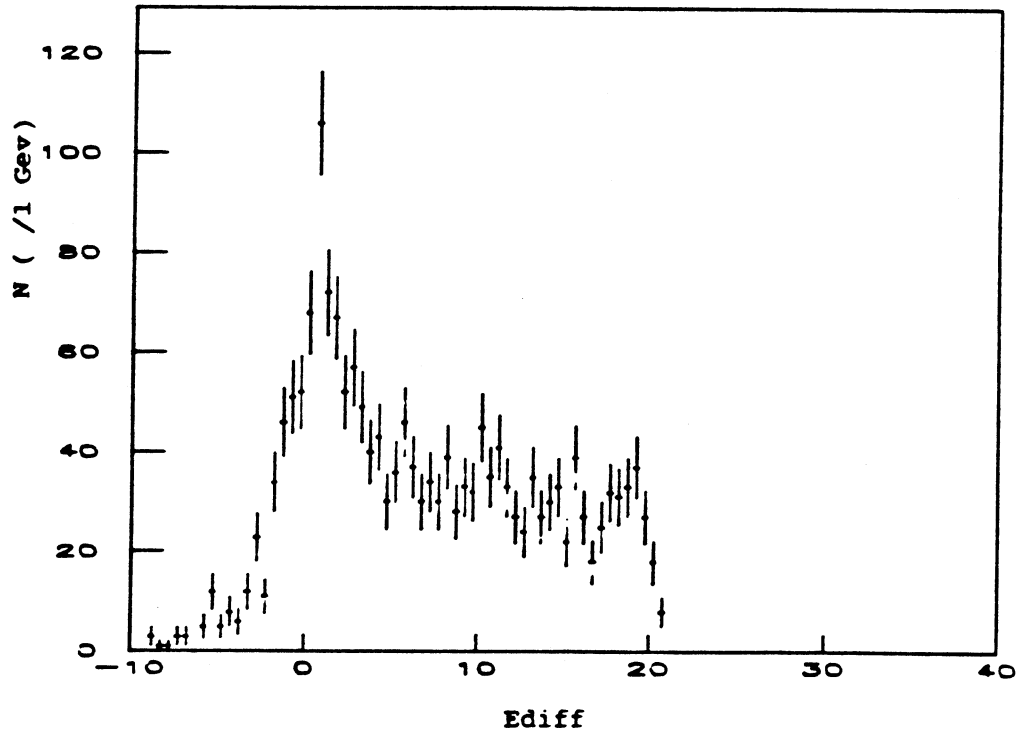

Fig. 7.27 Ediff Spectrum

	Good Events	All events
No. Photons	6.63E8 0.63E8	6.63E8 0.63E8
No. Hadronic events	231593	231593
Good Beam Vertex and Extra Tracks Cut	23911	222739
No. 4 and 5 prong	9703	64084
Pxdiff Cut	4179	28160
Pairs filter	2600	12209
Charge Balance	1888	8071
Ediff Cut	754	3006
No. 4 prong	552	2260
No. 5 prong	202	746

Fig. 7.28 Numbers of events at each level of selection

The $\pi^+\pi^-$, $\pi^\pm\pi^\pm$ and $4\pi^\pm$ invariant mass of the selected events were calculated and plotted (Fig. 7.29). In the $\pi^+\pi^-$ mass spectrum (with four entries per event) there is a clear $\rho(770)$ peak upon a combinatorial background which does not show up in the $\pi^\pm\pi^\pm$ mass spectrum (with two entries per event). In the $4\pi^\pm$ mass spectrum there is a broad enhancement between 1 and 2 GeV tailing off at high masses. The $4\pi^\pm$ mass against $\pi^+\pi^-$ mass scatter plot shows that the $4\pi^\pm$ enhancement is correlated with the $\rho(770)$ signal seen in the $\pi^+\pi^-$ mass spectrum.

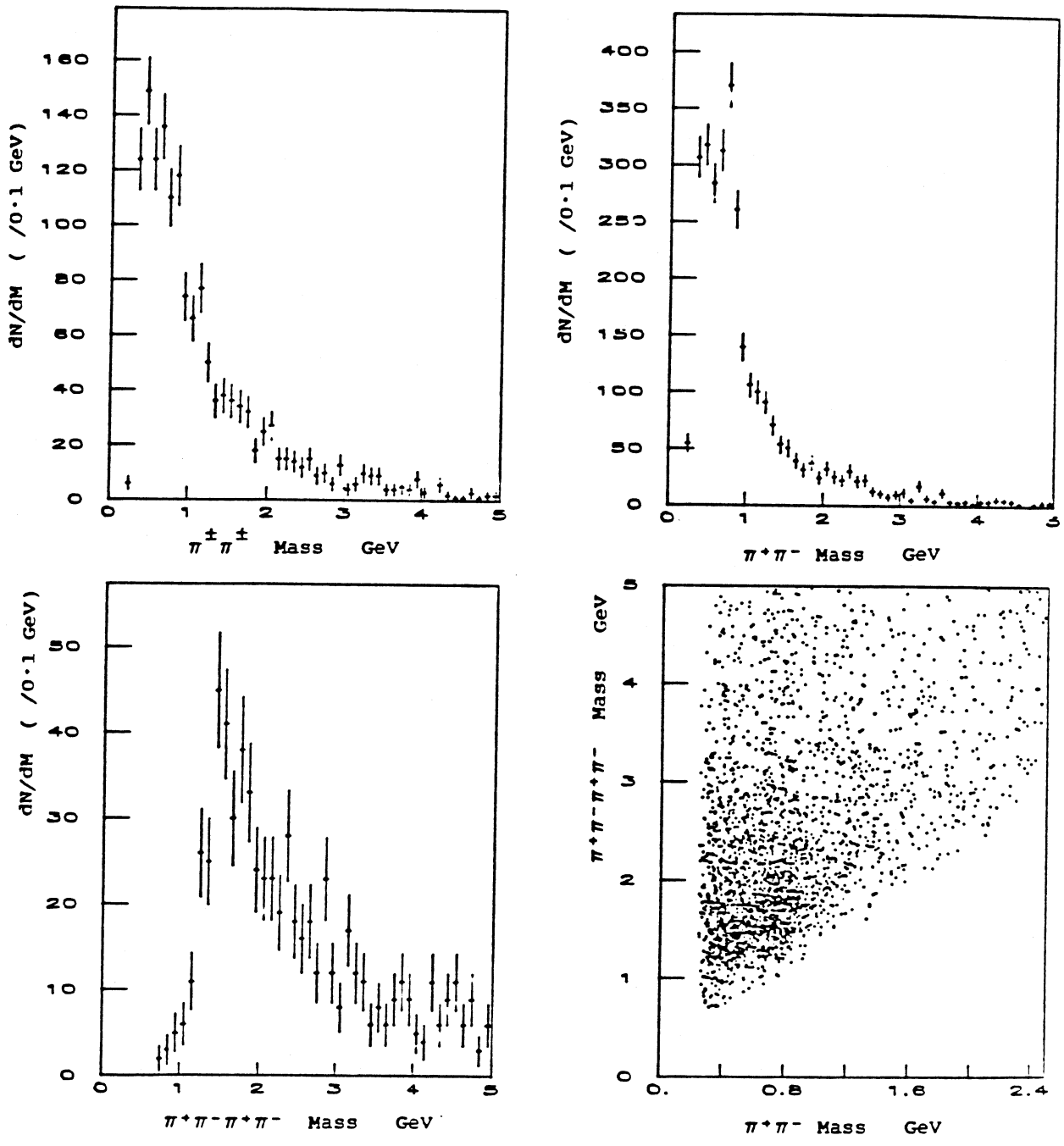

Fig. 7.29 Two and Four Pion Invariant Mass Spectra

The program SAGE (see section 6.2.6) was used to simulate diffractive photoproduction of the rhoprime(1600), with an e^{-7t} distribution with respect to the recoil proton axis (s-channel helicity conservation). The rhoprime was then allowed to decay to pions with P_t limited phase space (with $\langle P_{ti}^2 \rangle^{\frac{1}{2}} = 0{\cdot}3$ GeV). The program MAP (also see section 6.2.6) was then used to perform the trigger acceptance. Accepted events were then run through the same selection and analysis programs as if it were real data. An overall event acceptance of $0{\cdot}8 \pm 0{\cdot}1$ was calculated. This value contains both a contribution from the trigger acceptance (MAP) and a contribution from the selection used to extract the four charged pion channel. More complicated models for the decay of the rhoprime to four charged pions were considered but they gave similar values of acceptance. The error quoted contains the Monte-Carlo statistical error and a contribution for the uncertainty in the model.

In order to compare the elastic 4-pion photoproduction rate with that found in photoproduction at lower energies the cross-section of events with a four pion invariant mass less than 1·8 GeV was calculated. Using the fully reconstructed events the number of events satisfying this requirement was found to be 210. By assuming that the fraction of such events is the same in the full event sample as in the completely reconstructed event sample and an acceptance as calculated above the cross-section was found to be

$$\sigma(\gamma p \longrightarrow 4\pi^{\pm}(p)) = 0{\cdot}6 \pm 0{\cdot}2 \ \mu b \quad \text{for } M_{4\pi} < 1{\cdot}8 \text{ GeV}.$$

The main source of error in this calculation comes from the

systematic uncertainty in the assumption that the number of events in both data samples is the same, this error was taken to be 30%. The value obtained is consitent with that obtained in a photoproduction experiment at a lower photon energy range where this cross-section was found to be $0{\cdot}7 \pm 0{\cdot}2\ \mu b$ with an $E_\gamma^{-0{\cdot}4}$ dependance (Ref. 7-1).

The $4\pi^\pm$ mass spectrum was then used to estimate the number of rhoprimes in the peak at about 1600 MeV. For this estimate assumptions had to be made about the background under the signal. Taking into account a range of values of the background the number of rhoprime events was estimated to be 150 ± 75. Using the same procedure as before the cross-section was calculated and found to be

$$\sigma\left[\begin{matrix}\gamma p \longrightarrow \rho'(p) \\ \qquad\quad | \\ \qquad\quad \longrightarrow 4\pi^\pm\end{matrix}\right] = 0{\cdot}45 \pm 0{\cdot}26\ \mu b, \quad E_\gamma \ \ 70 - 170\ GeV.$$

The error reflects the small number of events and the uncertainty in the shape of the background, there is also the 30% error in the assumption that the fraction of events is the same in both event samples.

To investigate the properties of the photoproduction of the rhoprime(1600) the invariant-X_f and Mandelstam-t distributions were plotted for the ($4\pi^\pm$) (Fig. 7.30). The invariant-X_f distribution shows that the $4\pi^\pm$ state is produced in the forward direction only. The t distribution (which is the equivalent of the P_t^2 distribution for the recoil proton for small t) shows an exponential distribution with a slope not as steep as that seen at lower energies (e^{-7t}) (Ref. 7-1). This again shows that

the $4\pi^{\pm}$ state is predominantly produced in the forward direction.

In order to estimate the proportion of rho(770) in the decay of the rhoprime(1600) the two pion mass spectrum (with 4 entries per event) was plotted for events with the 4 pion mass in the range 1200 - 2000 MeV (Fig. 7.31). Using this spectrum the number of rho(770) was estimated to be 120 ± 30 for 260 events of which half is estimated to be background beneath the rhoprime signal. This suggests that the rhoprime(1600) decays predominantly to $\pi^-\pi^+\rho(770)$.

The invariant-X_f distribution and P_t^2 distributions for the pions were then plotted (Fig. 7.32). These plots show that the pions are produced in the forward hemisphere with little P_t^2 ($\langle P_t^2 \rangle \approx 0{\cdot}2$ GeV^2).

A full acceptence correction of all the distributions presented above was unjustified because of the small number of events in the data sample and the high fraction of events which were not fully reconstructed. Similarly a full spin parity analysis was felt to be unjustified.

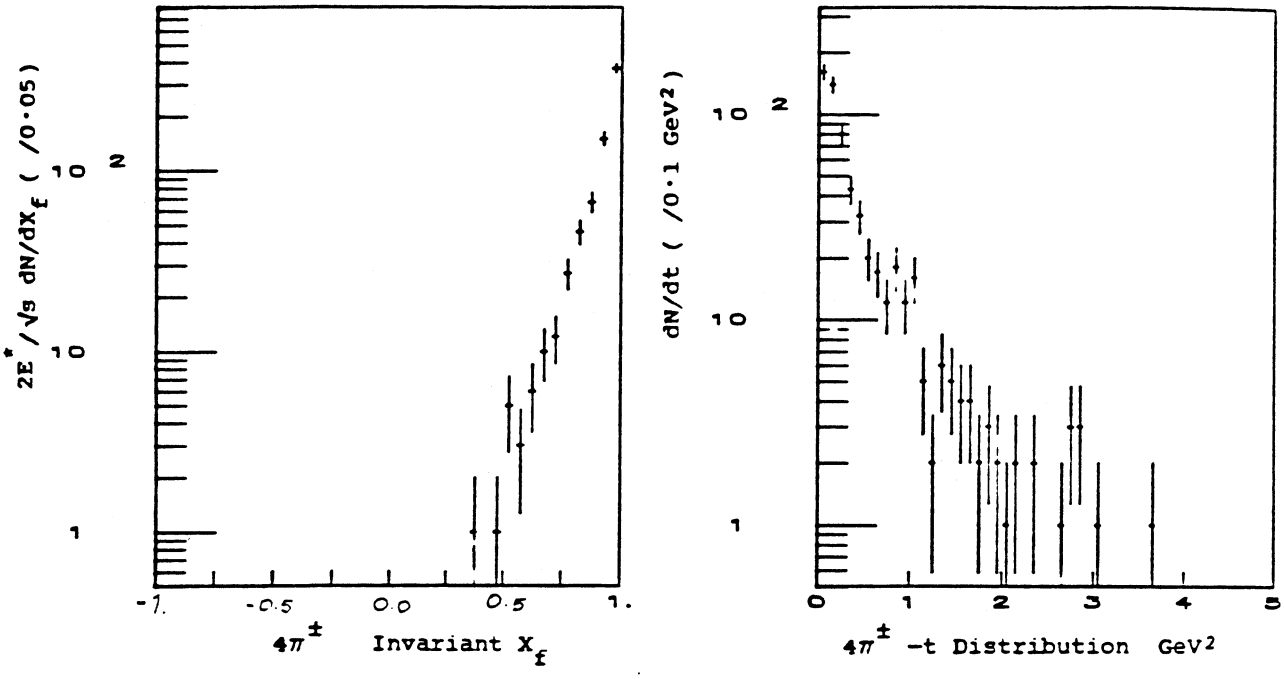

Fig. 7.30 Rhoprime Xf and t distributions

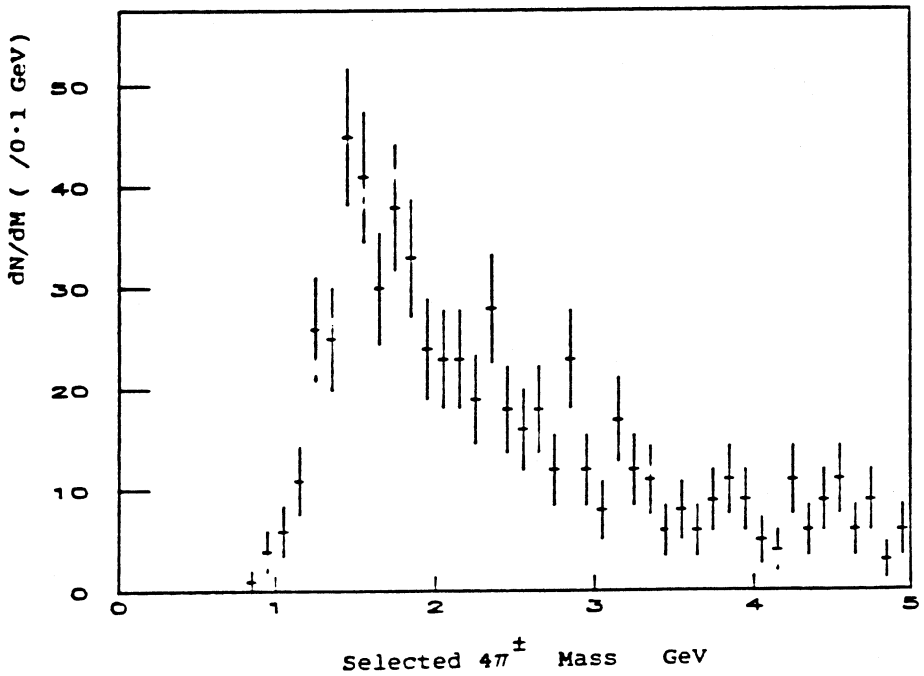

Fig. 7.31 Selected 2 Pion Mass Spectrum

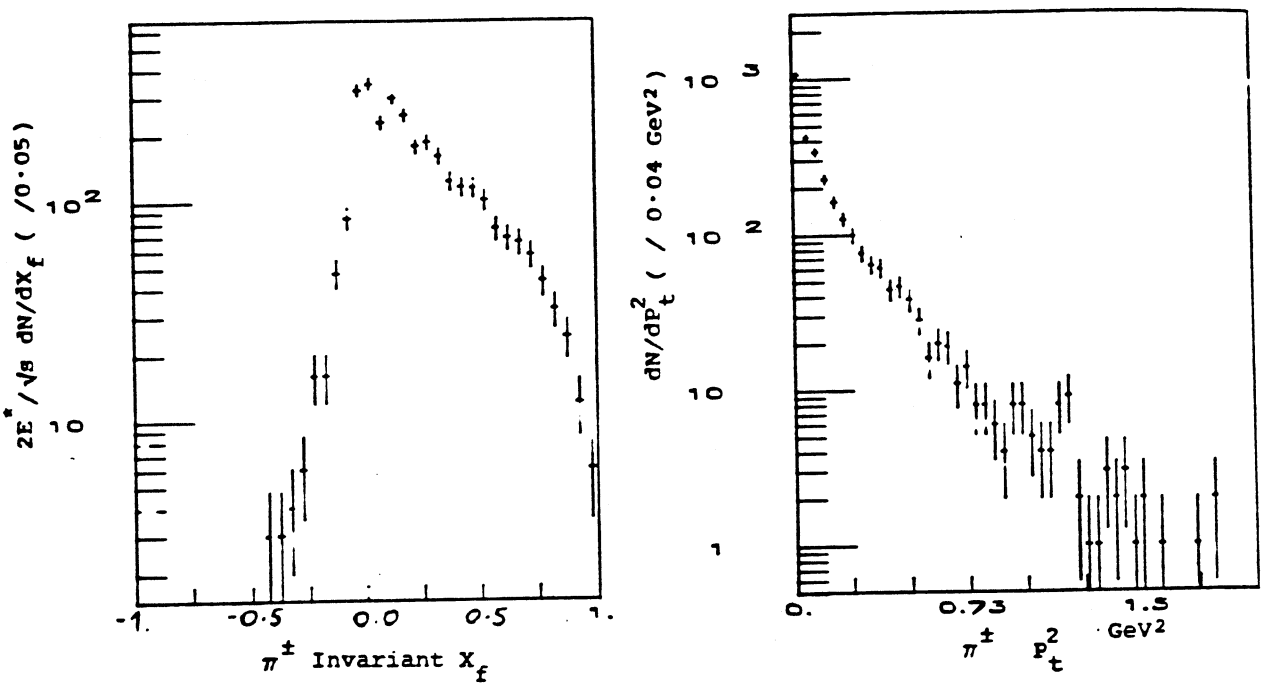

Fig. 7.32 Pion Xf and Pt Distributions from Rhoprime Decay

7.6 - Conclusions

In chapters 2 and 5 we have seen that the beam is well understood and the beam line and tagging system reconstruction program PEDRO works well. The hardware trigger electronics triggered on almost the full hadronic cross-section; unfortunately it also triggered on some electromagnetic events (mainly in the 2-prong events). The program TRIDENT was used to reconstruct charged tracks and find the event topology. The electromagnetic pairs filter in TRIDENT had the effect of removing almost all the events with less than three forward charged tracks. The TRIDENT track finding worked well but the topology and vertex finding sections were not so good, leaving on average 2·9 tracks per event not fitted to a vertex. Following a residual electromagnetic filter (to remove double pairs) the remaining 'hadronic' data sample corresponded to a cross-section of 100 ± 10 μb. This corresponds to events with charge-multiplicity greater than two and hence does not include any contributions from elastic low mass vector meson photoproduction. The total photoproduction cross-section is ≈ 120 μb, of which ≈ 12 μb can be attributed to the elastic photoproduction of the ρ, ω and ϕ. The value obtained from this data is slightly lower than the difference of the total and elastic cross-sections because of the small loss of low charge-multiplicity inelastic events in the trigger and data selection.

The mean charge-multiplicity was found to be 5·19 for the completely reconstructed events and 6·4 for the full event sample (of which 1·9 tracks on average were extra tracks). The

charge-multiplicity distributions for the completely reconstructed events was found to be in good agreement with a KNO scaling prediction for hadron-hadron interactions. The full event sample, including the extra tracks, was found to deviate from the predicted curve. This deviation suggests that many of the extra tracks found were not associated with the main event. In the backward rapidity hemisphere the loss of tracks due to absorption in the liquid hydrogen target was estimated to be about 50%. Considering the completely reconstructed event sample and making a correction for the loss of tracks a corrected mean charge-multiplicity of $\approx 7 \pm 0{\cdot}6$ was calculated in the photon energy range 70-170 GeV. In the forward rapidity hemisphere a mean charge-multiplicity of $\approx 3{\cdot}5$ was found for both event samples. The multiplicity distributions for the completely reconstructed events were found to be in agreement with the KNO scaling predictions but not in agreement for the full event sample. This suggests that the inclusion of the events with extra tracks biased the forward charge-multiplicity distribution without affecting the mean. Deviations from KNO scaling were investigated in the forward rapidity hemisphere where beam energy dependent components of the hydrogen target acceptance loss had no effect. The dispersion moment D_2, which in pure KNO scaling is predicted to be proportional to the mean multiplicity has been shown to have a small but significant offset. There may also be deviations from KNO scaling in the higher c_k multiplicity distribution moments. Such deviations have also been seen in PP scattering at the CERN ISR.

The inclusive rho(770) photoproduction cross-section was found to be 27 ± 6 μb. This is in agreement with the value measured in

photoproduction at lower energies. The invariant-X_f distribution for the rho was calculated by fitting a Breit-Wigner resonance together with a background to 2-pion mass spectra in slices of X_f, then using the fit in each slice to determine the proportion of rho. The invariant-X_f distribution showed production of rho in two regions. The first region, in the forward direction is due to the double diffractive dissociation process. In the forward region the rho's have small P_t^2 and show evidence for spin alignment (expected with SCHC). In second region, the central region, rho production is due to quark fusion. In this region the rho's have more P_t^2 and do not show any evidence of alignment to either the helicity axis or Gottfried-Jackson axis.

In the four charged pion channel an enhancement at a mass a little above threshold has been observed. This enhancement could be due to elastic photoproduction of the rhoprime(1600). By estimating the area under this enhancement the cross-section for photoproduction of this state was calculated as $0{\cdot}45 \pm 0{\cdot}26$ μb. This is consistent with the cross-section for the same channel at lower energies. The production of this enhancement suggests a diffractive mechanism where sharp forward peaking is observed in the four pion state. In the decay of this enhancement there is evidence that the decay goes via an intermediate state ($\rho^0\pi^+\pi^-$) which then decays to ($\pi^+\pi^-\pi^+\pi^-$). These observations have also been made in the decay of a similar enhancement in photoproduction at lower energies where it was identified as the rhoprime(1600).

7.7 - References

7-1 The Rection $\gamma p \longrightarrow p\pi^+\pi^-\pi^+\pi^-$ for Photons Energies from 25 to 70 GeV
D. Aston et al Nucl. Phys. B189(1981)15

7-2 Hadronic Cross-Section Study in e^+e^- Collisions form 1·350 to 2.125 GeV
G. Cosme et al Nucl. Phys. B152 (1979) 215

7-3 Photoproduction of Multiparticle States in the Beam Fragmentation Region for Photon Energies in the range 50-70 GeV
M. Atkinson et al CERN-EP/84-124
(Submitted to Zeitschrift fur Physik C)

7-4 Private Commumication Prof. A. Donnachie

7-5 Proton Fragmentation into Pions and Pion Systems in K^-P Interactions at 110 GeV and Comparison to Model Predictions
R. Göttegens et al CERN Pre-print CERN/EP 83-161 Oct 1983

7-6 Experimental Results on Strong Interactions in the NAL Hydrogen Bubble Chamber
J. Whitmore Phys. Rep. 10C 275-373 May 1974

7-7 Charged Multiplicity Distributions In PP Interactions at ISR Energies
A. Breakstone et al CERN Pre-print CERN/EP 83-165 Oct 1983

7-8 Evidence for the Systematic Behavior of Charged-Prong Multiplicity Distributions in High-Energy Proton-Proton Collisions
P. Slattery Phys. Rev. D 7 2073-2079 (1973)

7-9 HBOOK Histogramming, fitting and data presentation package
CERN DD-US-72 CERN DD-EE-81.1 Version 3 May 1983

7-10 Inclusive Photoproduction of ρ and ω in the Photon Energy Range 20 to 70 GeV
M. Atkinson et al CERN-EP/84-30

7.8 - Figure Captions

7.1 Rapidity (Good Events)

7.2 Rapidity (all events)

7.3 Charge-Multiplicity Distributions

7.4 Invariant-Xf and Pt2 Distributions (Good Events)

7.5 Invariant-Xf and Pt2 Distributions (all events)

7.6 Pt2 Distribution in Photoproduction at 50-70 GeV

7.7 Number of Events against Beam Energy

7.8 Mean Charge Multiplicity

7.9 KNO Scaling Distributions for Photoproduction

7.10 Invariant Cross-Sections in the Backward Hemisphere

7.11 Backward Charge-Multiplicity

7.12 Forward Single Particle Xf and Pt2 Distributions

7.13 Mean Forward Charge Multiplicity

7.14 KNO Scaling Function in the Forward Hemisphere

7.15 Photon Fragmentation Charge Multiplicity Moments

7.16 Photon Fragmentation Charge Multiplicity Dispersion

7.17 Two Particle Correlation Function f2

7.18 f2 for Photoproduction, PP and Hadron Scattering

7.19 2 Pion Invariant Mass Spectrum

7.20 Rho Invariant Xf and Pt2 Distributions

7.21 Mass Spectrum in Slices of Xf

7.22 Rho Invariant Xf Distribution from the Partial Mass Fits

7.23 Transverse Momentum Distributions for the Rho's

7.24 Forward Charge-Multiplicity Distributions for Rho events

7.25 Angular Distributions for Forward Rho mesons

7.26 Angular Distributions for Central Rho Mesons

7.27 Ediff Spectrum

7.28 Numbers of events at each level of selection

7.29 Two and Four Pion Invariant Mass Spectra

7.30 Rhoprime Xf and t distributions

7.31 Selected 2 Pion Mass Spectrum

7.32 Pion Xf and Pt Distributions from Rhoprime Decay

Acknowledgements

I wish to thank all the members of the Eγ collaboration (involving people from the Universities of Lancaster, Manchester and Sheffield, the Rutherford Appleton Laboratory in England and the University of Bonn in West Germany) for their work in designing, building, setting up and running the WA69 experiment at CERN. Special thanks go to my supervisor, Dr M. Ibbotson for his friendly guidance and encouragement during my three years research at Manchester. Many thanks also go to Mr R J Thompson, Mr D. Mercer and Dr R. E. Hugh-Jones for their help and guidance with aspects of the hardware development I have been involved with. Many thanks also go to Dr G. D. Lafferty for help with the analysis and to Prof. A. Donnachie for help with aspects of theoretical physics encountered during my research.

Thanks go to CERN and particularly all those involved with the Omega facility for providing the facilities for running the experiment. Thanks also go to computer centres at CERN, the Rutherford Appleton Laboratory and Manchester University Physics Departments for providing facilities for data analysis.

I am grateful for financial assistance from the SERC during my three years of research and for funding the WA69 experiment.

Finally, I would like to thank my fiancée Miss G. M. Clowes for her eternal patience and support.